Università degli Studi di Parma

Ph.D Thesis in

Science and Technology of Innovatives Materials

Study of Molecular Sensitization Processes of Nanostructured Metal Oxides

Francesca Detto

Supervisor:

Dr. Giancarlo Salviati

Tutor:

Dr. Salvatore Iannotta

Coordinator:

Prof. Enrico Dalcanale

Dottorato di ricerca XXIV ciclo

Marzo 2012

Contents

Chapter 1

Introduction

Functional hybrids are nano-composite materials lying at the interface of organic and inorganic realms, combining properties and advantages of both materials, and possibly minimizing their disadvantages. During the last years several studies on hybrid materials aimed at improving the performances and the reliability of these compounds for applications in energetics, gas sensing and optoelectronics. On these motivations, metal oxides have drawn renewed attention due to their ability to exchange charges with condensed molecules. In fact, when a molecule condenses onto a solid's surface, the molecule's frontier orbitals assume different energies respect to their gas-phase values. This phenomenon can either enable or inhibit charge transfer with the solid, depending on the suitability of the energy alignment of donor and acceptor states in both materials. Considering the large variety of both metal oxides and organic molecules, their potential high versatility offers a wide range of ways of realizing tailored materials in term of chemical and physical properties.

Nanostructured titanium dioxide is one of the most investigated material for hybrid systems, as its application areas range from photovoltaics and photocatalysis to photo-/electrochromics, optoelectronics and sensors. New interesting physical and chemical properties arise when the particles size decreases down to the nanometer scale. In particular, the high surface-to-volume ratio established by small particle size is beneficial to hybrid devices, as it facilitates the sensitization processes between the inorganic material and its molecular counterpart and the reactions between the device and the interacting media.

Among organic molecules, metal-phthalocyanines (MPcs) are of particular interest due their great versatility and high thermal and chemical stability. In particular the MPcs are the ideal candidates for hybrid photovoltaic applications, as their high absorbtion in the visible and ultra-violet spectral range and their p-type semiconducting character make them suitable as absorber-dye and hole-carrier transport layer. Moreover, the strong dependence of their conduction properties upon doping with gases makes them very appealing for application in gas sensing.

A critical and very challenging issue in hybrid system engineering is the contemporary achievement of the metal oxide nano-crystals and the molecular sensitization process. As the high crystalline quality of TiO_2 is commonly obtained through thermal treatments, its organic decoration is usually carried out in successive separate steps. Supersonic beams techniques (SuMBD) offer to overcome this challenge, thanks to the possibility of working with both organic molecules and inorganic aggregates, and to the ability to achieve physical and chemical processes at surfaces. In fact, beams seeded by organic molecules can be used to achieve growth of thin film, while deposition of inorganic species can be realized by using Pulsed Microplasma Clusters Sources (PMCS). The main characteristic of this approach is the control of the particles' kinetics by tuning the energy of the molecular precursors. In this way the kinetic energy can be tuned from 0.1 eV up to tens of eV, up to the activation of chemical/physical processes at the interface of a growing film, e.g. bond formation and improved structural order.

The aim of this thesis work is the study of the molecular sensitization processes, induced by supersonic beams approaches, that occurs at the titanium dioxide/copper phthalocyanine interface. This chapter introduces a general overview about the deposition methods, the materials (both inorganic and organic), the diagnostic techniques used during this PhD thesis. All the experimental results will be presented and discussed in next chapters. In particular, chapter 2 reports the first extensive analysis about nanostructured TiO_2 thin films grown by PMCS, whose peculiarities result from the non conventionality of the deposition technique. In order to collect a comprehensive knowledge about this nanostructured material, the candidate used a wide range of diagnostic techniques at the nanoscale. At the Parma IMEM-CNR Laboratories, the as-grown TiO_2 thin films were investigated by

means of several electron microscopy techniques. The morphological and luminescence properties have been evaluated by Scanning Electron Microscopy and Cathodoluminescence, while Transmission Electron Microscopy analyses provided the structural information. These studies have been integrated by surface photoelectron spectroscopies (XPS and UPS), that the candidate performed at the Trento IMEM-CNR Laboratories in order to study the material electronic properties. Moreover, the effects of annealing treatments on the observed properties have been investigated and discussed.

Chapter 3 reports the results of photoelectron emission experiments on both copper and free-base phthalocyanine, grown by means of supersonic beams seeded by organic precursors. These experiments have been carried out at synchrotron ELETTRA (Trieste). The aim of this study was to understand the real influence of the metal core on the molecule electronic properties. Taking advantages of the high resolution of the synchrotron facility, it was possible to determine well suitable fit models for both molecules. In particular, the deconvolution model related to the CuPc was decisive in the last part of this thesis work, to analyze the reactivity processes at the inorganic/organic interface.

After achieving a comprehensive knowledge of the electronic properties of both the organic and the inorganic counterparts, we focused our attention to the chemical reactivity phenomena occurring at their interface, which is the final aim of this thesis work (chapter 4). In the Trento IMEM-CNR Laboratories, we got two hybrid systems with the same configuration (CuPc/TiO_2) in a combined PMCS/SuMBD approach. In both cases the nanocrystalline metal oxide has been synthesized by PMCS, at room temperature without the need of any thermal treatment. In order to understand the role of the kinetic energy during the sensitization process, the CuPc deposition has been performed by molecular seeded beams at high (experiment A) and low (experiment B) kinetic energies. For both hybrid systems, a complete characterization of core levels and valence band states have been performed at increasing organic coverages, in order to better emphasize the dynamic of the chemical bonds formation at the interface, induced by different kinetic energies.

1.1 Supersonic Beams and thin film growth

In this section, a general picture about supersonic molecular beams is outlined. After a short introduction about the historical background that led to the development of this technique, fundamental physics of a free jet expansion is presented and related to the classical thermodynamics of an effusive cell. Two kinds of supersonic beams sources are then depicted, the continuous ones used for organic molecules and the pulsed ones used for cluster metal oxide thin films growth, comparing operating principles and experimental apparata. In the first case, we talk about Supersonic Molecular Deposition (SuMBD), while in the second case the technique is properly referred PMCS (Pulsed Microplasma Cluster Source). Furthermore, basic gas-surface interactions and dynamics are introduced and correlated to the peculiar features of supersonic beams techniques.
For a further exhaustive and comprehensive discussion about supersonic molecular beams, the reader is referred to the books by G. Scoles [1] and by P. Milani and S. Iannotta [2].

1.1.1 Historical background

In 1910 the invention of High Speed Vacuum Pumps suddenly paved the way to a new branch of science: the molecular beams physics. After the first pioneering work by Dunoyer [3] just one year later, free jets and supersonic molecular beams methods have been used for over a half century in many historical experiments investigating basic principles of modern physics. Some emblematic examples are the measurement of electric and magnetic moments of atoms and molecules by beam deflection in applied fields and the analysis of intermolecular forces in scattering experiments, both carried out by Stern and Gerlach [4] [5]. Further innovations in the apparatus design, introduced in 1951 by Kantrowitz and Grey [6] and improved in 1954 by Becker and Bier [7], solved the so-called problem of the "scattering cloud", producing a supersonic beam with higher intensities and narrower velocity spread than those related to conventional effusive sources. In the following years, the theoretical framework of supersonic beams experienced a great development, thanks to the study of the internal degrees of freedom relaxation of molecules [8] and of the processes occurring during collisions in the supersonic regime

[9]. As a matter of a fact, in a short of time supersonic beams have become the ideal environment to study free molecules, preferred to others for their narrow velocity distribution and for the strong cooling effects that allow the investigation of both spectroscopy of large cold molecules and the dynamics of cluster formations [10].

1.1.2 Supersonic beams properties and thermodynamics

For a better comprehension of the physics of supersonic beams, we will describe first the thermodynamic parameters and laws of a classical effusive source. Supersonic free jet expansion and beam formation are then introduced and discussed.

Classic effusive sorces: Knudsen cells

A Knudsen cell can be essentially described like a oven in a vacuum chamber, from which the sublimed material can leak in the vacuum through a small orifice, called nozzle (Figure 1.1). Inside this oven, the sublimating material

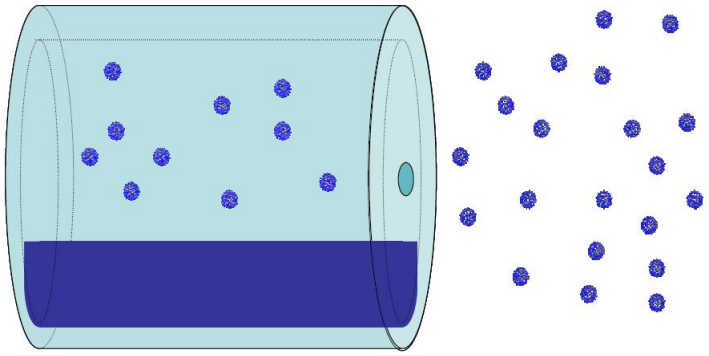

Figure 1.1: Schematic picture of an effusive Knudsen cell

is kept at temperature T_0 ($\sim 10^2 - 10^3 K$) by a feedback control system, and it is in thermal equilibrium with its vapours, at a pressure P_0 ($\sim 10^{-3} - 10^{-1} torr$). Since the nozzle aperture is smaller than the mean free path λ of the particles (usually some cm), the outgoing flux is molecular and it can be fully described by the classical gas kinetic theory. As the atoms or the molecules in effusive regime beam don't experience any collision, their internal degrees of freedom (the roto-vibrational energies) are the typical one

of a gas in thermal equilibrium at the specific temperature, so their velocity distribution $f(v)$ is given by a Maxwellian distribution:

$$f(v)dv = \frac{4}{\sqrt{\pi}} v^2 e^{-v^2} dv, \tag{1.1}$$

and the most probable velocity is described as:

$$\overline{v}[cm \cdot s^{-1}] = 1.4551 \cdot 10^4 \sqrt{\frac{T_0}{M}} \tag{1.2}$$

(being M the mass in atomic units). The intensity of a Knudsen effusive beam is defined by the number of molecules dN, leaving the orifice area element $d\sigma$, during time dt, with a velocity between v and dv , into a solid element $d\omega$, whose axis is at an angle θ respect to the normal at $d\sigma$, and it is given by the following relation:

$$\frac{dN}{dt}(\theta, v) = I(\theta, v)d\omega = \frac{d\omega}{4\pi} n_0 f(v) v \cos\theta d\omega dv d\sigma. \tag{1.3}$$

where n_0 is the the number density in the source, in $atoms/cm^3$. By integrating this equation over all velocities, we obtain the characteristic cosine angular distribution typical of effusive beams:

$$I(\theta)d\omega = \frac{d\omega}{4\pi} n_0 \overline{v} \cos\theta d\sigma \tag{1.4}$$

Supersonic free jets expansion

As mentioned in the last paragraph, the necessary condition for an expansion in effusive regime is

$$\frac{\lambda}{d} = K > 1, \tag{1.5}$$

where K is called *Knudsen number*. As the mean free path λ of the atoms is related to the source pressure and temperature by the relation:

$$\lambda = \frac{7.321 \cdot 10^{-20} T_0}{P_0 \sigma}, \tag{1.6}$$

it is possible to obtain a supersonic beam in which $K \ll 1$, by increasing the pressure P_0 (usually five orders of magnitude higher than a Knudsen cell). The high pressure gradient between the source and the external vacuum chamber will give rise to a free jet expansion, characterized by a large number of atoms collisions. Evidently, the supersonic regime can be obtained only if the experimental apparatus is supplied by an adequate pumping speed, able

to preserve the pressure gradient even in the presence of high gas load.
A supersonic beam source is constituted by an heated cylinder, inside of which high pressure gas is injected, that is put in communication with the external vacuum chamber through a nozzle. Figure 1.2 represents in detail the case of a free jet supersonic expansion from a converging nozzle, assuming an isentropic expansion with negligible heat conduction and viscous effects. The physic condition within the source (called *stagnation state*) is

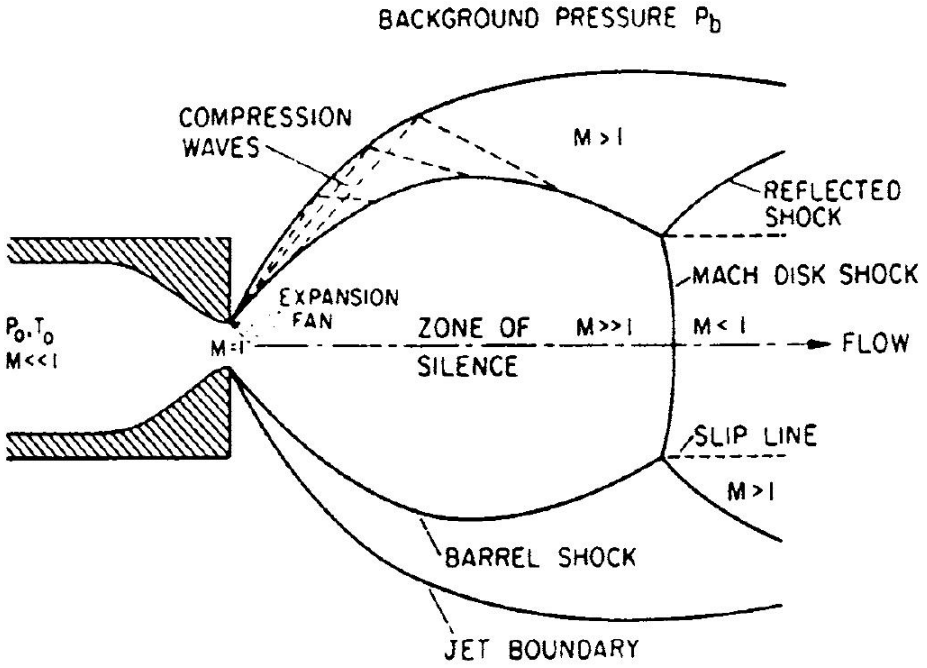

Figure 1.2: Different regions in a continuum free-jet expansion, formed by the interactions between the expanding and the background gases. M indicated the mach number. Taken from [1]

fully described by P_0 and T_0. This is a thermalized condition where the gas particles have a statistical thermal velocity distribution that depends on P_0 and T_0, with a quasi-static drift towards the nozzle. As the particles flow through the aperture, they accelerate under the effect of the pressure gradient, reaching immediately the sonic speed. This zone, just called *sonic region*, is placed at the nozzle exit and it is labeled in Figure 1.2 with M=1. M is the *Mach number* and is defined as the ratio between the velocity of gas particles and the local velocity of sound propagation. Just outside the

nozzle, the gas particles experience the highest acceleration and succeed to reach supersonic velocities: this region (marked in Figure 1.2 with the label M»1) is the core of the expansion and it is called *zone of silence*, because the gas in this region does not "feel" the presence of the external environment. In the forward direction, the border of the supersonic beam (called *Mach disk*) is outlined by shock waves outside of which the supersonic properties are strongly depleted and lost. On the other hand, on the side region the flow loses its isentropic and not-viscous behavior, decreasing its velocities by means of compression waves (M>1). The Mach disk distance from the nozzle δ_M can be evaluated using the empirical rule:

$$\delta_M = 0.67\sqrt{\frac{P_0}{P_{out}}}, \tag{1.7}$$

where P_{out} is the external pressure in the vacuum chamber. By placing a conical collimator, called *skimmer*, at a distance lower than δ_M from the noozle, it is possible to extract the particles with specific and desired characteristics from the zone of silence, in order to generate a well defined supersonic molecular beam. The skimmer design has to conciliate the requirement of an efficient particles selection with the need of low interference with the processes occurring in the zone of silence: the best found compromise is a sharp edged skimmer with an hyperbolic profile. Moreover, thanks to its small aperture, the skimmer is also useful to guarantee a vacuum pumping independence between the chamber where the beam is generated and the chamber where the beam itself will be used.

Supersonic expansion dynamics of a gas mixture

The assumption of isentropic and not-viscous expansion, made in the previous section, is a good approximation for high-speed flux, because the flow time is definitely shorter than the characteristic diffusion times of heat-conduction and viscous effects. The enthalpy conservation for such a flow can be written as:

$$H_0 = H + \frac{v^2}{2}. \tag{1.8}$$

This means that the enthalpy per mass unit H_0 is constant along each streamline coming from the source: as the gas expands and cools, its enthalpy

decreases giving rise to the increase of its mean velocity

$$v = 2(H_0 - H) = 2\int_T^{T_0} C_p dt. \tag{1.9}$$

By assuming that C_p is constant over the range from T_0 to T, and considering that for ideal gases $dH = C_p dt$ the beam velocity becomes:

$$v = \sqrt{2C_p\,(T_0 - T)}. \tag{1.10}$$

If $T \ll T_0$, the maximum final velocity will be:

$$v_\infty = \sqrt{2C_p T_0} = \sqrt{\frac{2K}{m}\left(\frac{\gamma}{\gamma - 1}\right)T_0} \tag{1.11}$$

where γ is the ratio between the specific heats at constant pressure and volume and can be related to C_p by

$$C_p = \frac{K}{m}\left(\frac{\gamma}{\gamma - 1}\right). \tag{1.12}$$

If the beam is a mixture of gases and different masses are present, the heat capacity has to be expressed as a weighted average:

$$C_p = \Sigma_i X_i C_{p_i} = \Sigma_i X_i \frac{K}{m_i}\left(\frac{\gamma}{\gamma - 1}\right) \tag{1.13}$$

being X_i the fraction of the species, in the gas mixture, with mass m_i. Therefore each species will be characterized by a different energy depending on its mass:

$$E_i = \left(\frac{m_i}{\overline{m}}\right)T_0 \tag{1.14}$$

where $\overline{m}$ is the weighted average mass of the beam particles. As a consequence of equation 1.14, it is possible to obtain heavy molecules with kinetic energies much higher then their thermal equilibrium by diluting them in lighter species (aerodynamical acceleration). The difference between the velocity of *carrier gas* (the lighter one) and the *seeded molecules* (the heavier one) is called *velocity slip*. If the seeded species are highly diluted (around $0.1 \div 0.01\%$ of the molecular beam), their final parameters can be described as a function of the Mach number M and γ. Thus, taking into account that $v = \sqrt{\frac{\gamma KT}{m}}$

$$\frac{T}{T_0} = \left(1 + \frac{\gamma - 1}{2}M^2\right)^{\frac{1}{2}} \tag{1.15}$$

$$v = \sqrt{\gamma \frac{KT_0}{m}} M \left(1 + \frac{\gamma - 1}{2} M^2\right)^{\frac{1}{2}}. \tag{1.16}$$

Considering an ideal isentropic expansion with constant γ

$$\frac{P}{P_0} = \left(\frac{T}{T_0}\right)^{\gamma/\gamma-1} = \left(1 + \frac{\gamma - 1}{2} M^2\right)^{-\gamma/\gamma-1} \tag{1.17}$$

$$\frac{\rho}{\rho_0} = \frac{n}{n_0} = \left(\frac{T}{T_0}\right)^{1/\gamma-1} = \left(1 + \frac{\gamma - 1}{2} M^2\right)^{-1/\gamma-1} \tag{1.18}$$

Once the value of M along the beam axis is known, the equations 1.15, 1.16, 1.17 and 1.18 describe completely the complex dynamics of the expansion. Obviously, the easiest case is that of the sonic region, where M is constant across any nozzle cross-section, so the expansion can be determined using the approximation of a quasi-one dimensional compressive flow. With these assumption, the mass flow rate $\dot{m}$ can be calculated, taking into account the nozzle shape. In fact, for converging nozzles, sonic and subsonic regions could be characterized by viscous phenomena, but in the regime of fast flow rates and short nozzles (see next paragraph) these effects can be neglected and we can write the mass flow rate:

$$\dot{m} = \rho v A = P_0 A^* \left[\frac{m}{KT_0} \gamma \left(\frac{2}{\gamma + 1}\right)^{\frac{\gamma+1}{\gamma-1}}\right]^{1/2} \tag{1.19}$$

where A is the cross section of the nozzle and can be calculated from the minimum cross section A^* (at the throat), by using the following relationship:

$$\frac{A}{A^*} = \frac{1}{M} \left[\frac{2}{\gamma + 1} \left(1 + \frac{\gamma - 1}{2} M^2\right)\right]^{\frac{\gamma+1}{2(\gamma-1)}} \tag{1.20}$$

Outside the nozzle these approximations are no longer valid, and a computational method is needed to calculate the mach number as a function of the position. In particular, according to *Methods of Characteristic (MOC)* [9], one of the most used for this purpose, the value of M can be written as:

$$M = A = \left[\frac{x - x_0}{d}\right]^{\gamma-1} - \frac{\frac{\gamma+1}{2(\gamma-1)}}{A\left[\frac{x-x_0}{d}\right]^{\gamma-1}} \tag{1.21}$$

assuming that the beam, far from the expansion, propagates along straight lines in a spherical expansion, from a point source centred at $\frac{x_0}{d}$ [11].
In figure 1.3 is reported the typical behavior of the main parameters of the beam as a function of the distance from the noozle, in the case of a

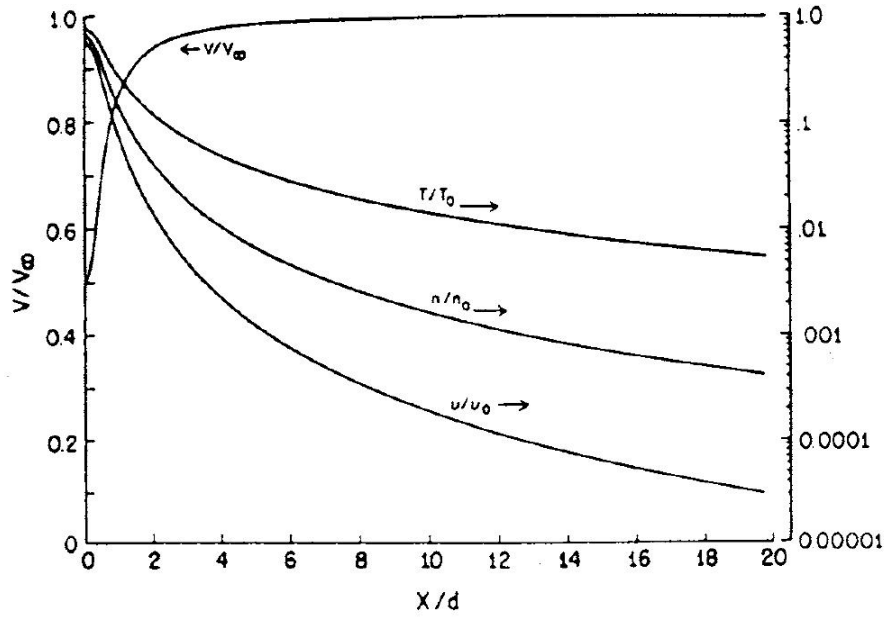

Figure 1.3: Evolution of velocity V, temperature T, density n and ν (collision rate for binary hard spheres) normalized to the corresponding values in the stagnation conditions (T_0 and n_0) and to the limit velocity (V_∞), plotted against the parameter x/d. From [1]

gas with $\gamma = \frac{5}{3}$, considering all the previous assumptions (isentropic flow, ideal gas behavior, C_P constant, continuum flow). It should be noticed that while very short distances are needed to reach the asymptotic velocity, the other parameters (temperature, density and collision rate) require 20 and more nozzle diameters to reduce themselves to their limiting value. In particular, when the collision frequency become too low, it cannot maintain the continuum flow regime and the beam is subjected to a transition to free molecular flow. Furthermore, if the molecule flow rate N is described as

$$N = n_0 F(\gamma) \left(\frac{\pi d^2}{4}\right) \sqrt{\frac{2KT_0}{m}} \tag{1.22}$$

and

$$F(\gamma) = \left(\frac{\gamma}{\gamma+1}\right)^{\frac{1}{2}} \left(\frac{2}{\gamma+1}\right)^{\frac{1}{\gamma-1}} \tag{1.23}$$

The intensity of a supersonic beam in ideal conditions (with no background scattering and skimmer interference effect) can be evaluated in terms of

molecules per radiant and second:

$$I_0 = \kappa N/\pi \tag{1.24}$$

The parameter κ is called *peaking factor* and it ranges from 1 to 2 depending on γ (for example $\kappa = 1$ for an ideal effusive source). From equation 1.24 it results clear that the forward intensity of a supersonic beam is higher then an effusive source as both N and κ have greater values in supersonic beams. In particular the density of a supersonic beam falls off going out of its centreline approximately as cos^4. An other important feature of the supersonic beams is the so-called "freezing" of the internal degrees of freedom of the molecules: as the rotational and vibrational modes of polyatomic molecules requires from 10 to 100 collisions to relax, the great number of collision (typically $10^2 - 10^3$) that occurs during the free-jet expansion [1] succeeds to cool efficiently all the molecular internal modes and to turn them in kinetic energy. This cooling phenomenon may cause the alignment of the backbone of strongly anisotropic molecules along the propagation axes of the beam [12] [13], that can affect the degree of ordering of the film growth. Before the expansion runs out of collision, it is possible to evaluate the velocity spread around the mean velocity by solving the Boltzmann equation: we obtain a distribution function distinguished in two directions (perpendicular and parallel to the beam propagation direction). Since $T_{//}$ is different from $T_{\perp}$, the gaussian distributions has different widths in the two direction (Ellipsoidal Drifting Maxwellinan Model). From the parallel component of the spread velocity it is possible to determine the energy resolution of the beam. With this purpose, we introduce a new variable S, called *speed ratio* and defined as the ratio between the mean velocity $\bar{v}$ and the velocity thermal spread:

$$S = \frac{\bar{v}}{\sqrt{\frac{2KT}{m}}} = M\sqrt{\frac{\gamma}{2}} \tag{1.25}$$

In order to obtain a narrow velocity distribution, very high ratio speed are needed: this can be reached by increasing the stagnation pressure and acting in this way on the efficiency of seeding, and increasing the cooling processes through collision. The most important limitations in the monochromatization of the beam are, obviously, the pumping speed that can not supply too high gas load, and the clustering phenomena that generates heat (it will be discussed in the next section). The expansion of a gas mixture

shows also an important mass-separation effect: assuming that at the exit of the nozzle all particles have approximately the same mean velocity and temperature the speed ratio of heavier species results higher than the one associated to lighter molecules. Since the beam divergence is clearly related to the transverse speed ratio, the angular spread of diluted particles is much smaller than that of the carrier gas.

Clustering phenomena

The clusters nucleation typically occurs when the heat of condensation is immediately taken away from the forming aggregates: for this reason, the use of cold carrier gas and the activation of cooling phenomena make a supersonic expansion the ideal environment to produce and control the cluster formation [14]. The density of the formed clusters as well as their average size are firstly depending by pressures and temperatures of both seeded and carrier gas. In particular, low source temperatures promote the supersaturation onset (so the higher T the smaller is clusters size and number), while high carrier gas pressure enhances clusters formation, by increasing the number of collisions. Moreover, the final mass distribution is also affected by the type of carrier gas and the seeding level, as the large clusters are stabilized by the collisions between carrier gas particles and those of the seeding species. The nozzle geometry and size is a further critical parameter to control the beam properties like clustering phenomena. Large nozzle diameters typically enhance cluster formation, while the expansion coming from smaller nozzles runs out collisions rapidly, producing smaller and fewer clusters. Moreover, a constrained expansion induces higher number of collisions, increasing the formation of clusters, so the nozzle geometry can be conveniently designed and selected to promote or inhibit particles aggregation. Following the notation of Hagena and Obert [15], three different configurations can be defined to produce an axial symmetric free jet: the sonic, the conical and the Laval nozzle (Figure 1.4). Among them, the first geometry is specifically designed to minimize the collisions number as well as the expansion time, in order to reduce clustering, while conical, cylindrical and converging/diverging nozzles are specifically suitable for particles aggregation.

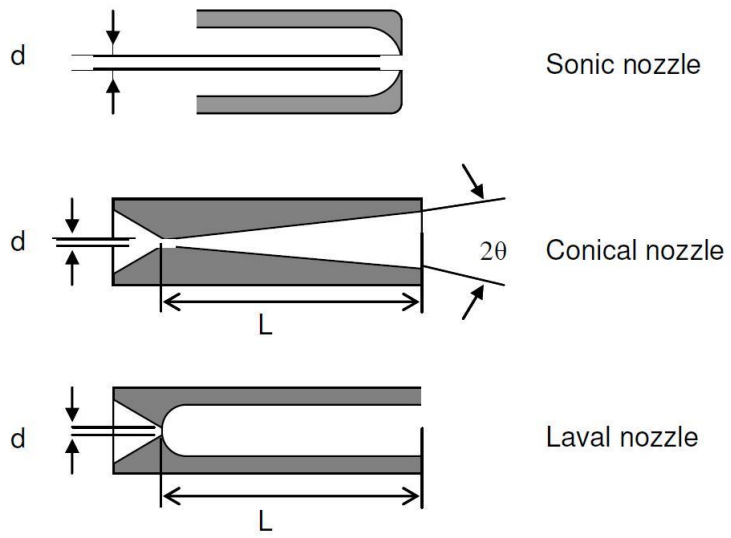

Figure 1.4: Some examples of nozzle geometries, axially symmetric.

Supersonic vs effusive deposition: a summary

In order to offer to the reader a clearer view on the innovative peculiarities of the supersonic beam growth techniques, we report in this paragraph a summary of the main features that distinguish them from classic Knudsen cells. It has to be reminded that the two sources operate in completely different framework conditions: while classical effusive cells are thermal equilibrium systems, supersonic beam sources are controlled by non-equilibrium processes.

- T_f and P_f in supersonic beam sources are considerably smaller than those of the stagnation values. On the contrary in Knudsen cells there is no significative difference between initial and final temperatures and pressions.

- In a supersonic beam the Knudsen number K_N is $\ll 1$: this means that the gas is underexpanded and a large number of collisions occurs. After a distance of a few nozzles diameters, the flow becomes completely free molecular (and K_N becomes > 1 like in classical effusive source).

- In supersonic regime the kinetic energies involved are noticeably larger than the initial values due to isentropic expansion and the large number

of collisions. On the contrary the velocity distribution from Knudsen cells reflects that of the oven.

- Free jet expansion induces a fast cooling of the internal degrees of freedom of the seeded species, whose efficiency depends from the energy spacing of molecular states. Such effects are not present in Knudsen cells, where the state population is given by the standard distribution at the temperature of the source. The degree of seeding of the species in lighter and non condensable carrier gases can be used to control the kinetic energy and the roto-vibrational cooling.

- the velocity distribution of a supersonic source has a very narrow spread (proportional to $\frac{(2\gamma)^{1/2}}{M}$), while a Knudsen cell is characterized by a larger Maxwellian velocity distribution. This difference can be valued in the left picture of Figure 1.5 where a Mach 50 beam is compared to a Knudsen cell.

- Clustering phenomena can promoted in supersonic beams, by changing the nozzle shape and controlling the degree of seeding of the species in the carrier gas. In Knudsen cells, clustering can be achieved only by external cooling and gas aggregation [2].

- As shown in the right picture of Figure 1.5, the forward intensity of a supersonic molecular source is narrowly peaked along the beam axis, while in effusive cells it follows a cosine-like angular intensity distribution.

1.1.3 The supersonic growth method

A major step towards the success of supersonic beam methods for thin films growth dates to about 10-15 years ago [2], when new development in supersonic beam sources were achieved, demonstrating the ability of controlling properties at different lengthscale of nanostructures and molecular systems. An important landmark has been the discovery of C_{60} [16], given by Smalley (awarded by Nobel Price in 1996) using a novel pulsed laser ablation supersonic source. The Trento IMEM-CNR group has been then developing specific methods for deposition of π-conjugated molecules by free jet expansions. This is a leading laboratory in supersonic beams methods [17]

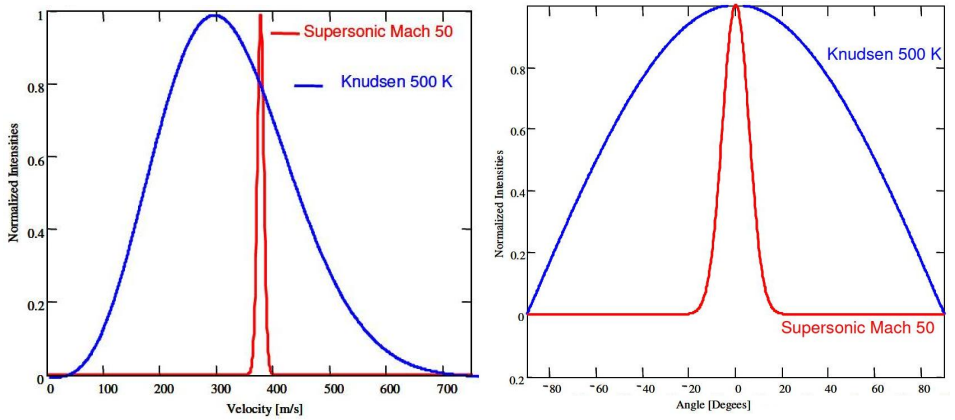

Figure 1.5: Velocity spread (left) and angular distribution (right) produced by supersonic and effusive sources.

and applications, spreading its research interests from molecular spectroscopies [18], to cluster physics [2] [19], [20] gas phase chemistry [21], growth processes [19] [13] prototype electronic and optoelectronic device developments [22] [23] [24]. Recently, the Trento IMEM-CNR group is exploiting the great versatility of Supersonic Beams techniques in the deposition of both organic molecules and refractory materials: in fact, just making the appropriate modifications to the seeding system, it is possible to obtain a continuous expansion of organic molecules (SuMBD) or a pulsed beam of inorganic clusters (PMCS). This peculiarity allows the deposition of the whole hybrid device, that can be projected with the desired and more suitable architecture: we can deposit first the inorganic material and subsequently the organic molecules (or viceversa), or we could carry out a simultaneous co-deposition by converging the two different kinds of beam, leading to a more efficient sensitization [25]. In this section we will analyze in details the different features and operation principles of the two kind of supersonic sources: the continuous one, suitable for organic molecules, and the pulsed one, used for the deposition of refractory materials. Straight afterwards, a more general view on the whole experimental deposition apparatus will be given. All the facilities that we are about to describe (and that have been used for the preparation of all the sample analysed in this thesis work) have been projected and developed by the IMEM-CNR in Trento.

Supersonic continuous sources

The typical design and the schematic principle of operation of a supersonic continuous source, suitable for materials sublimating at low temperatures, are shown in Figure 1.6. The carrier gas (usually a noble gas) is supplied

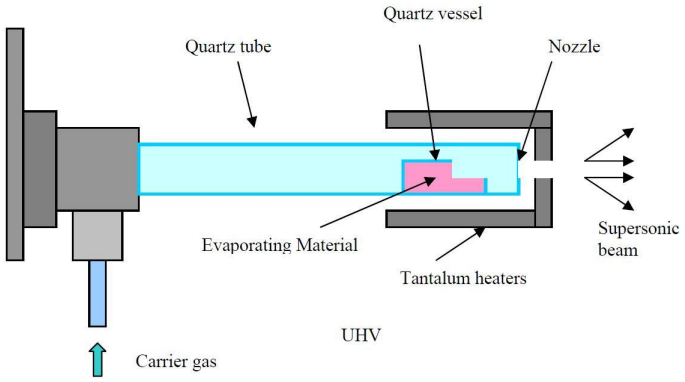

Figure 1.6: Configuration of a supersonic continuous source.

at a pressure $P_{gas} \simeq 100 - 2000$ mbar into a quartz cylinder, where a vessel filled with the organic material is placed. At the end of the quartz cylinder there is a noozle, 250-500 μm long and with a typical diameter of about 100 μm. The sublimation of the organic molecules, is allowed by a cylindrical tantalium heater (called *body heater*) enclosing the quartz tube, and by a filament placed just around the nozzle region (usually referred as *head heater*). The temperature of body and head can be independently controlled, by means of two different thermocouple that give the proper feedback to two power supplies. As already mentioned, the temperatures of the heaters are very important because they determine the temperature T_0 of the stagnation state, affecting the characteristics of the beam. This source is designed to operate for a wide range of material with sublimating temperatures lower than 1000-1100 °C. The organic material vapour seeds the carrier gas at typical concentration of $10^3 - 10^4$, then cross the noozle aperture and experience a supersonic expansion.

Supersonic pulsed sources

This kind of source is used when the supersonic beams have to be seeded by aggregates of materials that can hardly be sublimed. The vaporization of

these refractory materials is achieved through the ablation by high voltage discharge. The sputtered material and the carrier gas then thermalize in the source chamber; subsequently the seeded gas formed in such way expand in vacuum through the nozzle producing a supersonic beam. The Pulsed Microplasma Cluster Source (PMCS)is schematically represented in figure 1.7. It consists of a ceramic cube of 40 mm side length, where a 1.8 cm^3

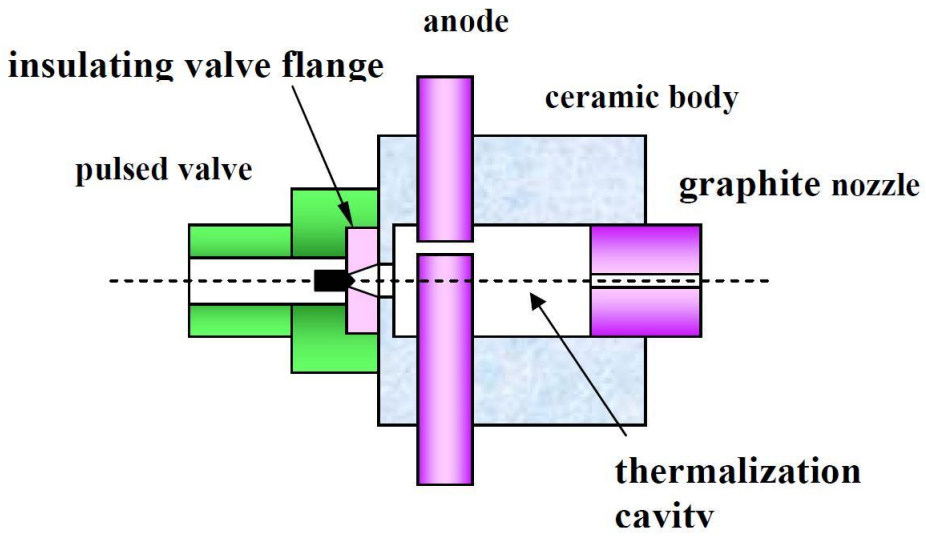

Figure 1.7: Configuration of a supersonic pulsed source.

cylindrical cavity has been drilled. Then a small channel (6 mm of diameter) is drilled perpendicular to the axis of the cavity and hosts two rods (the electrodes) of the material to be vaporized, facing each other and separated by a gap of about 1 mm. A removable nozzle with cylindrical shape, 2 mm in diameter and 8 mm long, closes the front of the source. The carrier gas inlet is supplied by a pulsed electro-valve, that in a pulse of few hundreds of μs is able to generate a gas jet with a pressure of several tens of bars. This valve is controlled by an external power supply that, by proper feedback from the vacuum gauge, stabilizes the reproducibility of each pulse. In this way, the carrier gas (usually helium or a mixture of helium and oxygen) is injected at 20 bar through an insulating ceramic nozzle on the back of the cavity and expands in the source chamber and along the rods surfaces (note that the gap between the two bars is out off axis-Figure 1.7). After the injection of the carrier gas pulse, a short (few tens of ms) and very

intense (hundreds of amperes) discharge is fired between the electrodes by applying a voltage ranging from 500 up to 1500 V. Ionized helium sputters small area of the cathode surface, causing the vaporization of the rods atoms and cluster nucleation. the peculiar source cavity configuration allows the efficiency enhancement of the ablation process, that is localized in a very small region of the target. The clusters are then carried out through the nozzle by the supersonic expansion, where further clustering phenomena can take place.

Experimental Apparatus

During last years a quite relevant number of original supersonic beams apparata has been designed and developed by IMEM-CNR Laboratory in Trento. These apparata have also been equipped by several kind of instrumentation in order to perform chemical-physical studies both in the gas and solid state. The supersonic beam apparatus used in this work (Figure 1.8) is essentially composed of two stages, supplied by a vacuum system, able to maintain pressures of about 10^{-4} mbar in the first chamber and 10^{-7} mbar in the second, even at high gas load (about 1200-1500 mbar for continuous source). The first stage has a cylindrical structure with horizontal main axis and hosts the source that is mounted on the front circular flange; by replacing this flange it is possible to switch from a continuous to a pulsed beam. This chamber is pumped by a MAG2800 turbo-molecular pump and by a special primary pump (IPX500, $\sim 500 m^3/h$) The second chamber has a truncated cone-shaped structure and is pumped by a MAGW830 turbo-molecular pump, whose pre-vacuum is supplied by the aforementioned IPX. This stage acts as an interface between the source chamber and the final deposition chamber and hosts a quartz microbalance in order to monitor the intensity of the beam that is typically 30 $\dot{A}/min$ for the continuous source and 10 $\dot{A}/min$ for the pulsed one. This apparatus can be directly connected to an analysis chamber, equipped by surface spectroscopies, to perform in-situ characterizations (Figure 1.9): in this way it is possible to study the surface properties at different stages of the deposition and to avoid contamination phenomena. The beam geometry and axis is defined by two collimators. One of them is placed between the first and the second stage on the axis of the vacuum system, and the other one between the second and the deposition chamber.

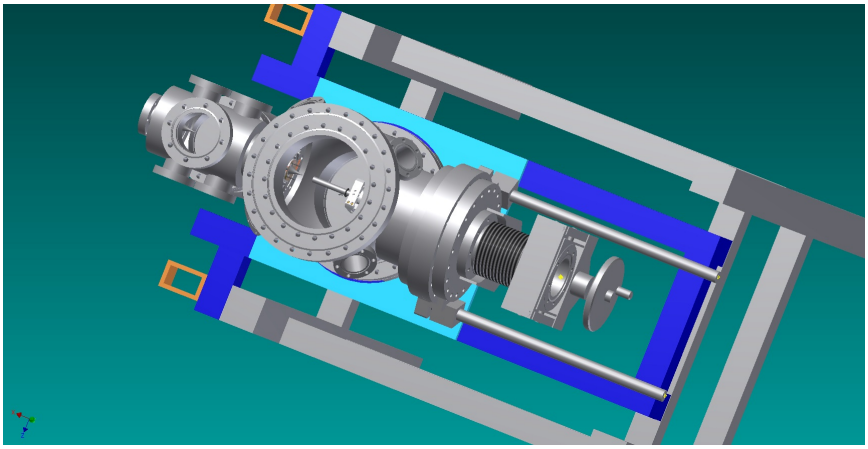

Figure 1.8: High-angle shot of a Supersonic Beam chamber.

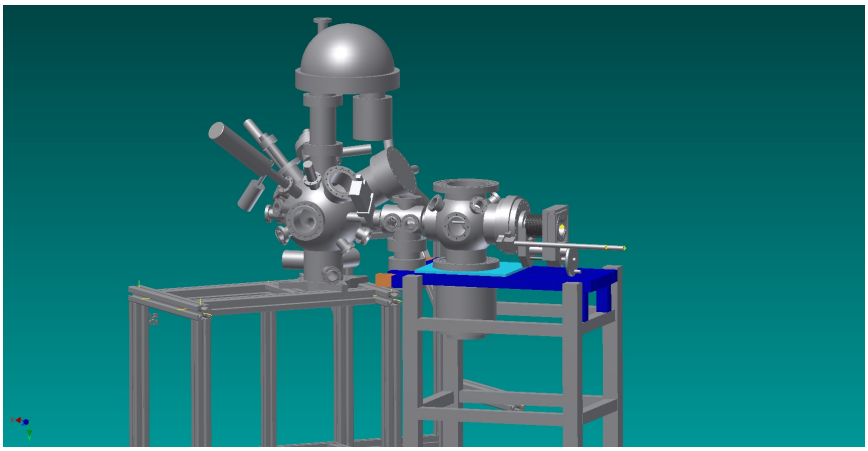

Figure 1.9: Experimental configuration for in-situ characterizations: the Supersonic Beam Chamber is directly connected to the analysis chamber

The real skimmer is the first one, since it is properly used to extract the supersonic molecular beam out of the zone of silence of the supersonic expansion and also works as a diaphragm between the two vacuum chambers. It is mounted on a heatable holder, in order to avoid the condensation of the seeded molecules and its following blocking up. The skimmers used for the pulsed source have a conical geometry, while an hyperbolic profile is preferred for the continuous sources. The second collimator, having a parabolic profile, is mostly used to keep a differential vacuum between the second and the deposition chamber and defines the size of the beam spot downstream.

The axis defined by the two skimmers remain fixed and define the basics geometry of the apparatus. The beam source have to be aligned on this axis every time that the source itself is changed, by means of a X,Y,Z transition stage. In order to insure best safety and operating conditions, the apparatus is equipped by several pressure gauges, sensors and electronic feedbacks. In particular the pressure is monitored simultaneously in the source, and in the two different vacuum stages including low and high vacuum sections.

1.1.4 Gas-surface interactions and dynamics

The gas-surface interactions give rise a large number of processes, including adsorption, desorption, chemisorption, energy transfer, clustering and coalescence, whose dynamics have been the subject of a very wide and extensive studies [26] [27]. Nevertheless the interaction between a gas particle and a solid surface can be described recalling two main processes: the physisorption and the chemisorption. The interplay between the surface energy potentials of the dissociated (A+B) and associated (AB) gas particle/surface system will determine which kind of adsorption will occur. Figure 1.10 describes the surface energy potentials as a function of the particle/surface distance z, involved in various interaction processes. In the case (a) the particle ap-

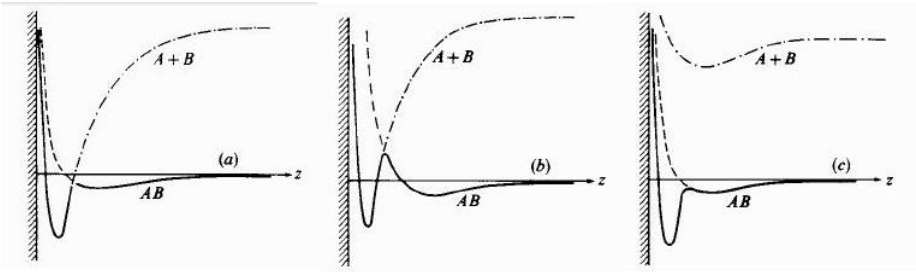

Figure 1.10: Schematic diagram of the potential energy for three kinds of adsorption processes in a gas particle/substrate system: (a) dissociative chemisorption; (b) physisorption and (c) molecular chemisorption.

proaching the surface experiences first the weak attractive Van der Waals forces (with the typical laterally averaged z^{-3} dependence), but the well depth is not enough to generate a stable bound state, so a dissociated system will be established (*dissociative chemisorption*). Let us consider now the

case (b) where at lower z values than the first shallow minimum of the weak dispersive forces, the repulsive forces become dominant giving rise to a potential barrier: the gas particle don't manage to reach the deeper minimum connected to a real chemisorption, so a physisorption occurs. The associative chemisorption process is the more difficult to explain by means of such a simplified model: in fact, chemical bonds need short range, strong interactions and require often an activation energy to overcome the potential barrier (c). While the strong attractive forces characterizing the chemisorption bond generate a stable and sometimes irreversible process (due to a deep potential well), the shallow potential wells (few hundreds of meV) of physisorption often produce a reversible state, that is often considered only a precursor of surface chemical reactions. The system stability of the chemisorption is

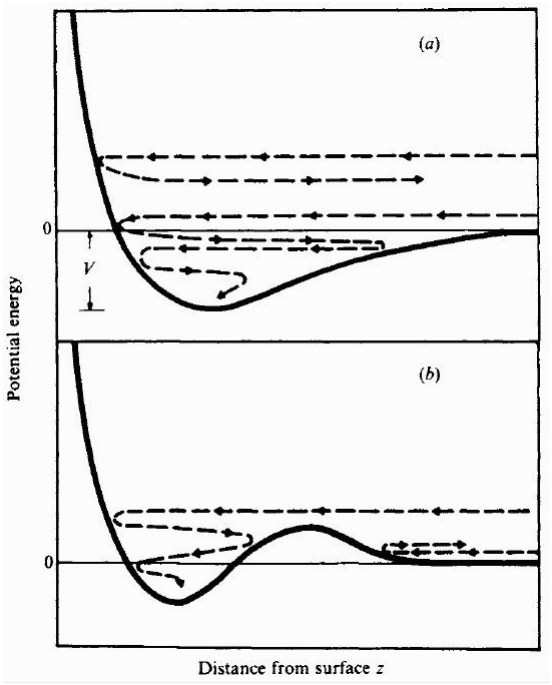

Figure 1.11: Schematic diagram of the processes occurring when a gas particles approach a surface with a given kinetic energy in the case of a simple adsorption well (a) and a potential well with an energy barrier (b)

particularly ensured if the dissociated A+B potential lies well above that of the adsorbate/substrate system, while if the crossing of the A+B and AB system occurs below the zero of energy there is a spontaneous dissociation

after a preliminary physisorption (Figure 1.10).
Let us consider the effects of the energy of the gas particle on the adsorption processes. In Figure 1.11 are represented the paths of high and low energy gas particles approaching the substrate (dashed lines), in the case of a simple absorption well or a potential well with energy barrier. In the former case (a), a gas particle experiences a backscattering if its energy is much higher than the laterally averaged well depth (upper dashed path), otherwise it can undergo to energy-loss phenomena (transitions between electronic levels, vibrational or rotational states, phonon assisted processes etc.) and it be trapped inside the potential well, establishing a bond with the surface. The presence of a potential barrier (b) implies the existence of an energy threshold for the activation of gasp particles bonds: in fact if the energy of the impinging molecules is not large enough backscattering or not stable adsorption occur. The energy barrier height depends on the kind of adsorption process: it is in the range of few meV for physisorption, mainly based on weak Van der Waals interactions, while it is in the order of some eV for chemisorption processes (so the potential minimum, where the bond is stable, cannot be reached if the total energy of the interacting system is not high enough). Beyond chemisorption, diffusion is another surface process characterized by an energy activation barrier that can affect the deposition. Considering, for example, a surface constituted by an ordered monolayer: Its regular array form a periodic surface potential, so the sites where absorption is favored are separated by barriers, as sketched in Figure 1-9. Given E_d the height of these potential barriers, the adsorbate particle will have a defined probability of jumping from one site to another (hopping phenomenon) with a rate r,:

$$r = \frac{1}{z} r_0 e^{\frac{-E_d}{KT}} \tag{1.26}$$

Therefore surface diffusion is related to the energy of the adsorbate particle by the Arrhenius form, the typical one for an activated process:

$$D = D_0 e^{\frac{-E_a}{KT}} \tag{1.27}$$

where D_0 is called diffusivity. As hopping and diffusion are processes that can be thermally activated or enhanced, a way to control the formation of different morphologies and structures in films growth is the tuning temperature of the system [13].

1.1.5 Supersonic beams as a novel approach to film growth

We have just depicted only a simplified and schematic picture of the phenomena occurring during gas-surface interactions, as we have neglected, for example, the possible dissociation processes of gas molecules (like structural distortion or configurational changes), the influence of substrate nature and morphology (that could imply a more complex surface potential) and all the processes occurring during the deposition, like energy-loss transitions. But the critical issue, that we want to highlight, is the fundamental role played by the energy of the impinging gas particles: by this point of view supersonic beams techniques are very attractive because of the possibility to control the energy content by tuning the thermodynamical parameters of gas precursors, increasing the overcoming efficiency of potential energy barriers. In this case we can refer to kinetic activated processes. Of course, the kinetic energy must not to be too high, since this could increase the probability of back scattering from the surface.

Thanks to this particular feature, supersonic seeded beams, already known as the ideal environment for molecular scattering and spectroscopy studies, have been recently proposed as new and appealing approach in thin film synthesis. The main idea is that a large and controlled amount of energy can be delivered by the seeded precursors to a localized region of the surface, where it can stimulate chemical processes and surface diffusion. Moreover, by using low divergence and highly collimated beams with a high flux density it is possible to reach growth rates strictly similar to those of MBE, but avoiding the chamber contamination typical of the effusive molecular beams. The interaction between the impinging cluster and the surface can be described by the ϵ value, defined as:

$$\epsilon = \frac{E_K/N}{E_{ch}} \tag{1.28}$$

where E_K is the kinetic energy of the whole cluster, N the number of its atoms or molecules and E_{ch} its cohesion energy. By controlling the energy content of clusters in the beam is possible to tune from soft landing, if the cohesion energy is much higher than the kinetic energy per molecule (i.e. $\epsilon << 1$), to a more energetic impact, where ϵ is typically 4-6. In the first case we will obtain a porous films growth, while the second case will generate cluster fragmentation and/or reactivity phenomena. This kinetic activated reactivity can be also used to generate chemical reactions between

inorganic and organic layers: this is a very interesting feature as it allows the employment of the same material in a wider range of applications, by conveniently changing the sensitizing molecule. The aim of this thesis work is just to show how supersonic beams techniques can be used both for the deposition of organic (phthalocyanine) and inorganic (titanium dioxide) thin films and for the achievement of molecular sensitization processes.

1.2 Nanostructured titanium dioxide: state of the art

Titanium dioxide, known as TiO_2 or titania as well, is a widespread and well-studied material due to its chemical stability, biocompatibility, physical, optical and electrical properties. Since its commercial production in the early twentieth century, titanium dioxide has been widely used as a pigment [28], in paints [29], sunscreens [30], plastic, paper and even in foodstuffs as E171 [31]. TiO_2 nanoparticles are also used as opacifier in textiles, glass and porcelain enamels, pharmaceuticals, cosmetics, skin care products [31–33] and other common stuffs of daily life.
Furthermore, titanium dioxide has excellent photocatalytic properties, as it allows the transformation of light energy into chemical energy [34]. The photocatalytic splitting of water on a TiO_2 electrode under ultraviolet (UV) light has been first observed by Fujishima and Honda in 1972 [35,36]. Since then, TiO_2 has roused increasing interest in the scientific panorama: the first studies have been devoted to the understanding of its photocatalytic processes and to the enhancement of its efficiency [37–41]. This leads to a great number of published works focused on new TiO_2-based catalysts [42–44], and to the spreading of new industrial applications of TiO_2 photocatalysis. The employment of TiO_2 nanoparticles has found to be particularly useful for indoor and outdoor air purification and as water decontaminant from toxic organic pollutants [31–33,45].
The enormous efforts devoted to research on titanium dioxide also paved the way to other different application areas ranging from photovoltaics to photo-/electrochromics and sensors [39,46–48]. Many of them depend not only on the properties of the TiO_2 material itself but also on its interactions with inorganic and organic dyes. Moreover, the large number of research

activities [49–51] in the nanotechnology field shows that new physical and chemical properties are expected when the size of materials are reduced down to the nanometer scale. In fact, the high surface-to-volume ratio of nanoparticles are found to be beneficial to many TiO_2-based devices, as it facilitates reaction/interaction between the devices and the interacting media, which mainly occurs at the surface or at the interface. Here, we focus on the main properties of titanium dioxide that have roused so much interest in the three past decades, giving evidence to the differences between the bulk and the nanostructured material. Particular emphasis is given to the structural, luminescence and electronic properties as they are the subject of all the investigations performed on our TiO_2 samples.

1.2.1 Structural properties

Titanium dioxide exists in several crystallographic forms, such as anatase, rutile and brookite. Anatase and Rutile are the most investigated phases, as their properties are particularly suitable for the aforementioned applications. Figure 1.12 represents their unit cell structures [52]. Both anatase and rutile are tetragonal systems and can be described in terms of chains of TiO_6 octahedra. Each building block consists of a Ti^{4+} ion, surrounded by an octahedron of six O^{2-} ions.

The two crystal structures differ in the distortion of each octahedron and in the assembly pattern of the octahedra chains. In particular, the octahedron shows a slight orthorhombic distortion in the rutile form, while it is significantly distorted in anatase. This implies the presence of larger Ti-Ti distances and shorter Ti-O distances in anatase than in rutile. Moreover each octahedron of the anatase crystalline form is in contact with eight neighbors (four sharing an edge and four sharing a corner). On the contrary, each octahedron in the rutile structure is in contact with 10 neighbor octahedrons (two sharing edge oxygen pairs and eight sharing corner oxygen atoms).

All these differences in the lattice structure cause different properties between the two forms of TiO_2. For example, rutile is the more stable phase at high temperatures, while anatase is more common in fine grained nanoscale natural samples [53]. Concerning the synthetic TiO_2 materials, the crystallization is usually achieved by severe thermal treatments [53]. In fact, the final product of the conventional growth methods, such as sol-gel and

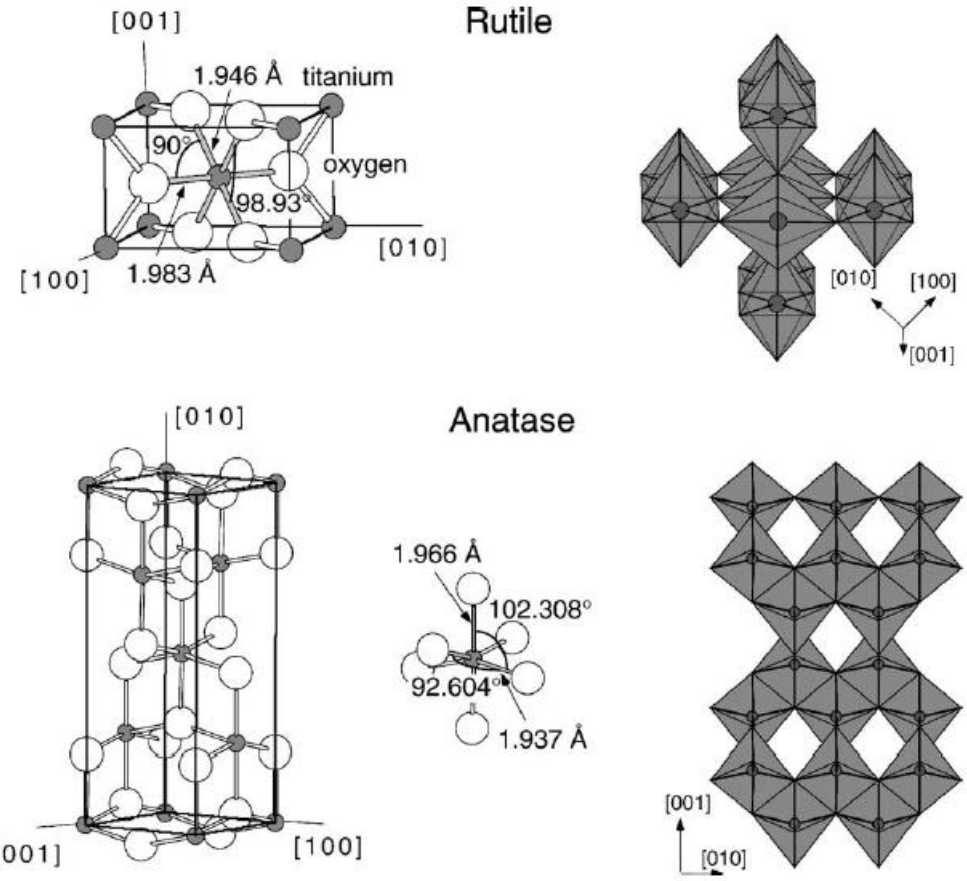

Figure 1.12: Bulk structure of rutile and anatase TiO_2. In both structures, slightly distorted octahedra are the basic building block units. The bonds lenghts and angles of the octahedrally coordinated are indicated and the stacking of the octahedra in both structures is shown on the right side. Taken from [52]

chemical vapour deposition techniques, would be amorphous titania. The transition from the amorphous to the anatase phase is achieved by thermal post-processing at around 500°C, while the anatase to rutile phase transition occurs in bulk crystals at around 900°.

On heating concomitant with coarsening, different phase transformations can be observed, whose thermodynamical sequences depend on the particles size and the preparation methods [44]. For example, Swamy et al. have found that the metastability of anatase as a function of pressure is size dependent, the smaller crystallites being able to preserve their structure at higher pressures [54]. Several theoretical studies about TiO_2 NPs in different environments show the great influence of surface passivation on morphology and phase stability [55–58]. In particular, the surface hydrogenation is found to induce important shape variations in rutile nanocrystals, but not in anatase, and a dramatic increase of the size at which the phase transition might be expected. These thermochemical results could differ as a function of shape, size, and degree of surface passivation [56]. The experimental work of Chen et al. shows the presence of surface lattice distortions in very small (diameter=1.9 nm) TiO_2 nanoparticles [59], that are probably responsible for binding with other molecules. Qian et al. found that the density of the surface states on TiO2 nanoparticles was likely dependent on the preparation methods [60], as the TiO2 nanoparticles prepared from basic sol show more surface states than those prepared from acidic sol.

The most employed diagnostic techniques for the phase identification are Raman or diffraction-based methods. The anatase TiO_2 has six Raman-active fundamentals in the vibrational spectrum: three E_g modes centered around 144, 197, and 639 cm^{-1}, two B_{1g} modes at 399 and 519 cm^{-1}, and an A_{1g} mode at 513 c^{-1} [61]. Rutile shows four Raman active modes with symmetry A_{1g}, B_{1g}, B_{2g}, and E_g, located at 612 cm^{-1} , 143 cm^{-1}, 826 cm^{-1} and 447 cm^{-1}, respectively [62]. As the particle size decreases, the Raman peaks show increased broadening and systematic frequency shifts.

Anatase and Rutile phases can be distinguished in TiO_2 NPs also by observing their X-ray or electron diffraction patterns [63]. The main observable features of rutile are diffractions from the 110, 101, 111 and 211 family planes, having d-spacing of 0.322, 0.253, 0.223 and 1.69 nm, respectively. On the contrary the main diffraction peaks for anatase are related to the

101, 004 and 200 family planes, with lattice parameter of 0.352, 0.237 and 0.189 nm, respectively.

1.2.2 Electronic properties

The fundamental physical quantity that influences the overall behavior of a device is the gap between valence and conduction bands [64]. Two different kind of band-gap can be distinguished: the optical and the electronic one. The former can be determined by light absorption experiments and it is particularly important in energy applications, as it determines the fraction of the solar spectrum absorbed. The electronic gap can be extracted by photoemission experiments and it assumes particular relevance in the electronic charge injection phenomena of solar cells and sensors. These two kind of experiments clearly provide information on two different physical quantities: the photoemission experiment implies a change in the total number of electrons in the material, while the optical-absorption edge studies induce the formation of an electron/hole pair (where the free electron is compensated by the hole). A large number of experimental studies have been devoted to the determination of the optical and the electronic gap of titania. Whereas a general agreement exists in the indirect optical-absorption edge, the experimental value for the electronic band gap still has a large degree of uncertainty. For example, the indirect electronic gap of bulk rutile is found in the range of 3.3-3.6 eV from UPS [65] and IPES [66] studies (Ultraviolet and Inverse photoemission spectroscopy) while there are no reports of the same combined measurements performed on anatase. Also theoretical works have been devoted to the determination of electronic band gaps, by means of density-functional theory (DFT) calculations [67–70]. The DFT is known to give a strong underestimation of the electronic band gaps [71] but the application of many-body corrections allows a quite agreement with the photoemission values. Chiodo et al. show a comprehensive DFT study on the electronic properties of both anatase and rutile, calculating their band structure along the high symmetry directions (Figure 1.13), the density of states, and the spatial behavior of wave functions [64]. The electronic gap is calculated to be 1.93 eV (at the Γ point) for the rutile direct gap and 2.15 eV for anatase indirect gap(from X to Γ). The anatase direct gap is 2.43 eV (at Γ). These values are underestimated by almost 1.5-2.0 eV with respect

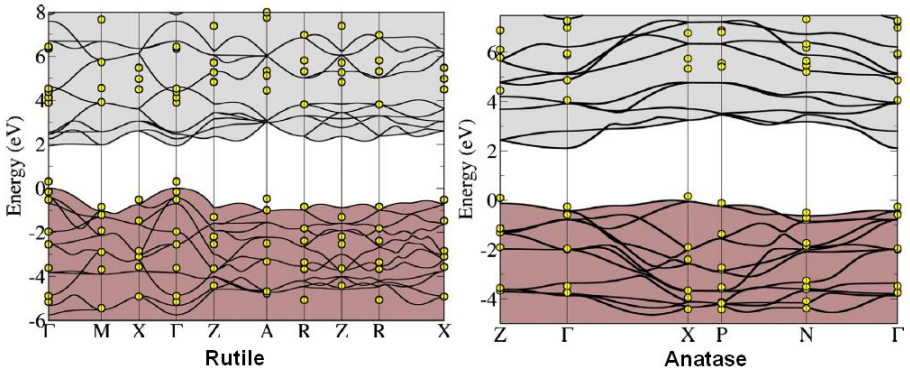

Figure 1.13: Electronic band structure of bulk rutile (left) and anatase (right) along the high symmetry directions of the first Brillouin zone. Black lines and yellow point indicate the employment of different corrections in the DFT calculations. Taken from [64]

to the few experimental data available. The application of a multi-body correction gives a resulting electronic direct gap of 3.59 eV for rutile, while the direct and indirect gaps for anatase are estimated to be 4.29 and 3.83 eV, respectively. The rutile electronic gap is in good agreement with the aforementioned experimental estimations of 3.3 -3.6 eV [65, 66]. The electronic gap of both phases are definitely larger than their experimental optical gap of 3.0-3.2 eV [72, 73], as expected. The spatial distributions of the wave functions for TiO_2 valence and conduction bands are represented in Figure 1.14. They highlight the strong ionic character of the material: the valence band of TiO_2 consists mainly of O 2p states partially hybridized with Ti 3d states, while the the conduction band is constituted by metal 3d states with a small amount of mixing with O 2p states [64].

Figure 1.15.A represents the density of states (DOS) of anatase TiO_2, composed of Ti orbitals with e_g and t_{2g} (d_{yz}, d_{zx}, and d_{xy}) symmetry, O p_σ and O p_π. The vertical dashed line represents the bottom of the conduction band. As previously mentioned, the valence band is mainly related to oxygen orbitals and it can be divided into three regions: the lower energy region of σ bonding, due to O p_σ orbitals, the π bonding in the middle region and the higher energy region of O p_π non bonding states (where the hybridization with d states is almost negligible). The contribution of the π bonding is much weaker than that of the σ bonding. The conduction band consists of

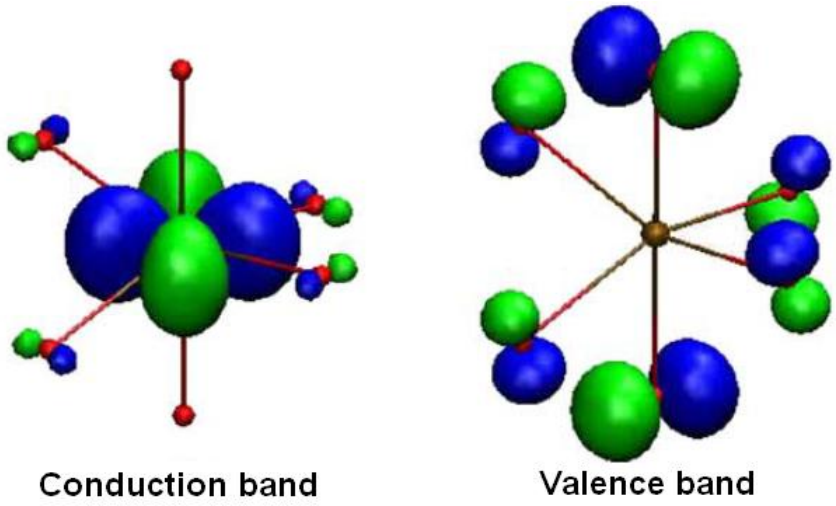

Figure 1.14: Wave functions for titania valence and conduction bands at the Γ point. Taken from [64]

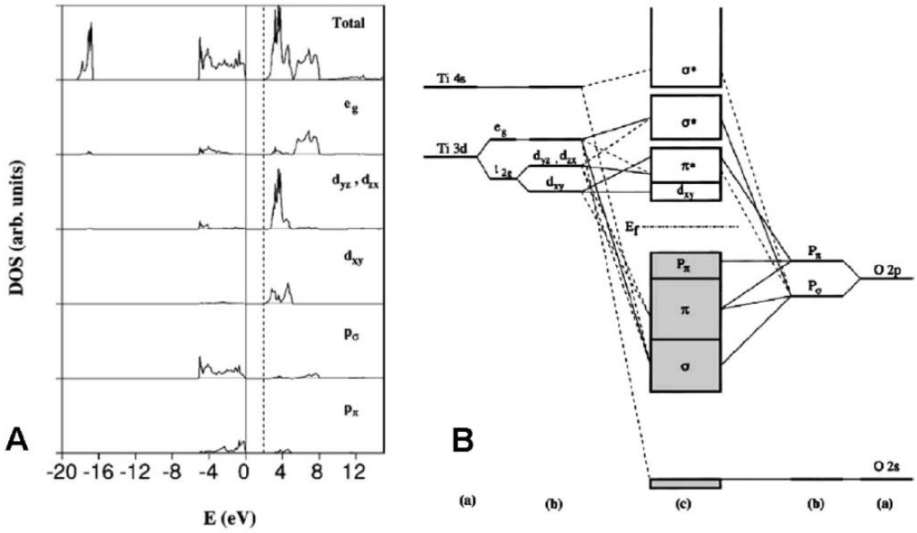

Figure 1.15: A) Total and projected densities of states (DOSs) of the anatase TiO2 structure. (B) Molecular-orbital bonding structure for anatase TiO2: (a) atomic levels; (b) crystal-field split levels; (c) final interaction states. The thin-solid and dashed lines represent large and small contributions, respectively. Taken from [74]

two regions, composed of Ti t_{2g} bands below 5 eV and of Ti e_g above 5 eV. The d_{xy} states are mainly located at the bottom of the CB, while the rest of the Ti t_{2g} states, are antibonding with p states.
Figure 1.15.B shows the anatase molecular-orbital bonding diagram, that highlights the presence of non-bonding states near the band gap (p_π in VB and d_{xy} states in CB. Slightly differences can be observed in rutile, due to the different packing of the ochtaedron [64]. In fact, the ochtaedra form linear chains in rutile and zigzag chains with a screw axis in anatase. This results in a lower density of anatase than rutile. Also, anatase has a large metal-metal distance of 5.35 Å, so its Ti d_{xy} orbitals at the bottom of the conduction band are quite isolated. On the contrary, the d_{xy} orbitals provide metal-metal interactions, due to a smaller Ti-Ti distance (2.96 Å).
Furthermore, titanium dioxide is known to be easily reduced in TiO(2-x) [52]. The deviation from stoichiometry induces in titanium dioxide two kind of defects: double charged oxygen vacancies (V_o) and Ti^{3+} and Ti^{4+} interstitials. These defects are localized in both bulk and surface and can be subjected to diffusion mechanism, as the oxygen atoms can migrate via vacancy diffusion and Ti atoms can diffuse as interstitial atoms (especially through (001) direction). The concentration of oxygen vacancies at surface is particularly influenced by the employed synthesis process, as it is increased by vacuum annealing treatments, while it is reduced after exposure to molecular oxygen gas [52]. The role of V_o in surface processes, such as dissociation of organic molecules or stabilization of supported metal clusters, is well recognized [52] and it may assume very high relevance in TiO_2 Nps, due to their high surface-to-volume ratio. The presence of defect structures should affect the electronic properties of non-stoichiometric titanium dioxide, however, it is not clearly evident if intrinsic doping produces isolated energy levels inside the band gap or produce energy states that merge with the valence or conduction band to produce a concrete band gap reduction. The presence of defect point can be observed by photoemission spectroscopies in the formation of intra-gap levels at 0.8 eV below the Fermi edge in the UPS spectrum [75,76] or of a shoulder in the XPS Ti2p peak [77]. However, the defect state in the band gap is not reproduced by all theoretical calculations. For instance, the work of Munnix et al shows that the bulk V_os don't induce any energy level inside the gap of rutile, rather lead to a pinning of the Fermi level near the

CB edge [78]. In contrast, Ramamoorthy et al. found that the structural relaxation related to the presence of oxygen vacancies is responsible for introducing defect energy level at 0.3 eV below CB [79]. Cho et al confirm that the effectively positive charges of the vacancy site can act repulsively with nearby cations, inducing structural relaxation. Moreover they found that oxygen vacancy does not give rise to a defect level within the energy gap while the titanium interstitial creates a localized state 0.2 eV below the conduction edge [80]. Even if the theoretical formalization is still a subject of debate, the nature of defect levels can be easily explained: the removal of neutral oxygen atoms leaves behind two electrons, which previously occupied O2p levels in the VB. Therefore, the presence of oxygen vacancies acts as a n-type dopant. [52].

1.2.3 Luminescence and optical properties

The optical properties of TiO_2 are of great importance for the behavior determination of photocatalytic and photovoltaic devices. The indirect optical gap has been determined to be 3.05 eV for rutile [72] and 3.2 eV for anatase [73] by absorbtion measurements. These values are referred to phonon assisted indirect transitions occurring in bulk materials. The first dipole allowed gaps have been measured at 4.2 eV for rutile [82] and 3.68-3.80 eV [83,84] for anatase. Urbach tails are found in the absorbtion edge of anatase, ascribable to self-trapped excitons [85]. An exciton results from the interaction of an electron in the CB (Ti 3d states) with a hole built essentially on oxygen 2p states. The exciton can be localized on a TiO_6 octahedron if its transfer towards the neighbor sites is not energetically competitive. The exciton self-trapping phenomenon is then related to how compactly the octahedra are condensed in the crystalline structure. Differently from the case of anatase, rutile shows only free excitons, due to its close-packed structure [85]. It is well-known that the band gap energy increases in nanoparticles and that the energy band becomes more discrete with decreasing size [86,87]. As the size of a semiconductor nanoparticle falls below the Bohr radius of the first excitation state or becomes comparable to the de Broglie wavelength of the charge carriers, the charge carriers begin to behave quantum mechanically and the charge confinement leads to a series of discrete electronic states [88]. Quantum size effect is not common in nanosized TiO_2 because of the high

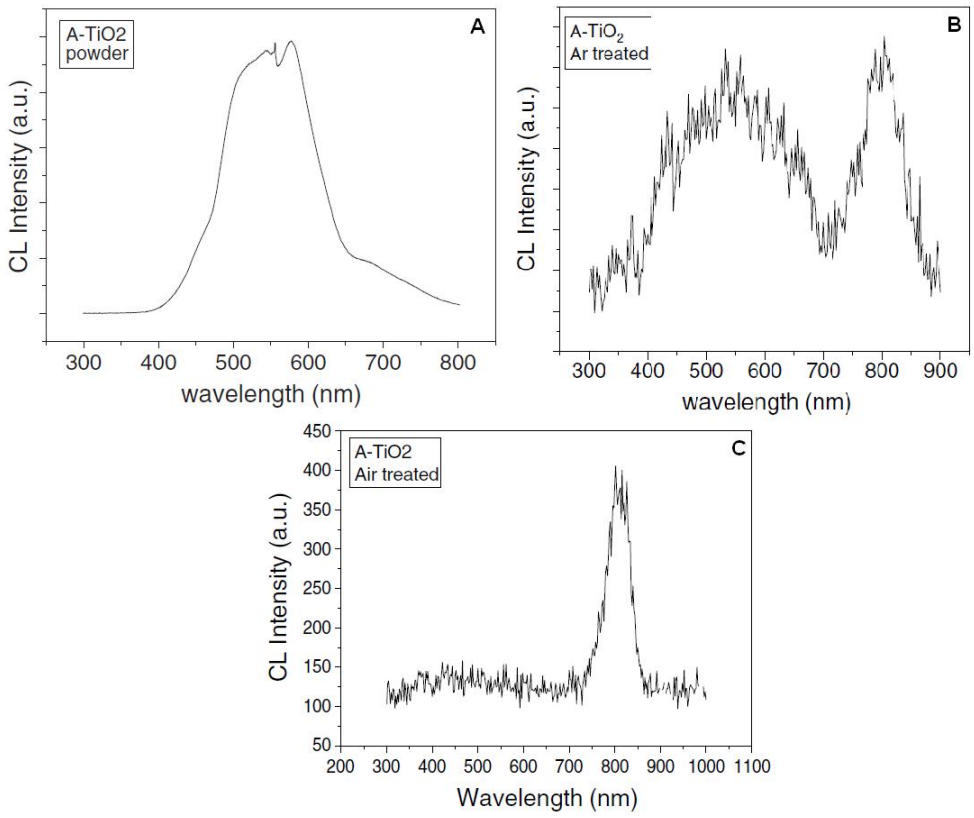

Figure 1.16: CL spectra of initial anatase powders (A) and anatase samples formed by treatment of powders at 1100°C in Ar (B) and in air (C). Taken from [81]

effective mass of carriers and the small exciton radius (0.75-1.90 nm) [86]. In fact, Kormann at al. found a small band gap blue shift only in TiO_2 particles with size down to 2 nm [86], while the blue shift phenomena observed by Serpone et al. in TiO_2 NPs with sizes of 2.1, 13.3, and 26.7 Å, have not been attributed to quantum confinement effects [89], but to direct transitions. Monticone et al. did a comprehensive study on the quantum size effects in anatase nanoparticles and found no quantum size effect for sizes $\geq$ 1.5 nm, but they observed unusual variation of the oscillator strength of the first allowed direct transition with particle size [90].

Luminescence studies are also very useful as they give information about the optical levels involved by radiative processes. The most common emission of titanium dioxide is a broad and weak band in the visible region (Fig-

ure 1.16.A). This emission band has been observed in both bulk [91] and nanostructured [92] TiO_2 by photoluminescence (PL) [92] and cathodoluminescence (CL) [91,93] studies and it is attributed to radiative recombinations via the oxygen vacancies which presumably reside at surface [93]. Piqueras and Plugaru performed several CL studies [81, 91, 93] at different annealing conditions, in order to understand the optical emission spectra on anatase and rutile powders and bulk crystals (see Figure 1.16). The visible emis-

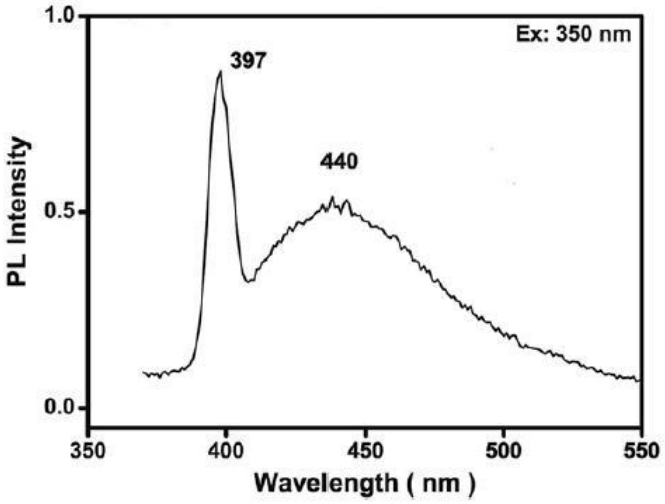

Figure 1.17: PL spectra of colloidal TiO_2 nanoparticles. Taken from [94]

sion is observed for both phases within the 2.75-2.15 eV range [91] (Figure 1.16.A). The treatment in oxygen at 800 °C of TiO_2 sintered ceramics showed that some of the defect centers are sensitive to oxygen [81]. In particular, blue luminescence peaked at 2.75 eV becomes the dominant emission in the visible region after treatment in oxygen, suggesting that the de-excitation process is assisted by a shallow trap associated with a vacancy of oxygen. Further infrared emissions at 1.54 eV and 1.51 eV have been observed in samples sintered at high temperatures (1000-1100 °C) and are associated with Ti^{3+} interstitial ions [91] (Figure 1.16.B and C). The emissions related to Ti^{3+} ions and to oxygen vacancies show a correlated behavior as the formation of one vacancy can generate two Ti^{3+} defects.

Finally, a very few works report also the presence of near band edge emissions in the ultraviolet region (Figure 1.17). The UV emission in not so common in titanium dioxide, as the presence of oxygen vacancies generally

constitutes a preferential channel for radiative recombinations.
The first observation is reported by Haart and Blasse in 1986, that found a strong peak at 3.01 eV in Rutile bulk crystals and ascribed it to a free exciton emission [95]. Also other studies, performed on a wide range of titania materials, such as rutile nanowires [96], anatase [97,98] and rutile [98] thin films, ascribed the observed UV emissions to excitonic transitions. Further, several groups have observed the presence of UV emission in titanium dioxide also at room temperature [94,99,100].

1.3 Phthalocyanines: a class of interesting π-coniugated molecules

Recently, organic molecules are considered increasingly promising in device technology, thanks to the possibility of fine tuning their electro-optical properties added to a great structural flexibility [101] [102] [103]. Although phenomena like charge injection, molecule-substrate or intermolecular interactions are crucial in the determination of the optical and electrical properties, detailed investigations on the interdependence of these features are rather limited. Therefore, the nodal point is to understand the role of the electronic structure in the determination of the material characteristics, in order to obtain the desired electronic properties by controlling the growth processes [104] [105] [106]. Among the great number of organic molecules, the family of the phthalocyanines (Pc) is one of the most attractive candidate for UHV deposition of organic thin films, due to their chemical and thermal stability. While the first industrial application of Pc was just as dyestuffs for textiles and inks, nowaday their technological potential ranges over a wide variety of applications, such as intrinsic semiconductors, chemical sensors, materials for nonlinear optics or laser recording, OLED, photovoltaic cells [107] [108] [109].
Phthalocyanines are planar (or quasi-planar) macrocycles, related to porphyrins: they are constituted by four pyrrole-like rings, linked by nitrogen atoms and sharing each one two carbon atoms with a benzene ring (Figure 1.18). This structure shows highly delocalized $\pi-$conjugated molecular orbitals, which make these complexes suitable for several fields in material science; by varying this π-electron delocalization it is possible for example

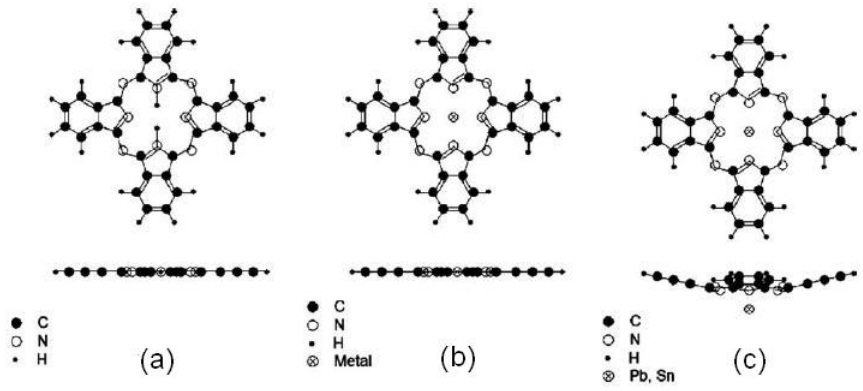

Figure 1.18: Top and side view of free-base phthalocyanine (a), as well as planar (b) and non-planar (c) metallophtalocyanine.Taken from [110]

to tailor and modify the Non Linear Optical (NLO) response, as in Naphthalocyanine systems.

Another remarkably feature of these molecules is their great versatility: as shown in figure 1.18.a, the coordination number of the square-planar Pc is four, thus more than 70 elements are suitable for replacing the H atoms of the central cavity, allowing a very large tuning of physical properties. Then most common structural formula related to metallophthalocyanine (MPc) is represented in Figure 1.18.b, but according to the size, the oxidation state and the coordination number of the element, different configurations could be achieved: in the case of alkalines, even two atoms may be included into the Pc core, while metals with higher coordination number results in pyramidal, tetrahedral or octahedral structures.

Besides, phthalocyanines show a rich optical absorption spectrum in the visible and ultra-violet spectral range, whose features depends on the presence and the nature of the metallic center (see next subsections). Concerning the conducting properties, phthalocyanines molecules are considered as p-type semiconductors, for this reason are suitable as hole-carrier transport layer in photovoltaic devices [109].

The typical direct energy gap is about 1.8 eV and the conductivity ranges usually between 10^{-12} and $10^{-4} Sm^{-1}$ [110].

Both electrical and optical properties of phthalocyanine molecules depend strongly on their structural configuration, so in next sections we will describe

the peculiar case of copper and free-base phthalocyanines, the molecules used in this thesis work. Afterwards, we will give a brief introduction about the growth mechanisms of organic thin films and the sensitization processes, paying attention to the innovative features introduced by Supersonic Molecular Deposition methods.

1.3.1 Copper and free-base phthalocyanines

The copper phthalocyanine (CuPc) is a metallophthalocyanine, where the center of the molecule is occupied by a copper atom. In literature several crystalline structures of CuPc have been reported as $\alpha, \beta, \gamma, \delta, \epsilon$ polymorphs and mixtures of them, depending on the preparation conditions. The first two are the most common for UHV depositions, in particular the former is the preferred phase for sublimation pressure lower than 10^3 Pa and it is stable for temperature up to 210°C (after which it turn into β-CuPc polymorph).

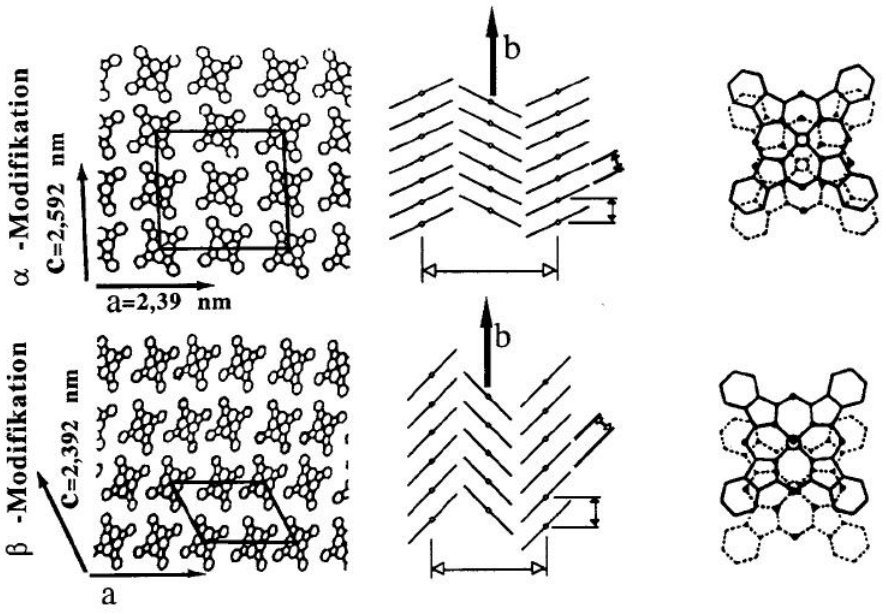

Figure 1.19: Molecular arrangement of CuPc α and β polymorphs

The two phases show also different crystalline structures, due to the different stacking among molecules and a dissimilar tilt angle of alternating arrangements: in particular α-CuPc has cubic form, while β-CuPc crystallites are

long needle-shaped. Moreover, the crystalline structure changes by increasing the molecular coverage: in the presence of strong surface interaction, the molecules lie flat on the surface for the first 1-2 monolayers, then the strain release occurring for further layers gives rise to a columnar molecular arrangement.

The crystalline structures and arrangements of α and β polymorphs are shown in Figure 1.19. In both modifications the molecules face each other to form closely packed column, but the higher tilt angle of the β-CuPc results in a higher film stacking density.

The $\alpha \rightarrow \beta$ transition takes place for substrate temperatures above 250°C: as a consequence of this, if the deposition activation energy is obtained by means of thermal treatments, the α-phase molecules formed during the sublimation in UHV conditions, turn into the β polymorph. Polymorphs stability and transitions are still a matter of study and debate, because of the tendency of Pc to grow in polycrystalline and mixed-phase forms, rather than in ordered single crystallites. Concerning the optical properties, copper phthalocya-

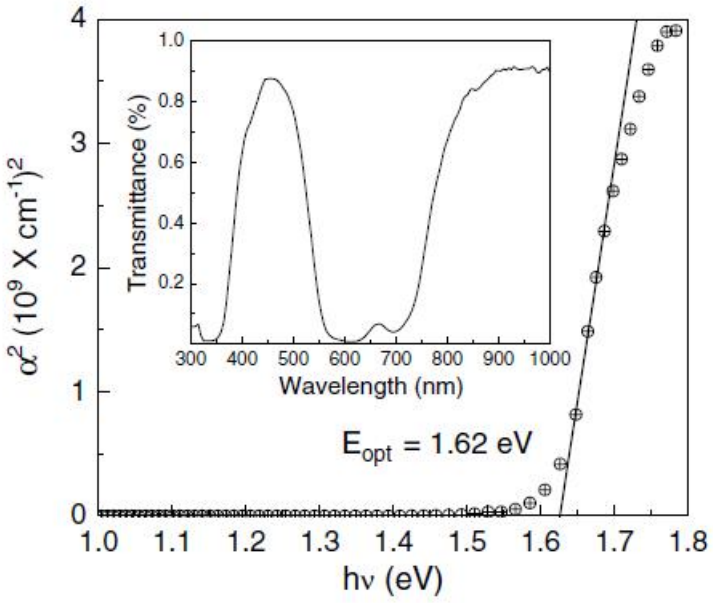

Figure 1.20: Plot of α^2 versus energy and calculation of the optical gap for CuPc thin film evaporated at substrate temperature of 30°C. Inset: optical transmittance of the same sample.Taken from [111]

nines thin films show absorption coefficients higher than $5 \times 10^{-5} cm^{-1}$, for photon energies upon the energy gap In figure 1.20 is shown the typical absorption coefficient behavior of CuPc reported by Della Pirriera et al. [111]. The calculated band gap is around 1.62 eV. The exponential decreasing in the optical absorption at 1.7 and 1.5 eV indicates the presence of band tails, similarly to the case of microcrystalline inorganic semiconductors, while the absorption phenomena occurring in the sub-gap region are usually negligible and are ascribed to structural defects in the material. moreover in the inset is represented the transmittance spectrum in the visible region, showing two distinct absorption bands located around 2 eV (Q-band) and 3.5 eV (B- or Soret band). These bands are related to the $\pi \longrightarrow \pi$ transitions of the macrocyclic π-system [112], [113], while the two absorption peaks observed in the near-infrared region are assigned to copper absorption bands.
Thanks to the aforementioned features, metallophthalocyanine and in particular copper phthalocyanines are considered very attractive for a wide range of applications so they have been extensively studied. On the contrary metal-free phthalocyanines show features that are less interesting from the opto-electronic point of view, so they have been less investigated and really few properties are really proven. For example, as it concern the absorption spectrum, it is known that the lower symmetry of H_2Pc delete the degeneracy of LUMO orbitals, inducing a complete splitting of the Q-band in the visible region [114] [115] (instead of the intense and almost featureless Q-band typical of MPc), but at the best of our knowledge, there are no reports about the optical band gap. Afterwards, one of the aim of this thesis work is to wide the knowledge about this molecule, especially from the electronic point of view, in order to better understand the real influence of the metal core during the sensitization processes.

1.3.2 Growth of molecular thin films

The concept of epitaxial growth is closely related to inorganic thin films: it consist on the arrangement of adsorbate layers upon a crystalline substrate, where the order degree of the growing structure depends on the interactions and the re-arrangement processes occurring at interfaces. Molecular Beam Epitaxy (MBE) methods have been extensively developed in the last 50 years, as the presence of well-ordered structures typically enhances the

charge transport properties, as well as the final performances of inorganic electronic devices. On the contrary, during the deposition of organic films, most part of the interactions involved are Van der Waals like (VdW), too weak so that the adsorbate layer follows a fixed, long range order given by the substrate. Epitaxy phenomena in organic materials have been just observed in small areas and in the first interface layer; the following layers usually experience forces induced by the overlapping of delocalized molecular orbitals, rather than punctual interactions with a single atomic layer. The so-formed bonds range from weak physisorption up to strong chemisorption, so that the resulting film usually shows high disorder and low density. Moreover, the polymorph nature of most molecular bulk form makes the achievement of a uniform organic structure even more difficult.

For all these reasons, we will refer to all the vacuum evaporations and MBE-like approaches for organic material growth, as a more general *Organic Molecular Beam Deposition* (OMBD), in order to not induce misunderstandings. By the way, there are other growth techniques for organic film deposition, all related to wet chemistry (dipping, sol-gel), but there will not be treated here.

The main OMBD growth parameters are the molecular arrival rate, the substrate temperature and the deposition geometry. In other respects, the organic precursor kinetics can be hardly controlled because it is related to the specific sublimation/evaporation temperature of the molecule of interest. If the molecule kinetic energy is usually in the range of few tens of meV, the momentum is often undefined, as it is related to the internal energies in terms of roto-vibrational modes. Therefore the impinging molecule can assume a large variety of orientations and, in the case of low molecular mobility on the surface, the achieved morphology is typically high disordered, showing dendritic structures, defects and high anisotropy.

In order to improve the organic film quality, the critical issue is the achievement of a control on the precursors kinetics, as it would allow the enhancement of mobility and the formation of new chemical bonds, structural relaxations and interactions processes at interfaces. In this way, the film growth would be ascribed not only to merely equilibrium thermodynamics but also to kinetically activated phenomena at the surface. Conventional OMBD techniques, based on vapour phase, do not allow the aforementioned control

on precursors kinetics; this would be a prerogative of sputtering methods, but the high energy involved can not be applied to deposition of molecules, being highly destructive for organic materials.
As discussed in section 1.1, the desired control on kinetics can be achieved by means of supersonic beams seeded by organic precursor, paving way to growth of ordered organic films. Three different kind of molecular film growth

Figure 1.21: Different kind of molecular film growth: (a) layer by layer deposition, (b) islands formation and (c) a combination of two former cases.

can be achieved by OMBD, depending on the interaction processes occurring at the interface, on the morphology of the substrate and on the geometry of the molecules:

- the Frank van der Merwe growth consist in a layer by layer deposition, where the upper sheet start to form after the completion of the previous ones (Figure 1.21.a). This phenomenon occurs when the adsorbate-surface interactions are stronger than the intramolecular ones. The resulting structure is a bi-dimensional film.

- Volmer Weber growth occurs when the adsorbate-adsorbate interactions are stronger than any others, so that the molecules tend to aggregate to form three dimensional structures, called island (Figure 1.21.b),

without the achievement of a complete substrate coverage.

- the Stranski Krastanov is the most common growth and consist in a combination of two former cases: initially the molecules begin to grow layer by layer then, when the influence of underlying substrate becomes weaker, their arrangement assume the aforementioned island configuration (Figure 1.21.c). The number of bi-dimensional layers is usually no more than three and is commonly called called a *wetting layer*.

1.3.3 Molecular sensitization processes

In Material Science, the concept of *sensitization* is used to point out all processes that make a certain material "sensitive" to a peculiar phenomenon or, in other words, it indicates the way of tuning a selected property of a material in order to render it suitable for a specific "function". The sensitization process, called *functionalization* as well, is achieved by creating chemical interactions between two materials, whose electronic structures fit well together for the desired application.
In particular we want to focus our attention to the case of hybrid structures, where the core of the device is constituted by an inorganic material having semiconducting properties (like, in our case, TiO_2), while the "sensitizer" is chosen among organic molecules (like CuPc). Note that this process is based on the creation of stable chemical bonds between two different materials, so it is related to a phenomenon occurring just at the surface and interface between inorganic and organic; this means that sensitization efficiency can be really improved handling on nanostructured materials, where the surface-to-volume ratio is maximized.
The sensitization process is commonly achieved through wet chemistry methods, so it cannot be performed during the growth of the nanostructured semiconductor, but it is usually carried out in a following, separated step.
Considering our specific case, it is known that the synthesis of TiO_2 NPs always requires severe post-annealing treatments in order to activate the crystallization (see section 1.2); as the involved temperatures could damage the intermolecular structure of the organic sensitizer, the functionalization of TiO_2 NPs need to be performed in a subsequent stage. In this scenario, the peculiar features (section 1.1) of SuMBD techniques become increasingly

appealing for the deposition of hybrid structures: as already mentioned, the high kinetic energy involved in a supersonic expansion entails, on one hand, the synthesis of nanocrystalline TiO_2 thin films without any further thermal annealing and, on the others, the activation of chemical bonds between inorganic and organic layers. Hence the SuMBD methods allow both materials growth and *in-situ* sensitization, that can also be achieved simultaneously, by performing the co-deposition of the semiconductor oxide and its sensitizing molecule [25].

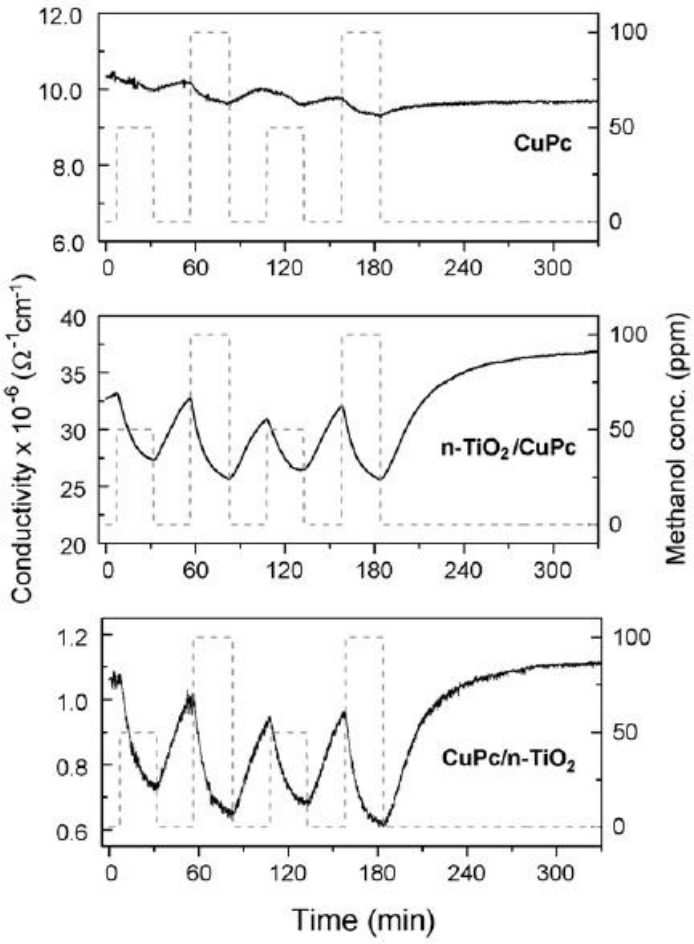

Figure 1.22: Dynamic response of hybrid and pure CuPc sensors at T=75°C to methanol in cycles of exposures of 50 and 100 ppm. Taken from [116]

Pc/TiO_2 hybrid devices

Hybrid devices are particularly suitable, among the others, for sensing, biomedical and photovoltaic application fields. Concerning the former two, hybrid structures are very appealing for their great selectivity and sensitivity, that can be tuned by modifying the hybrid architecture or the sensitizer molecules.
Emblematic examples are given by ref [116] and [117], where the authors proposed different solutions for MPc/TiO_2 gas sensors, achieved through supersonic beam methods.
In [116] CuPc/TiO_2 thin films have been achieved on alumina substrates with gold interdigitated electrodes. The devices response towards methanol, in terms of changes in conductivity, has been tested at different working temperatures and compared to those of pure CuPc and titania films (Figure 1.22). The novel hybrid devices demonstrated improved sensitivity performances with respect to pure organic sensors and a more reliable and stable behavior even at low temperature (where the nanostructured TiO_2 sensors are not functional at all). Moreover, taking advantages of the peculiarity of the deposition techniques, two different hybrid architectures have been tested: a CuPc layer over an oxide one, and viceversa (Figure 1.23 (a) and (b, respectively)). The different responses are reported in Figure 1.22 (b) and (c) and show that the configuration with CuPc in the upper layer is more desirable because of the higher conducibility.
Even the results reported in [117] for ZnPc/TiO_2 films confirm the advantages of hybrid sensors with respect to pure MPc devices. Nevertheless, by comparing these works, several differences between the two molecules have been observed: the effect of the sensitivity enhancement of the hybrid structure is found to be less evident in ZnPc-based sensors, as (concerning the pure substances) ZnPc has shown a lower response to methanol than CuPc. On the other hand, ZnPc/TiO_2 devices showed better recovery properties with respect to CuPc/TiO_2 sensors.
The use of dye-sensitization in photovoltaics has been inspired by the energy and electron transfer mechanisms in natural photosynthesis and in dye sensitized silver halide emulsions used for photography, but remained rather unsuccessful until a breakthrough in 1991. As a matter of a fact, the Dye Sensitized Solar Cells technology originated from the work of Grätzel et al. [46],

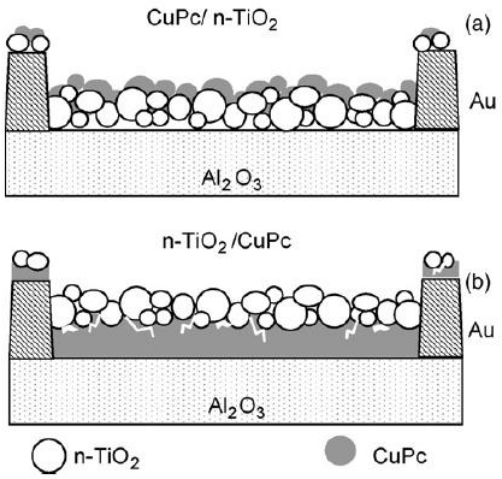

Figure 1.23: Sketch of the two different architectures explored in [116]: (a) $CuPc/TiO_2$ and $TiO_2/CuPc$.

wherein an efficiency of 7.1% has been obtained with a successful combination of nanostructured and mesoporous electrodes and efficient charge injection dyes. In Figure 1.24 is sketched the configuration and principle of operation of a typical Grätzel cell: the impinging light cross the transparent front-electrode and is absorbed by the dye sensitizer, inducing the photo-excitation of an electron in the Lowest Unoccupied Molecular Orbital (LUMO) and of a hole in the Highest Occupied Molecular orbital (HOMO). At the organic/inorganic interfaces the charge separation takes place and the electron is fast injected from the LUMO of the dye into the conduction band (CB) of the wide band oxide. The electron is transported through the porous structure of the semiconductor and collected from the front electrode. The fundamental state of the dye is subsequently regenerated by electron donation from the iodide ion (I^-) of the electrolyte solution, that turn into triiodide ion (I_3^-). The electrolyte solution is restored by the reduction of triiodide at the counter-electrode. The voltage generated between the electrodes under illumination corresponds to the difference between the Fermi level of the electron in the solid and the redox potential of the electrolyte [118].

The most attractive features of DSSC technology for industrial applications are the low cost and the ease of processing, so great efforts have been done

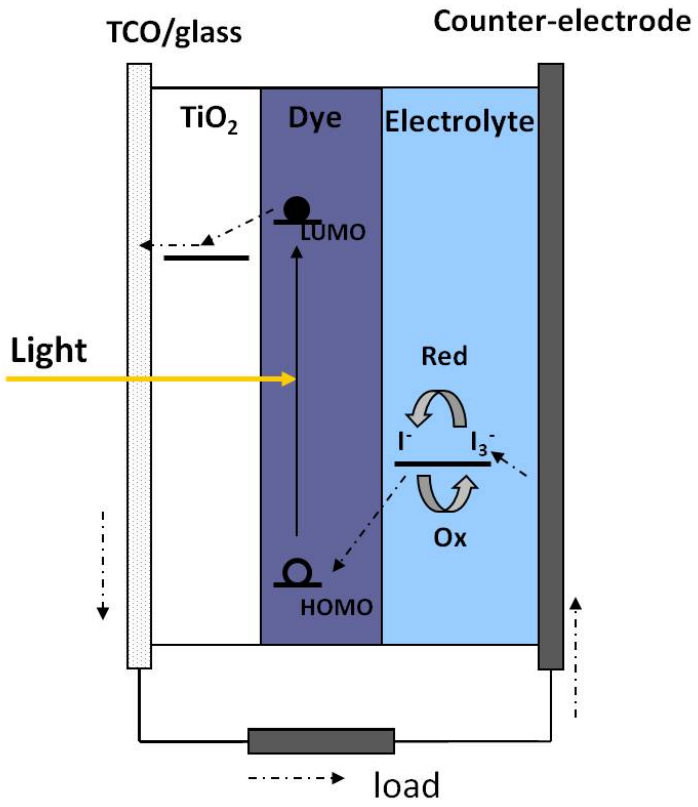

Figure 1.24: Principle of operation of a dye-sensitized nanocrystalline solar cell. Photo-excitation of the sensitizer is followed by electron injection into the conduction band of the mesoporous oxide semiconductor. The dye molecule is regenerated by the redox couple, which itself is regenerated at the counter electrode by electrons passed through the load.

from 1991 by research to reach a real efficiency improvement. The heart of the matter is to find the right synergy between the semiconductor structure and morphology, the dye photo-physics and the electrolyte redox chemistry (see [118] and references therein). Although alternative wide band gap oxides, such as ZnO, and have been investigated, titanium dioxide has been confirmed to be the semiconductor of choice for its low cost, wide availability and non-toxicity. Nevertheless its low conductivity is a limitation to cell efficiency, so further theoretical and experimental effort are needed to understand the involved charge percolation process and to find more suitable nanostructure or functionalized systems [119] to improve the electron mo-

bility. On the other hand, much of the research in dye chemistry [120] is devoted to the identification and synthesis of dyes, matching the following requirements: light absorption just below a threshold wavelength of about 920 nm, good energy level alignment of the LUMO with the oxide CB (in order to maximize the efficiency of electron injection process) and a sufficient stability to guarantee about 20 years of exposure to natural light.
However, the real challenge of the actual studies is to make a full solid-state DSSC [121], in order to overcome the encapsulation problems posed by the use of liquid electrolyte and to offer more stable performances. Obviously in a full solid-state DSSC a solid hole-carrier layer should be chosen to replace the task of the liquid electrolyte. Metallophthalocyanines and in particular CuPc are particularly interesting for DSSC application as they can assume both functions of dye absorber and p-type semiconductor, thanks to their peculiar optical and electrical properties (see previous paragraphs).
Recently Coppedé and co-workers investigated different configurations of CuPc/TiO_2 solid-state DSSC, completely achieved by supersonic beam techniques [25]. The advantages of the SuMBD methods have been explored, by comparing cells showing a sharp CuPc/TiO_2 junction with those provided with an intermediate co-deposited layer. In the latter configuration an enhancement of the photocurrent of a factor of 45 and of the efficiency of a factor of 40 have been observed. In figure 1.25 the J-V characteristics, in both linear and logarithmic scale, have been represented for the both architectures. This study pave the way to new perspectives in the use of supersonic deposition methods in photovoltaic field, as it allows the fabrication of new hybrid device configurations as well as a more efficient sensitization.
The final aim of this thesis work is just the investigation of the molecular sensitization processes occurring at the CuPc/TiO_2 interface, achieved by supersonic beam methods.

1.4 Diagnostic techniques adopted for material characterization

The aim of this section is the description of the diagnostic techniques used in this thesis work. Considering the wide range of the employed analysis techniques, as well as their wide spread in materials science, we will just

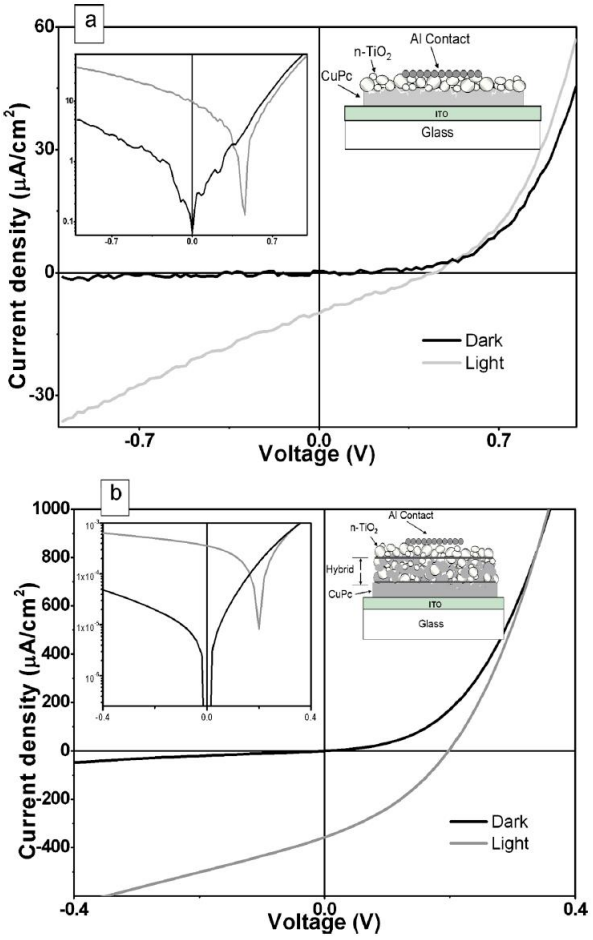

Figure 1.25: (a) J-V characteristic of ITO/CuPc/TiO_2/Al solar cell in dark (black) and in light (gray). Top-left inset: the logarithmic scale of J with respect to V using the same dimension units. Top-right inset: a sketch of the cell geometry. (b) J-V characteristic of ITO/CuPc/Hybrid/TiO_2/Al solar cell in dark (black) and in light (gray). Top-left inset, the logarithmic scale of J with respect to V using the same dimension units. Top-right inset: a sketch of the cell geometry. Taken from [25]

introduce the fundamentals of each method, giving evidence to the experimental apparata and the facilities used in this work.

1.4.1 Morphological analysis by SEM

A scanning electron microscope (SEM) is a microscope, where the images from the sample are obtained by scanning it with a energetic beam of electrons in a raster scan pattern. Once the high-energy electron beam hit a solid surface, a wide range of signals are produced by elastic and inhelastic scattering with the matter (Figure 1.26). A large variety of information (morphological, structural, chemical, electrical..) about the material can be obtained by collecting the different signals. The most common imaging mode uses the secondary electrons ejected from the specimen, as a consequence of inelastic scattering interactions with the electron beam. Due to their low energy (<50 eV), these secondary electrons originate within a few nanometers from the sample surface, giving information on the specimen morphology. In our

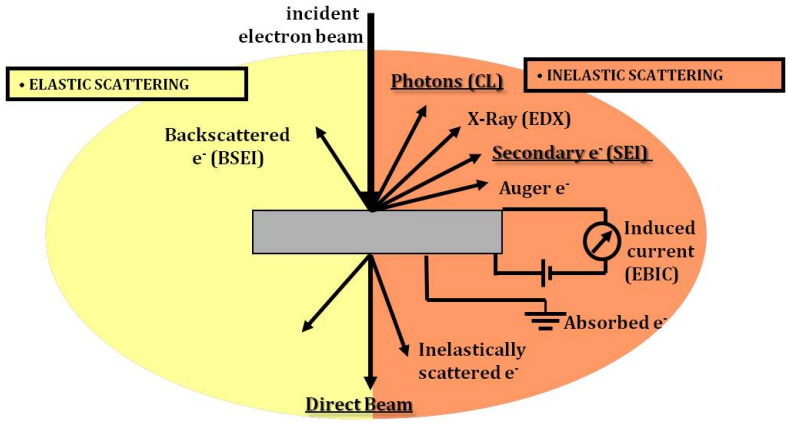

Figure 1.26: Electron interaction with Matter

work we used a Cambridge 360 Stereoscan SEM with a tungsten filament. The resulting beam size on the sample surface typically ranges between a few microns and a few tens of nanometers. The electrons are detected by an Everhart-Thornley detector, that is a kind of scintillator-photomultiplier system. The whole SEM column is kept in vacuum at 10^{-6}-10^{-7} torr by rotary and turbomolecular pumps.

1.4.2 Luminescence analysis by CL

The cathodoluminescence (CL) technique is based on the collection of the photon emitted as a consequence of the interaction between high-energy elec-

tron and matter (Figure 1.26). In semiconductors, the excitation by highly energetic electron beam generates electron-hole pairs within the specimen volume. The excess carriers then thermalize and diffuse inside the material and finally recombine, either by non radiative processes or by photon emission. As shown in Figure 1.27, two different kind of radiative transitions

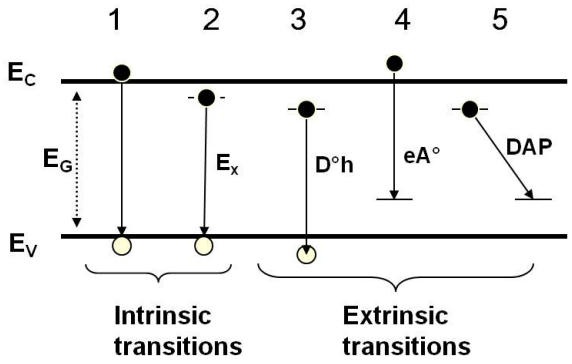

Figure 1.27: Schematic diagram of radiative transition occurring in a semiconductor

can be distinguished: the intrinsic and the extrinsic luminescence. The first one is due to recombination of electrons and hole across the fundamental energy gap, by interband transition from the bottom of the conduction band to the top of valence band. The second one is related to radiative emission involving states in the band-gap, shallow or deep, mainly due to native defects and impurities acting as a donor or acceptor centers. Several recombination processes between trapped and free carriers can occur, indicated as free-to-bound or donor-to-acceptor pair (DAP transition). The photons emitted during the radiative processes propagate inside the material and, a fraction of them, come out of the specimen. The resulting intensity of the recorded CL signal depends on several factors, such as the CL detection system response and internal losses due to scattering/absorption processes of light along its path within the material. The cathodoluminescence set-up used in this thesis work is mounted on the Cambridge Stereoscan360 SEM previously described (Figure 1.28). The photons coming out from the specimen are collected by a parabolic mirror. A light guide carries the signal to the Gatan monoCL2 detection system, located outside the microscope. Here the signal is detected by means a monochromator equipped by a grating

for light dispersion and a multi-alkali photomultiplier sensitive in the range 350 - 830 nm (3.6 eV - 1.5 eV). The sample temperature can be changed from 300 to 6 K, in order to improve the CL intensity and to separate contiguous emission peaks. Different kinds of CL analyses can be performed with this standard setup: the spectral analysis, having a spectral resolution of 0.1 nm, give information on the luminescence properties of the material. The study of the nature of the radiative recombination can be performed by observing the emission dependence on the experimental conditions. Moreover, the analysis of the luminescence spatial distribution by pan-chromatic and mono-chromatic CL maps allow to correlate spectral and spatial studies. The lateral resolution of the luminescence map is strongly influenced

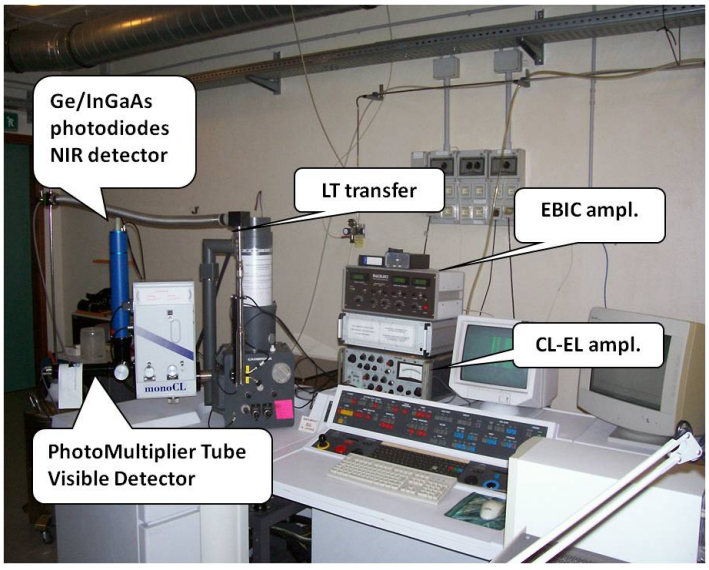

Figure 1.28: CL-SEM set up at the Parma IMEM-CNR laboratories

by the beam/sample interaction volume, which is mainly determined by the electron energy, as well as by the minority carrier diffusion lenght. In the experimental condition used in this work the CL lateral resolution is in the range of hundred of nanometers.

1.4.3 Structural analysis by TEM

Differently from the case of SEM, the sample imaging obtained by a Transmission Electron Microscope (TEM) is created by primary electrons that have crossed the specimen (see Figure 1.26). The interactions with the sam-

ple induce some perturbation on the electron motion, from which we can extract information about the specimen structure. The basic working principle of a TEM can be easily assimilated to that of a conventional optical microscope. As the probe employed in a TEM is an energetic electron beam, very small wavelenghts can be reached, overcoming in this way the resolution limit of classical light microscopes.

Figure 1.29: TEM experimental apparatus at the Parma IMEM-CNR laboratories

The TEM used in this work is a JEOL JED-2200FS and is represented in Figure 1.29. The primary electrons are emitted by a Field-Emission Gun, composed by an extraordinary fine tungsten tip, covered by zirconium. The accellerating working voltage is 200 eV. Electro-magnetic condenser lenses collect the electrons coming from the source and send them to the specimen in a parallel and coherent beam. The sample is mounted on an extractable stage in a perpendicular plane of the optical axes. It can be moved in the x-y-z directions and rotated by $\pm$ 25° e $\pm$19° in two orthogonal directions.

Just beyond the sample, several magnetic lenses (objective, intermediate

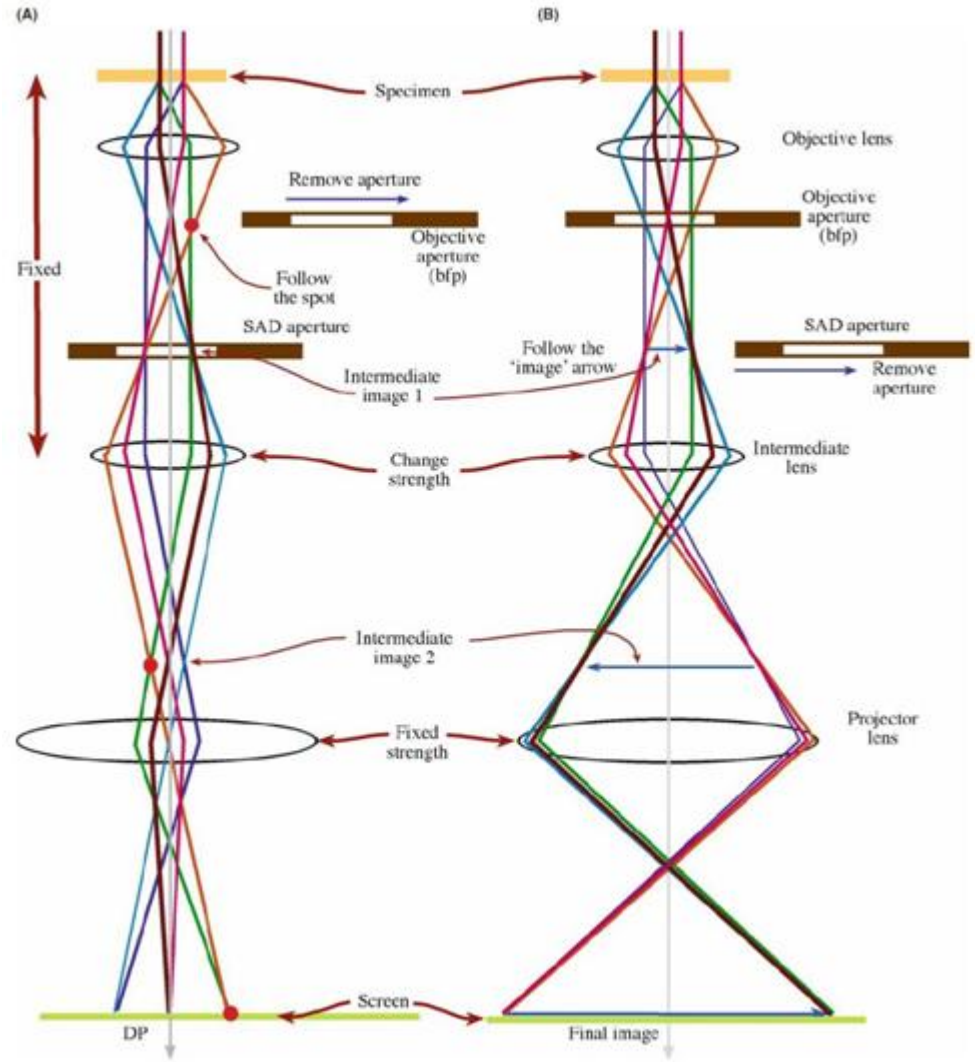

Figure 1.30: Scheme of the main working modes of a TEM: a) diffraction pattern formation and b) sample imaging formation.

and projector) collect the transmitted beam, in order to compose a magnified sample image. The final magnified image can be displayed by means of a CCD camera, placed just at the end of the optical path. An Ω-filter is located between the intermediate and the projector lenses and can be used to get images filtered by energy. The whole column is kept at 10^{-8} Torr by ionic pumps.

Our TEM equipment allows a wide range of analytical methods. In partic-

ular, the sample imaging can be obtained by TEM, High resolution TEM (HRTEM) and in scanning TEM (STEM) mode. The first two methods allows to display the material crystalline lattice, by using the transmitted and the low-angle (Bragg) diffracted electrons. On the other hand, the Mott-Rutherford diffraction used in STEM mode generates high-angle and incoherent diffracted electrons, whose intensity depends on the atomic number Z. This method, called Z-contrast, gives also chemical information about the material. Reciprocal lattice imaging can be obtained in Diffraction Pattern (DP) mode. Moreover, purely chemical information can be extracted by analytical techniques such as the Energy Dispersive X-Ray Spectrometry (EDXS) and Electron Energy-Loss Spectrometry (EELS): the study of the characteristic X-rays or the specific energy loss of primary electrons, resulting from inner-shell ionization, gives information about the atomic structure, that is a fingerprint of a specific element.

A complete description of the complex physical principles and formalism of all TEM working methods is far beyond the aim of this thesis. Here, we will introduce the fundamentals of the techniques employed in our experimental work. The reader is referred to [122] for an exhaustive and comprehensive discussion about the Transmission Electron Microscopy. The TEM studies performed during this work have been focused on the observation of the crystalline (TEM and HRTEM sample imaging mode) and reciprocal lattice (DP mode) of our TiO_2 samples.

In figure 1.30 these main TEM working modes are displayed. The electrons coming from the sample can be represented by geometrical beams. The parallel diffracted beams are found to converge on the back focal plane of the objective lens, where the crystal diffraction pattern is created. Here, a slit with a variable diameter allows to select specific diffraction spots. In the image plane of the objective lens, a first reversed image of the sample is formed. Here, the "selected area diffraction (SAD) aperture" allows the selection of the beams coming from a specific area of the sample. Now, the beams path depends only on the selected working mode: if the intermediate lens is focused on the back focal plan of the objective (mode *a* of Figure 1.30) the DP is magnified and projected on the CCD camera. On the contrary, by focusing the intermediate lens on the image plane of the objective lens (mode *b* of Figure 1.30), the CCD camera displays the magnified sample

image. The magnification can be tuned from 50 up to $1.2*10^6$ times.
The sample imaging can be obtained by operating in amplitude contrast or phase contrast. The amplitude contrast is a consequence of the different electrons diffraction occurring at different regions of the sample. In this mode, the images are magnified maps of the diffraction efficiency over the specimen, with a resolution $>$ 1.5 nm. In particular, they are obtained by

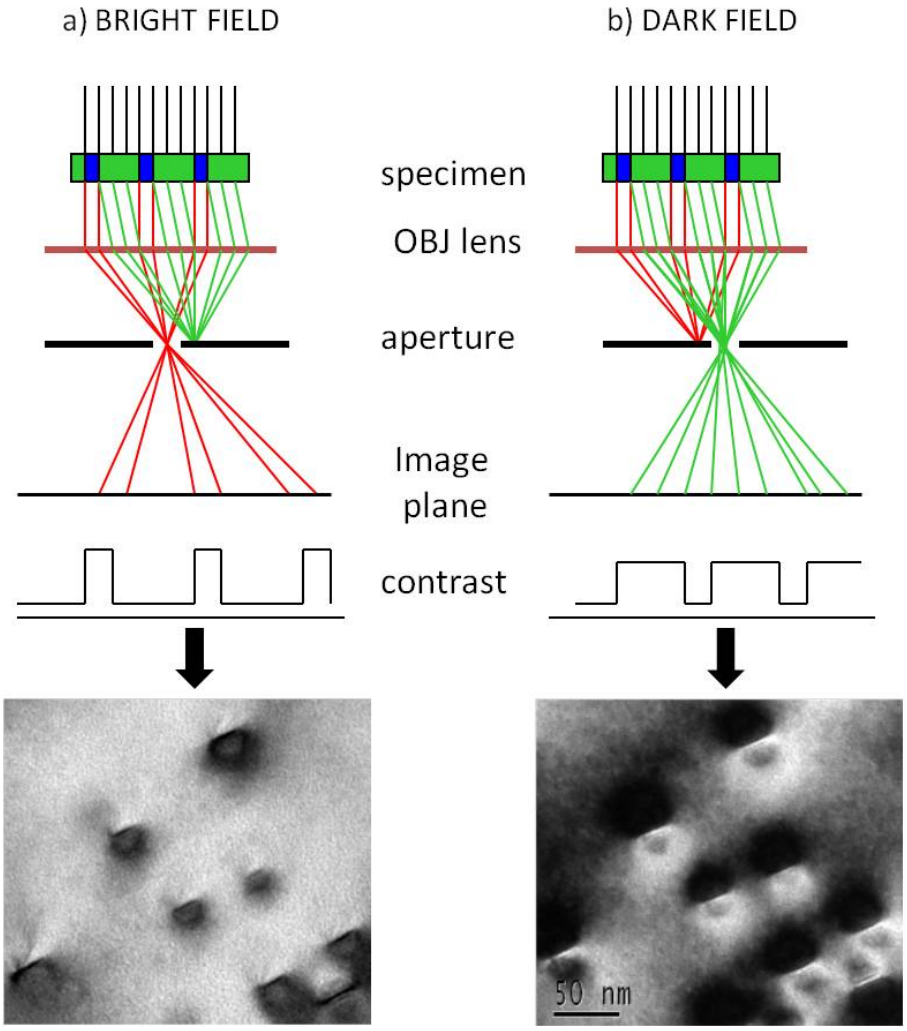

Figure 1.31: Working principles of amplitude-contrast imaging in bright (a) and dark field (b). The related TEM images have been acquired on InAs/GaAs quantum dots.

selecting the transmitted beam (*bright field* image in Figure 1.31) or one of the diffracted beam (*dark field* image), by means of the aperture located in

the focal plane of the objective lens.
On the contrary, the phase-contrast images are obtained by the phase interference of several beams. In fact, a thin specimen introduces phase differences in the scattered electron waves. If the aperture in the back-focal plane of the objective lens allows the recombination of the transmitted beam with the diffracted ones, their interference will produce intensity fringes (Figure 1.32.a). The latters give the representation of the arrangement and the spacing of crystalline planes (Figure 1.32.b), with a resolution up to 0.19 nm. Finally, the diffraction pattern is the bi-dimensional projection of the

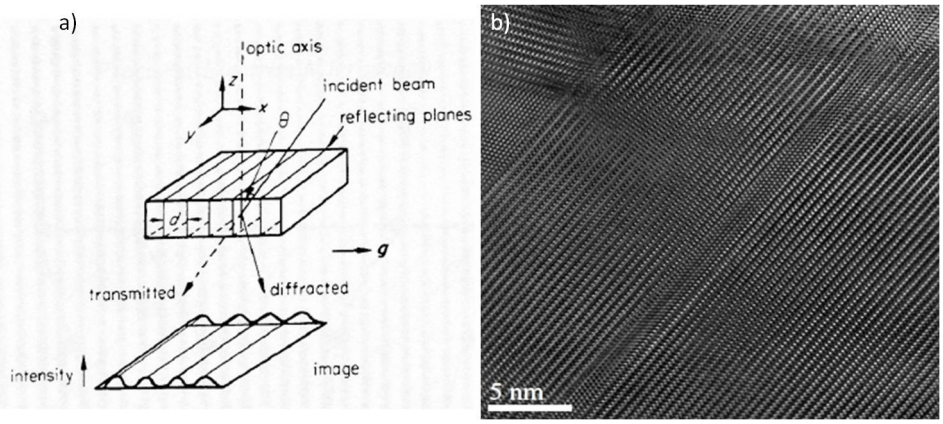

Figure 1.32: a) working principle of the phase-contrast imaging; b) HRTEM image of a ZnO nanorod.

reciprocal lattice points (Figure 1.33.a). Therefore, the analysis of the intensity and symmetry of the diffracted spots gives mainly crystallographic information, such as:

- the crystal orientation respect to the incident electron beam
- the identification of the crystalline plane that have originated the diffraction
- the identification of different crystalline phases.

Note that the diffraction pattern from disorderly-oriented nanocrystals (like our TiO_2 samples) does not show individual spots, but it is characterized by concentric rings (Figure 1.33). In this case, the lattice parameter of the crystalline planes that have originated a specific diffraction ring can be extracted from the inverse of its radius.

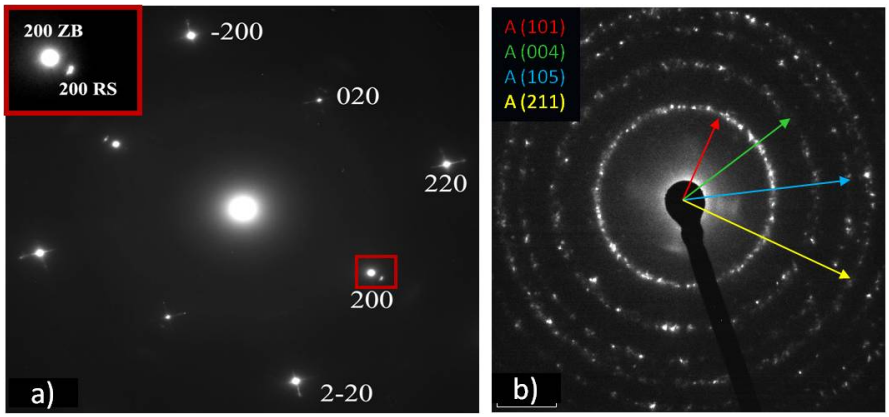

Figure 1.33: a) diffraction pattern from MgS, showing different phases: zincblend(ZB) and rocksalt(RS); b) diffraction pattern from powders (anatase TiO_2 nanocrystals).

1.4.4 Electronic structure by Surface Photoemission spectroscopy

Photoelectron spectroscopies (PES) have been used for the *in-situ* characterization of organic and inorganic thin films and their hybrid interface. PES are considered surface spectroscopies due to the nature of the electron-matter interaction and the regime they are operated. The electrons emitted from a solid undergo several collision processes before exiting the sample surface. In particular, electrons with a kinetic energy in the range of 10-1000 eV undergo diffusion processes in the solid and their mean free path λ is of the order of 0.5-2 nm. Let us consider now the electron escape probability as a function of the creation's depth: from Figure 1.34 it is clear that the 98% of the electrons can escape the surface without losing their KE when the creation's depth is not larger than 4λ. Considering θ as the take-off angle (i.e. the angle between the analyzer and the sample surface) this probability can be written as:

$$P = e^{\frac{-d}{\lambda \sin\theta}} \tag{1.29}$$

Thus the large majority of the electrons leaving the surfaces comes from a maximum depth of 4λ. In Figure 1.35 is represented the "universal curve", that is the electron escape depth as a function of their kinetic energy. As can be observed, the escape depth is in the 5-20 Angstroms range, thus only

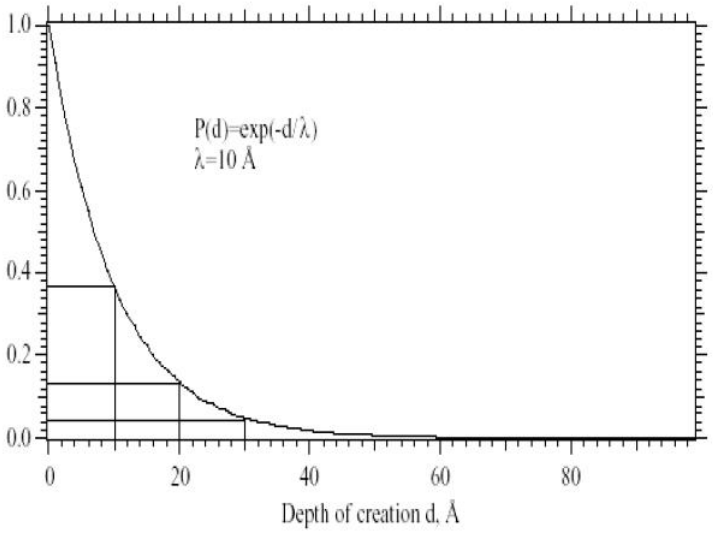

Figure 1.34: Probability of electrons escaping without loss as a function of their creation depth for PES

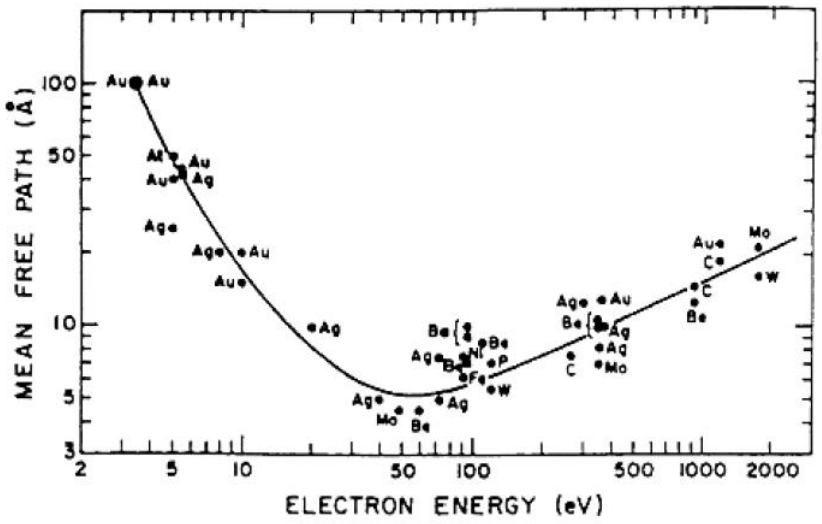

Figure 1.35: Electron escape depth as a function of their kinetic energy for several metals

upper surface contributes to the collected electron signal, as a matter of fact coming from a maximum depth of 80 . UHV conditions are mandatory for PES, and not only for the interaction of escaping electrons with surround-

ing atmosphere. As the sticking coefficient for common residual gases in a vacuum chamber is typically close to 1, at a chamber pressure of 10^{-6} torr it takes only 1 s to the achievement a coverage of 1 Monolayer (ML) on the surface, while at 10^{-9} torr it would takes 1000 s. Therefore, pressures in the 10^{-10} mbar range are necessary to perform a surface spectroscopy experiment in an extended period of time and with reliable results.

X-ray Photoelectron Spectroscopy

The X-ray Photoelectron Spectroscopy (XPS) technique is based on the photoelectric effect: when X-ray photons hit a solid surface, their energy (from few hundreds to thousands of eV) can be absorbed by an electron of a core level, causing its escaping from the surface sample. This process is outlined

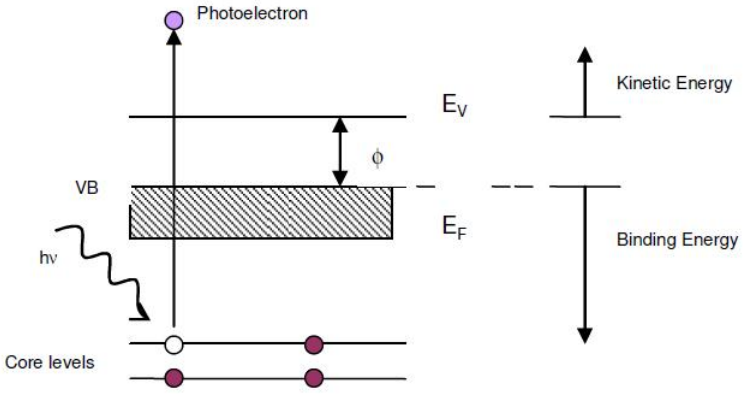

Figure 1.36: Photoemission Process

in Figure 1.36: the electrons generated from a core level leave the surface with a kinetic energy that depends, in a first approximation, from the initial photon energy, the binding energy and the work function of the solid. The fundamental relationship that describes the photoemission process is:

$$KE = h\nu - BE - \Phi \tag{1.30}$$

where KE is the electrons kinetic energy, BE the binding energy of core level from which they were ejected and Φ the work function of the system (considering the sample in electric contact with the analyzer, and at the same ground potential). This relationship is based on the so called one-electron approximation. A more accurate description requires to take into account

further phenomena, as the relaxation processes occurring in the excited parent atom and the energy loss processes experienced by electrons in the solid (electron-phonon coupling and plasmon losses). All these processes lead to a final energy distribution composed of main features, reflecting the core level density of states, and secondary peaks, due to transport processes. As the system can not reach the equilibrium state prior to the photoemission, thus the final state can show two configurations (the so-called "sudden approximation"): in the first one, the electron lies in one atomic excited state, while in the second one the electron is ejected, leaving the atom double ionized. These processes decrease the kinetic energy of the photo-emitted electron and give rise to satellite peaks, such as the so-called shake-up and shake-off features. A detailed description of these processes is beyond the aim of this thesis, and can be found in ref [123]. The photoelectron spectrum is obtained by measuring the kinetic energy of photo-emitted electrons and plotting the intensity (usually expressed as counts per seconds) versus the kinetic energy. It consists of several features: core-hole lines, shake-up and shake-off excitations, Auger peaks, valence band peaks and secondary peak due to minor physical processes. XPS is a powerful technique in surface science since allows the observer to get information about the chemical properties and the elemental composition of the studied surface. Elemental characterization is possible due to the intrinsic uniqueness of each atom electronic configuration, just by evaluating the Binding Energy. Quantitative analysis can be performed measuring the peak area associated to an element, weighted by a sensitivity factor that takes into account the excitation efficiency of each element. For a homogeneous sample with an isotropic elastic diffusion of the photo-emitted electrons, the photocurrent intensity can be expressed as:

$$I_i(KE, i) = I * N_i * \sigma_i(k) * \lambda(KE) * H \tag{1.31}$$

where I is the incident photon flux, N the atomic concentration of the i-species, σ_i the ionization cross section referred to the level i and to the incident photon, λ(KE) the escape depth length at the kinetic energy KE, H an instrumental factor. Since ab-initio calculation of some of the factors in equation 1.31 is quite difficult, the general procedure for this type of analysis is the use of calibrated quantities and the atomic sensitivity factors (ASF), which take into account the excitation probability of the element i, for a certain impinging photon. In such a way the relative atomic concentration

of the element i can be expressed as:

$$N_i = \frac{A_i}{ASF} \tag{1.32}$$

in which the peak intensity is its integrated area Ai. The ASFs, which are also defined for the AES peaks, are tabulated taking as a reference the element i in a standard state [124].

Ultraviolet Photoelectron Spectroscopy

The Ultraviolet Photoelectron Spectroscopy (UPS) is based on the photoelectron effects as well, but it employes UV photons, therefore the involved photon energy ranges from few eV up to few hundreds of eV. The main difference from the XPS spectroscopy hence is that only the most external electronic levels of single atom, molecular bands of atom aggregates (such as HOMO) and high-laying energy bands in the case of solids (like valence band for semiconductors) are involved in the process of photoelectron production. UPS is therefore used to extract important information about interaction processes involving the external electronic levels. For example, let us consider an organic molecule adsorbed on an inorganic surface: UPS enables to extract the HOMO level position with respect to a common reference level (i.e. the Fermi level of the system), which which can give information about the chemical (or not) interaction at the surface. The position of this peak, for instance, can be used to calculate the ionization potential of the species under inspection, leading to useful determination of the band-bending or dipole formation processes for organic/metal interfaces.

Experimental apparatus at Trento IMEM-CNR laboratories

Figure 1.37 shows the surface spectroscopy facility at the Trento IMEM-CNR laboratories. The pumping system, a turbo-molecular pump connected with a dry-pump assures a base pressure of the analysis chamber in the range of 10^{-10} mbar. The analysis chamber is made of μ-metal, in a spherical symmetry so the several sources radially converge to the chamber focus point. The sample stage is located at this point by means of a 5 degrees of freedom manipulator. Moreover, UHV electrical feedthroughs provide electrical contact to bias the sample surface. The analysis chamber is connected by UHV lines with the Fast Entry system and to the Co-deposition chamber by means

of gate valves to assure UHV conditions. This chamber is equipped with

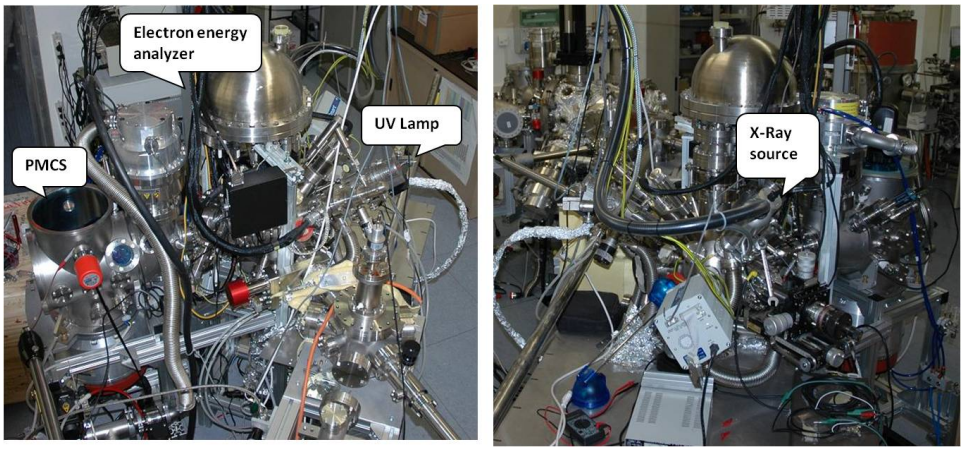

Figure 1.37: Different views of the analysis chamber at the TRENTO IMEM-CNR laboratories

several facilities, but we want to focus our attention on the instrumentation employed during this thesis work. The X-ray source is a Dual Anode X-Ray Source provided by Thermo VG Scientific. Photons are emitted by impact of high energy electrons (up to 15 kV, maximum power of 300 W) on a water cooled twin anode, made of Aluminium or Magnesium. For both materials, the excited emission is the line $K_{\alpha 1,2}$, but the emission energy is different: 1486.6 eV (with a resolution of KE=0.85 eV) and 1253.6eV (KE=0.70 eV) for Al and Mg respectively. The continuum Bremsstrahlung spectrum is filtered by the insertion of a thin (1μm) aluminium foil in correspondence of the exit aperture, which also acts as shield to the high voltage of the anode for the surface of the sample. The UV source is a home-made He discharge lamp, with a two-stages differential pumping employed to minimize gas load in the main chamber. In this work we have used both the He I (hν=21.2eV) and He II (hν=40.8eV) emission lines. The VSW electron analyzer acts as a narrow pass filter, letting pass only the electrons that have a specific kinetic energy. It consist of the lenses system, to focalize and adjust initial electron energy, the analyzer, composed by two hemispherical and concentric lenses, and a 5-Channels Electron Multiplier to collect and reveal the electron. The final resolution is 100 meV. During our experiments also an electron source (LEG62 ThermoVG electron gun) has been used as to perform Scanning

Electron Microscopy (SEM), in order to display the sample surface with a lateral resolution of about 3 μm.

Experimental apparatus at the ELETTRA synchrotron

Part of the surface photoelectron experiments have been performed at the BEAR beamline - ELETTRA (Trieste), in order to take advantage of high photon flux and resolution. The BEAR scheme is illustrated i Figure 1.38 The BEAR beam-line is particularly suitable for our studies as it offers

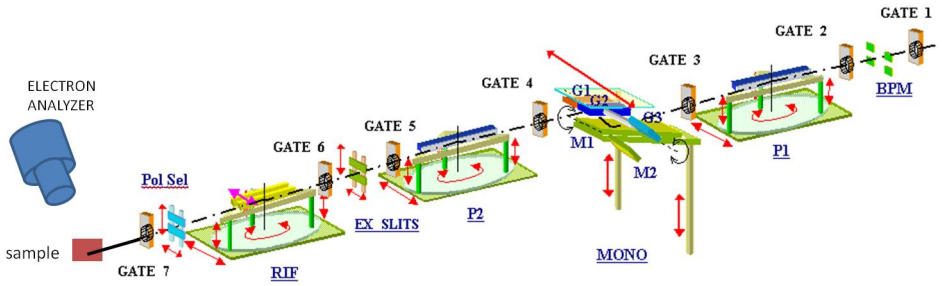

Figure 1.38: BEAR beamline scheme

grants both PES and XAS (not shown here) measurements with the necessary resolution, not disregarding the possibility to proper installing the supersonic beam apparatus on the preparation chamber, an operation not possible on other beam-lines. The BEAR beam-line optics is based on a couple of parabolic mirrors and two in normal and grazing incidence, respectively monochromatizing sections working in parallel light. The design allows to collect emitted radiation from the bending magnet in the 4 mrad horizontal and +/- 1 mrad vertical solid angle. The delivered photons cover the 4-1400 eV energy range: The spot size at the sample is of the order of 300x30 μm x μm (horizontal x vertical). The hemispherical electron energy analyzer has a radius of 66mm, with an energy resolution of 10 meV.

Chapter 2

Titanium dioxide by supersonic beams

The first part of this experimental work is exclusively devoted to the study of TiO_2 thin films, that is the inorganic counterpart of the hybrid interface we will examine hereinafter.
Therefore this chapter is focused on the analysis of the peculiar properties of as-grown TiO_2 thin films, resulting from the non conventionality of PMCS technique. The use of various kinds of diagnostic techniques, described in section 1.4, allows the collection of extensive and wide-ranging information about the structural, chemical, physical, electronic and optical properties of the material. Finally, the effects of annealing treatments on the observed properties have been presented and discussed.

2.1 TiO_2 sample preparation

All the studied TiO_2 specimens have been prepared at the IMEM-CNR laboratory of Trento, by means of the PMCS described in section 1.1.3. As already mentioned, the involved deposition processes are based on the supersonic expansion of cluster-assembled materials and on their subsequent interaction with the substrate. By controlling the beam kinetic energy, it is possible to tune from a soft landing to more energetic impacts, leading to different clusters fragmentation and reactivity phenomena.
The thickness of the studied samples ranges from 100 to 300 nm, as determined by microbalance measurements. Various kind of substrates have been

employed, such as Silicon with native oxide, thermal Silicon oxide, copper, Indium Tin Oxide (ITO), graphite, gold, kept at room temperature. The discharge has been achieved by means of a voltage of 1200 V, with a delay time of 900 μs with respect to the trigger of the pulsed electro-valve. The opening time of the latter has been kept at about 400-500 μs, in order to keep the source chamber and the interface stage at 10^{-5} mbar and 10^{-7} mbar, respectively, with a carrier gas pressure of 20 bar. A critical growth parameter is the composition of the carrier gas mixture, with the presence of specific percentages of O_2 allowing the formation of oxides clusters directly into the plasma source and determining the final stoichiometry. The typical experimental conditions used for the TiO_2 depositions are summarized in the following Table:

carrier gas	opening time (μs)	Voltage (V)	$T_{substrate}$ (K)
He + 1%$_0$ O_2	400-500	1200 V	300

Table 2.1: Typical experimental conditions used for the TiO_2 deposition. By courtesy of IMEM-CNR group of Trento.

2.2 Morphological and structural properties

As a result of the aforementioned growth parameters, all the studied samples are thin film showing a very high porosity. As preliminary investigation, the specimens have been observed by Scanning Electron Microscopy: during the deposition process, the clusters fragmentation at the surface induces the formation of a rough morphology, due to the presence of agglomerates, with size ranging from tenth of nanometers up to a few micrometers. Big-sized clusters are usually arranged at the center of the sample (Figure 2.1.a), while peripheral areas show a lower roughness: that is a direct consequence of the focusing of heavier species at the center of the impinging clusters beam. The use of different substrate does not seem to affect the film morphology. The observed rough character of PMCS TiO_2 (Figure 2.1.b) is particularly interesting for photovoltaic applications. In fact a porous surface guarantees the high surface to volume ratio needed for a good sensitization efficiency;

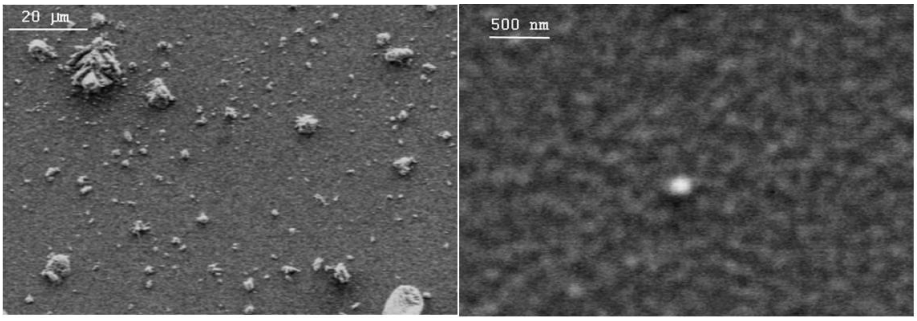

Figure 2.1: SEM images of a typical TiO_2 sample grown by PMCS: (a) the central area of the specimen, characterized by the presence of big-sized clusters and (b) its rough surface, observed at higher magnification.

besides it constitutes a strong limitation to light refractivity.
Extensive Micro Raman studies have been assigned to the Physics Department of Trento University, in order to get structural information of the as-grown samples. To obtain the phase composition from single agglomerate and to avoid the average effects due to the contribution of several submicrometric structures, the attention has been focussed on agglomerates of the same size of the probe (2 μm).
All the investigated agglomerates show a mixed-phase character, as it results from the relative intensity variation of Anatase and Rutile vibrational modes reported in Figure 2.2. Particularly interesting is the presence of the Rutile phase, as it commonly requires high annealing temperatures (850-1000 °C) to be activated [125].
The data collected by this technique were particulary helpful for our studies as it gave us preliminary information about the crystalline nature of the samples, despite their small thickness. Moreover Micro Raman has been used to investigate selected regions of the sample so allowing a better correlation with the luminescence information provided by our following Cathodoluminescence studies (see section 2.4). It has to be mentioned that XRD measurements, performed on other films with higher thickness, showed the same mixed-phase structure [25].
In this thesis work, the information provided by these long-range techniques is integrated by structural studies at the nanoscale. To this end, in order to get samples suitable for HRTEM studies, the titania films have been

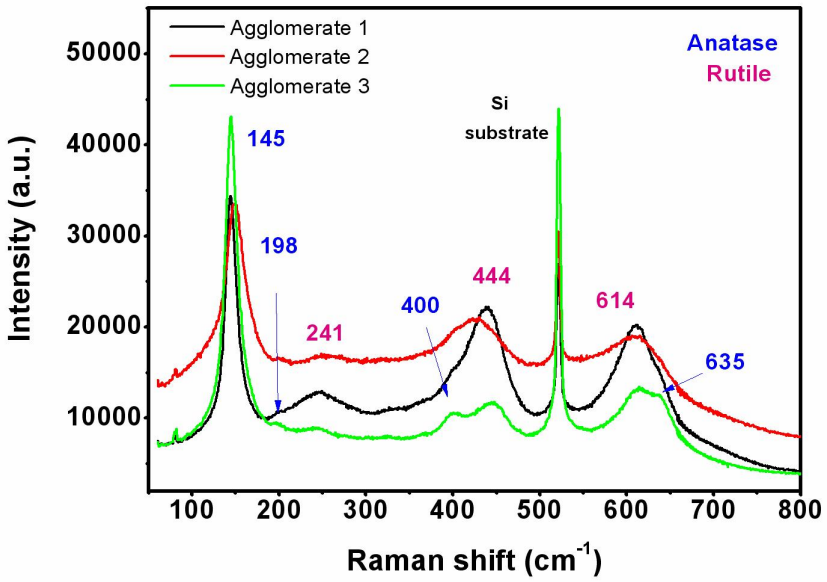

Figure 2.2: Micro Raman spectra of as-grown TiO_2 thin films, acquired from different agglomerates visible on the sample surface. The vibrational modes of both Anatase and Rutile phases are shown, revealing the strong mixed-phase nature of the specimen (by courtesy of Physics Department of Trento University).

scratched out from their substrates and deposited on copper meshes. Taking advantage from the different facilities of our system (see section 1.4.3), a detailed analysis on the structure of the agglomerates has been performed. In particular HRTEM images show that the agglomerates are mainly composed of nanocrystals, embedded in a thin amorphous matrix. The nanoparticles (NPs) shape is quite irregular, while their size range in the interval 5 - 30 nm (Figure 2.3 (a) and (b)).

Crystallographic studies have been performed on various agglomerates, by observing their Diffraction Pattern (DP) or by calculating the Fast Fourier Transform (FFT) from their HRTEM images. In Figure 2.4 the DPs from two different clusters are represented and compared. Figure 2.4.a shows the typical diffraction pattern from powder of the same phase (here Rutile),

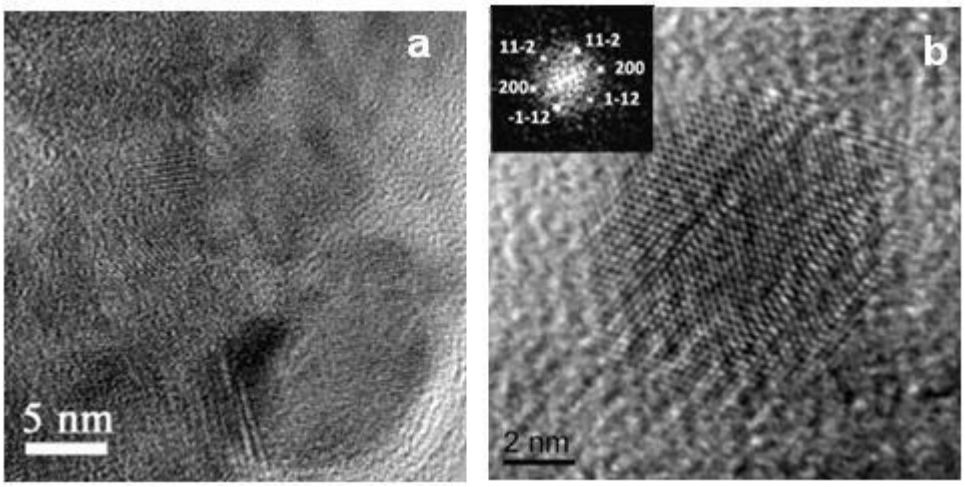

Figure 2.3: (a) High resolution TEM image acquired on RT-grown TiO_2 sample, showing the presence of crystalline nanoparticles and a certain size spreading (b) Wiener filtered HRTEM image of a small and isolated particle crystallized in the anatase phase, 021 projection, as demonstrated by the diffractogram in the inset.

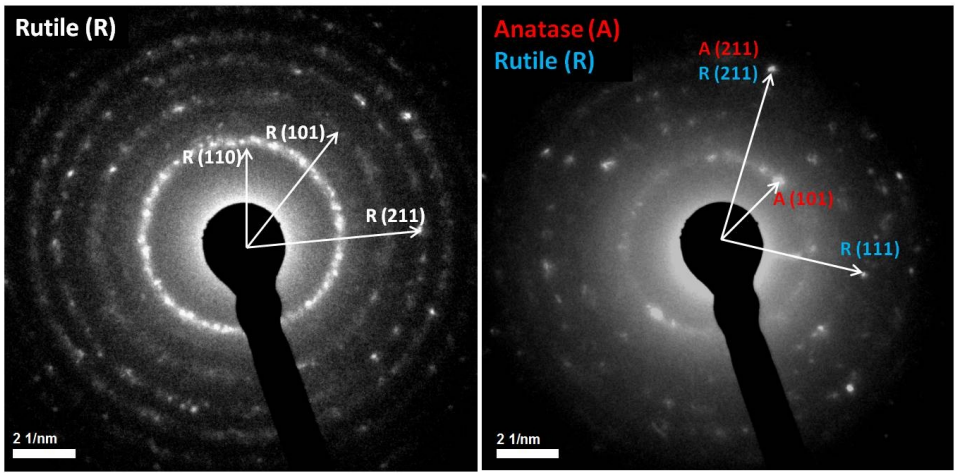

Figure 2.4: Crystallographic studies on two different clusters: (a) well-defined DP that can be ascribed to diffraction from a single phase (Rutile); (b) DP showing the contributions from different phases.

characterized by the presence of well-defined concentric rings. Actually this is a quite rare case, as the DPs obtained in our samples usually show a mix

of not well-defined rings and single spots, like those represented in Figure 2.4.b. In this case, the calculated lattice distances can be related sometimes to Anatase, sometimes to Rutile or even to both phases. The inset of Figure 2.3.b represents a crystallographic study on an isolated anatase particle performed by means of FFT.
These studies are a confirmation of the crystalline and mixed-phased nature of our samples, but they give above all the first direct evidence of the small dimensionality of the crystals and a measurement of their average size.

2.3 Electronic properties

The electronic properties of as-grown TiO_2 samples have been studied by means of photoelectron emission experiments performed in the IMEM-CNR laboratories in Trento (see section 1.4.4). The experimental results, here presented, have been obtained from *in situ* studies, i.e. the TiO_2 samples have been directly deposited in the analysis chamber and then characterized in UHV environment without exposure to atmosphere. This procedure prevents and minimizes the surface contamination.

Core levels

The typical experimental core levels spectra of as-grown TiO_2 samples are represented in Figure 2.5. In particular, the left picture (A) reports the photoelectron emission from Ti_{2p} core level, showing the spin-orbit doublet, separated by 5.7 eV: the sharper $Ti_{2p^{3/2}}$ peak is found at 459.34 eV, while the $Ti_{2p^{1/2}}$, having a broader FWHM, has a BE of 465.29 eV. The right picture (B) of figure 2.5 represents the O_{1s} spectrum: it shows a main peak at 530.62 eV and a smaller one at 532.51 eV. These two peaks are representative of the oxygen bonded to titanium (blue peak) and to other chemical species, i.e. water and air contaminants (green line). The latter is about the 5% of the main peak area and it is probably be related to residual contaminants lying on the surrounding substrate, thus not from the film surface. All the observed binding energies (see Table 2.2) are in agreement with the values reported in literature [124], confirming that the chemical species of titanium and oxygen atoms present in our films is properly TiO_2. The atomic percentages of have been evaluated from the core levels analysis, by using the

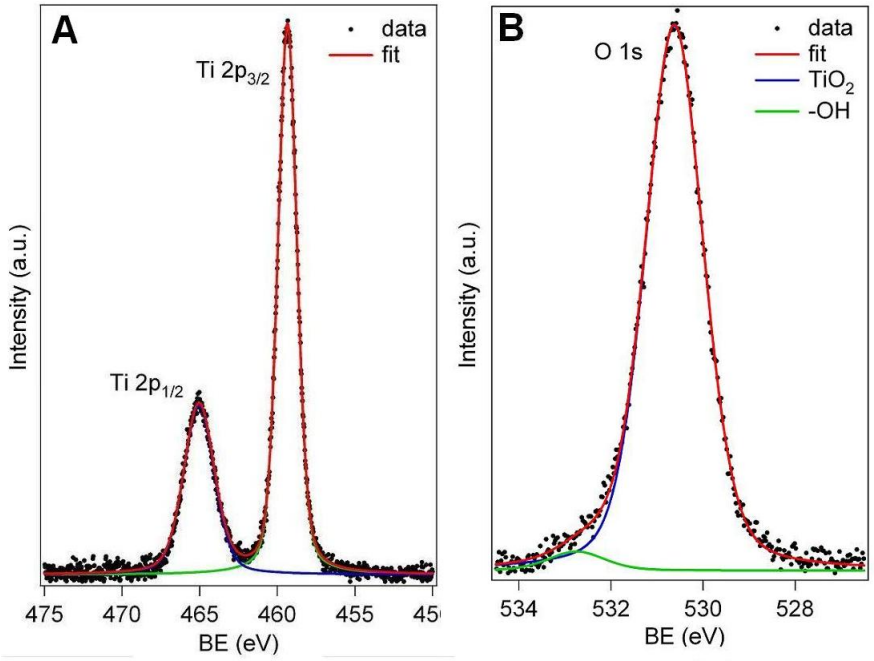

Figure 2.5: Core levels spectra from TiO_2 thin films: (A) Ti_{2p}, (B) O_{1s}

sensitivity factors method [126] with the Yeh and Lindau photoionization cross sections [127]. The statistical O/Ti ratio calculated over a wide number of as-grown samples ranges between 2.20 and 2.30, suggesting that the NPs are superstoichiometric in nature. This is in contrast with the typical results obtained for TiO_2 grown by other techniques, where the tendency is to synthesize under-stoichiometric materials, showing oxygen vacancies due to the high temperature thermal treatments. It has to be noticed that the stoichiometry calculation has been achieved by disregarding the peak related to oxygen contaminants and -OH groups, and by taking into account only the main peak at 530.62 eV. Moreover, the XPS signal, in the experimental conditions used for this analysis, samples a surface depth of about 5 nm. In our case, we are dealing with the typical dimensions of the titania NPs, thus the observed oxygen concentration can not be due to a segregation in the topmost layers but is representative of a NPs volume property.

Core Level	component	BE (eV)	FWHM (eV)
Ti_{2p}	3/2	459.34	1.45
	1/2	465.29	2.35
O_{1s}	TiO_2	530.62	1.48
	-OH groups	532.51	1.45

Table 2.2: Experimental Ti_{2p} and O_{1s} Core Levels Components of PMCS TiO_2 thin films, shown in Figures 2.5

Valence band

Figure 2.6 represents the typical UPS spectrum acquired from PMCS TiO_2 thin films. It is referenced to the Fermi level E_F, determined from an UPS spectrum of a sputtered gold surface. The spectrum shows two distinct re-

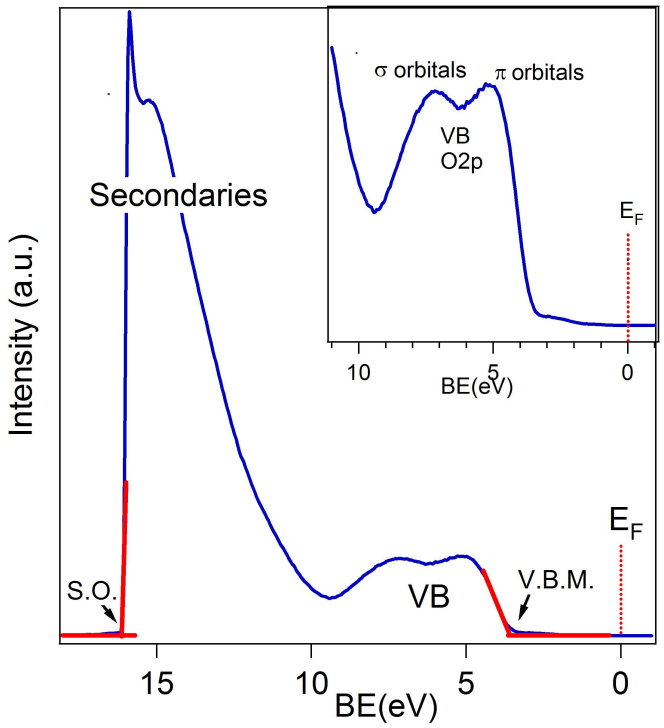

Figure 2.6: UPS spectrum from TiO_2 thin films. INSET: an extended view of valence band region.

gions: the first one at higher BEs is related to the secondary electrons, while

the second one at lower binding energies corresponds to the valence band. The value of the valence band maximum has been determined by fitting a straight line into the leading edge: it is found at around 3.51 eV below the Fermi level (E_F) [76]. The secondary electron onset (SO) on the left side of the spectra is located at 16.0 eV. Then, the work function of our TiO_2, calculated by subtracting the SO value from the excitation energy (21.2 eV), is found to be 5.2 eV.
The inset of Figure 2.6 represents an extended view of the valence band region. Titanium dioxide is known for its ionic character [64], so the valence band consists mainly of O 2p states (partially hybridized with Ti 3d states). The O 2p contribution to the UPS spectrum displays a double-peak structure: the first emission peak at around 5 eV, is attributed to the photoionization of the upper part of the VB, i.e. the non-bonding π orbitals, while the second one at around 7 eV is related to photoemission from σ (bonding) O2p orbitals [128]. A small component can be observed at about 2-3 eV, near the valence band edge (see the onset of Figure 2.6). It is ascribable to the presence of surface defects states probably related to the material morphology, such as grain boundaries and clusters aggregation. Several works [75] [76] [128] report the presence of a weak structure between the VBM and the E_F (at a BE around 0.8-0.9 eV), attributed to the photoionization from the lower oxidation state of $Ti^{3+}3d$, related to surface defects of oxygen.

2.4 Luminescence

The luminescence properties of non-conventional superstoichiometric as-grown samples has been investigated by SEM-CL.
Taking advantages of the possibility to correlate spectroscopic and morphologic information, we have focused our attention on specific agglomerates on the surface and we have collected their spectroscopic response. As shown in Figure 2.7 (continuous lines), two distinct emissions are found at room temperature, centered at 3.16 or 3.25 eV, depending on the investigated agglomerate. The peaks show high intensity, small FWHM and are localized in the spectral region of the material band gap, suggesting typical Near Band Edge (NBE) emissions.

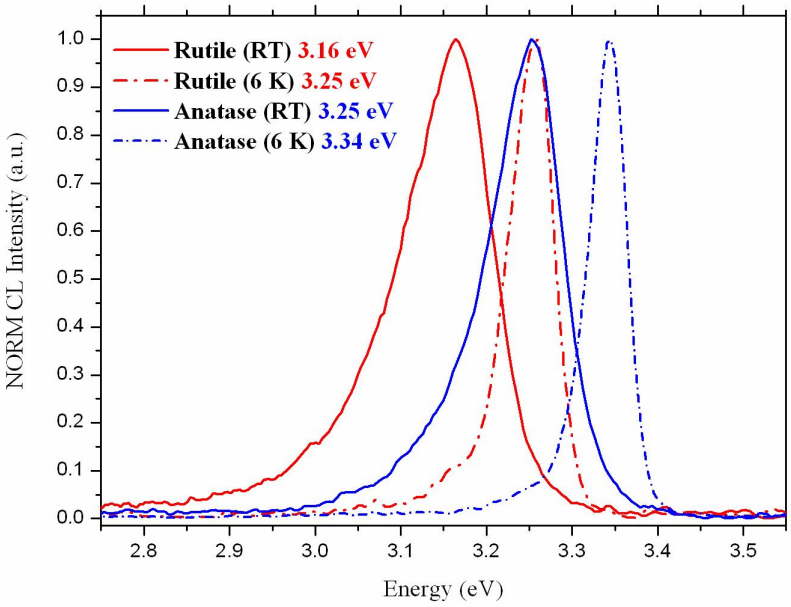

Figure 2.7: Comparison between the RT and 77K SEM-CL spectra acquired from the same two agglomerates. A rigid energy shift of about 90 meV is found for both the Anatase and Rutile phases.

In order to determine the nature of the involved transitions, we performed CL investigation by changing the experimental conditions. As expected for the NBE emissions, no energy dependence from excitation density has been found in both cases and the observed relation between CL intensity (I_{CL}) and the beam current is (I_B) $I_{CL} = {I_B}^{\alpha}; 1 < \alpha < 2$.
Finally, temperature dependent CL investigations have been performed from 6 K (LT) to 300 K (RT). At LT, both peak positions show a rigid red shift of 90 meV (Figure 2.7- dashed lines); this phenomenon is reproducible for all the studied nanostructures. The emission energy dependence on temperature, represented in the inset of Figure 2.7, is found to follow the Varshni equation [129], demonstrating the excitonic nature of the transitions.
Considering the mixed-phased nature of the specimens, the presence of two distinct UV emissions, centered at 3.16 eV and 3.25, can be explained as exciton recombinations from Rutile [96] and Anatase [130] phases respectively.

The peak energy positions as well as the energy difference (about 90 meV) between the CL peaks are in good agreement with literature photoluminescence [98] and absorption studies performed on nanostructured TiO_2 (n-TiO_2) [96] [130]. It is important to note that the optical band gap values reported for n-TiO_2 are usually larger than those for bulk Titania, (about 3.2 eV for Anatase and 3.05 for Rutile [73]). This phenomenon is ascribed to an increasing of the oscillator strength of the first allowed direct transition with the decreasing of crystal size [131].
CL imaging is then used to visualize the emissions from Rutile and Anatase phases on our specimens. An emblematic example is shown in Figure 2.8, where the accurate study about the spatial distribution of the excitonic emissions from two agglomerates is reported (A and B in Figure 2.8.a). The monochromatic SEM-CL images (monoCL), acquired at the RT excitonic emission energy of both Rutile (3.16 eV) and Anatase (3.25 eV), are shown in Figure 2.8 (b) and (c) respectively. The first observation is that the two

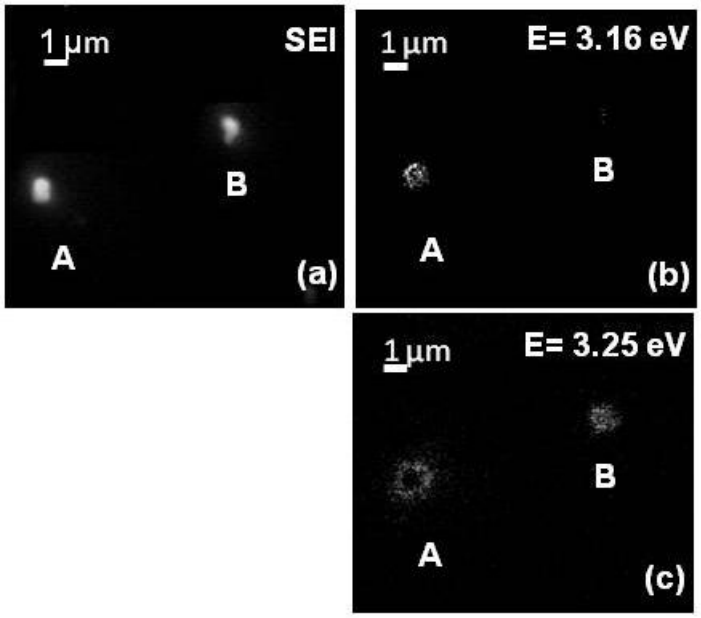

Figure 2.8: . (a) SEM image of two typical TiO_2 agglomerates of submicrometric size; (b) and (c) mono-CL images of the agglomerates in (a) acquired at E=3.16 eV (Rutile phase) and E=3.25 eV (Anatase phase) respectively. The onset/disappearance and the spatial distribution of the two mixed phases are shown.

agglomerates show their maximum of luminescence at different energies, that is an indication of higher fraction of Rutile in Agglomerate A than in B. Further, by comparing Figure 2.8.b and 2.8.c an anticorrelation between Rutile and Anatase spatial emission is imaged on the agglomerate A, while agglomerate B does not seem to show any spatial distribution of its emission.
In Figure 2.9 we report a deconvolution of the emission peak from agglomerate B, showing the presence of different contributions: the deconvolution curves marked 1-4 could be ascribed to the recombination of free and bound excitons from the Anatase phase and their phonon replicas, while the fifth contribution could be related to the exciton recombination from the Rutile phase. The lower intensity of the emission at 3.25 eV is ascribed to a lower amount of Rutile in the investigated agglomerate.
It is also worth to notice that the main component in Figure 2.9 is 20 meV blue shifted with respect to the afore-mentioned value of Anatase exciton emission at 77 K. The observed shift can be possibly ascribed to Anatase NPs with different diameter compared to those responsible for the transition at 3.34 eV. In fact a dependence of the optical band-gap on the NPs size has been already demonstrated in the literature by absorption [132] as well as by photoluminescence measurements [98]. In particular Luo et al. found a PL peak energy blue shift of 200 meV for a 45 nm size increase of self assembled Anatase nano-dots grown at 500 °C [131]. Quantum confinement effects on the excitonic energy emission values have been excluded, because observable only for NPs of size smaller than 3 nm [90] [89].
Further extensive CL investigations on different NPs agglomerates have been performed showing a maximum energy deviation dE of 30 meV from the 2 main values of the excitonic emissions. By plotting and fitting the data reported in ref [131], it is possible to extract the emission energy dependence on the nanodots size variation; according to this empirical relation, the NPs size variation expected for our energy shift of 30 meV is about 5 nm, that is consistent to the afore-mentioned NPs size spreading, obtained by HRTEM. However, it must also be considered that the CL recombination volume diameter at the analyzing conditions has been calculated (by MonteCarlo simulations [133]) to be about 500 nm, so the observed energy shift could also be affected by a different amount of Anatase and Rutile phases in the investigated volume.

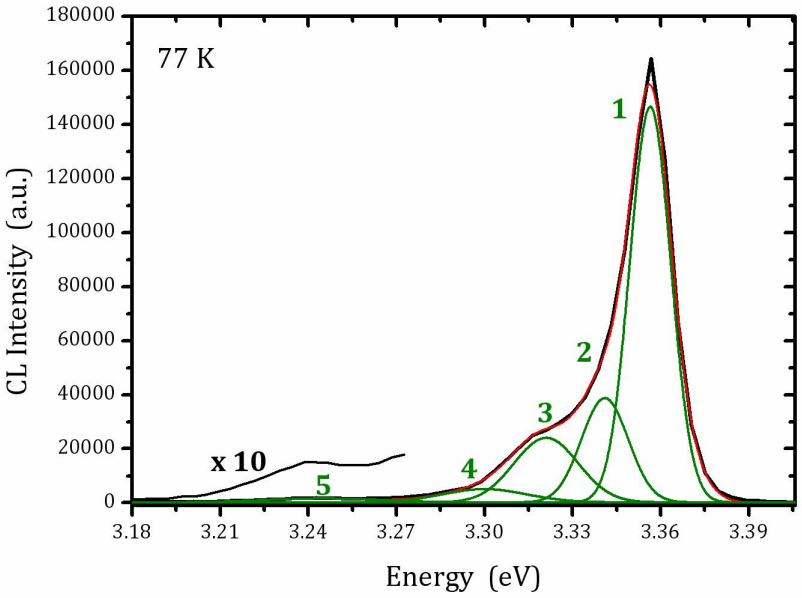

Figure 2.9: A deconvolution of the UV peak from agglomerate A in fig. 4, showing a clear coexistence of excitonic emission from both phases; in particular component 1-4 are ascribed to free (3,357 eV) and bound (3,340 eV) exciton from the Anatase phase and their phonon replicas (3.301 eV and 3.245 eV), while the fifth contribution can be related to the exciton recombination from the Rutile phase.

2.5 Effect of annealing on the n-TiO_2 properties

In order to test the peculiarity offered by PMCS in room temperature synthesis of nanocrystalline TiO_2, we carried out controlled thermal treatments, typically required from other synthesis processes for crystalline activation [134].

After in vacuum annealing at 450 °C, the excitonic emissions observed in superstoichiometric samples completely disappear while a broad band arises, centered around 2.5 eV (Figure 2.10) and typically correlated to the presence of V_O, arises [91] [93].

The observed metastability of the optical properties does not correlate with any pronounced structural modification as shown by HRTEM studies that

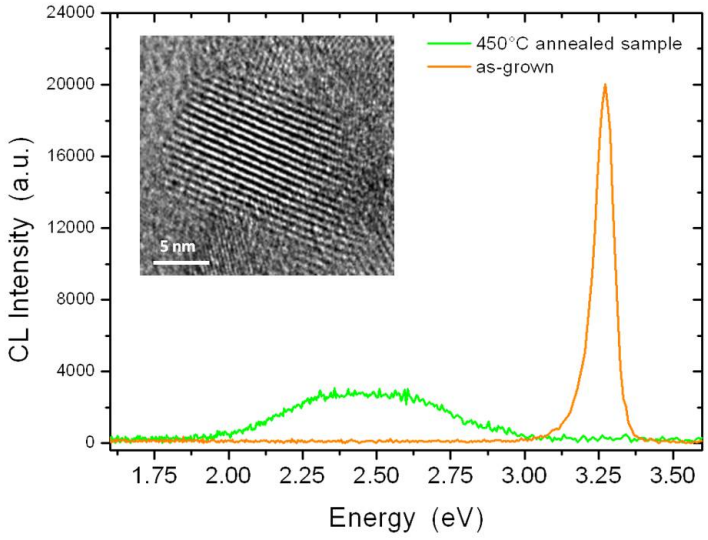

Figure 2.10: Comparison between room temperature SEM-CL spectra on as-grown and T=450 °C annealed n-TiO_2 thin films. The onset of a broad band centered around 2.5 eV due to Vo in the annealed sample is apparent. INSET: HRTEM image of a nanocrystal 10 nm in size belonging to an annealed sample. No significant difference is found with respect to the as-grown n-TiO_2 thin films (see Figure 2.3.b).

revealed the NPs remained single crystals in nature (see inset Fig. 2.10). As typically thermal treatments induce a desorption of oxygen atoms [135], the vanishing of the excitonic peaks in the superstoichiometric annealed samples may be simply ascribed to the formation of V_O. To assess this hypothesis, further XPS studies were carried out on annealed samples. Figure 2.11.a and 2.11.b shows the O_{1s} spectra achieved in ex-situ experiments, the fit parameters and the calculated stoichiometries of the same sample, before and after the annealing. The Core Level spectra of O_{1s} show two components in both cases, with the peak at higher Binding Energy (BE) being related to TiO_2 (blue area), while the other one is assigned to residual -OH species (green area) due to air contamination. The variation in the spectrum shape, as a consequence of the annealing, is mostly ascribed to the strong reduction of the -OH components, i.e. to water desorption. The O_{1s} component

related to TiO_2 shows a small but significant area reduction, leading to a corresponding decrease of the O/Ti ratio from 2.30 to 2.20 due to the annealing treatment. The presence of a visible emission despite this residual superstoichiometry, could be explained by a sort of "compensation" induced by the annealing. The oxygen in excess in the as-grown samples probably leads to the formation of intra-gap p-levels [136] that are not optically active, so the material and shows its excitonic emission. The subsequent annealing and formation of V_O can induce the formation of the n-levels below the conduction band. In this way, the oxygen loss generates the superstoichiometry reduction, the quenching of UV emission and the contemporary rising of the visible band. Our findings confirm that the n-TiO_2 thin films grown by

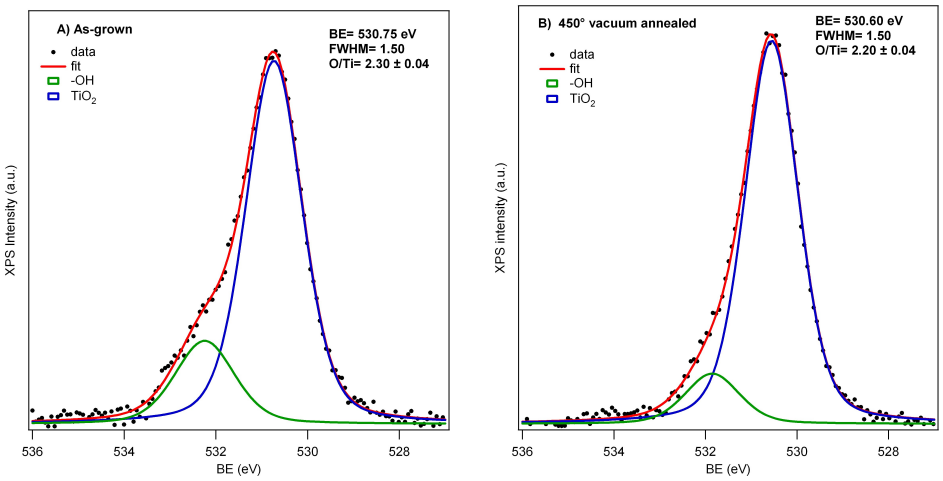

Figure 2.11: O_{1s} spectra of the same sample before (a) and after (b) the annealing are compared. Two different contributions has been observed: the oxygen related to titanium dioxide (blue) and the residual -OH species (green).

PMCS, have properties at the state of the art that are very promising for device applications [117]. That result is achieved despite the crystallization is not supported by thermal treatments but it is carried out just through purely kinetic processes.

2.6 Conclusions

The first experimental evidence of room temperature excitonic emissions from n-TiO_2 grown by a supersonic cluster beam at 300 K is given. XPS studies shows the n-TiO_2 are superstoichiometric in composition, with an O/Ti ratio ranging from 2.20 up to 2.30. HRTEM investigations reveal the crystalline character of the specimens, confirmed also by the Micro Raman analyses with presence of both Rutile and Anatase phases. These results are achieved because of the unique properties of the PMCS approach, with the formation of crystalline NPs at room temperature and the possibility to control the stoichiometry of the compound. CL spectroscopy shows two sharp excitonic peaks at 3.16 and 3.25 eV, ascribed to the coexistence of Rutile and Anatase respectively. An average energy spread of $\pm$ 30 meV is found and is correlated to emissions from NPs with different sizes in a 5-30 nm range, as also supported by HRTEM studies. The influence of stoichiometry on the optical and structural properties of the n-TiO_2 is assessed by studying the thin films before and after annealing experiments. In vacuum thermal treatments at 450 °C resulted in a complete vanishing of the excitonic transitions of both Rutile and Anatase phases. XPS and HRTEM studies performed on annealed n-TiO_2 thin films show a decreasing of the O/Ti ratio, without any significant change in the crystalline structure. As a conclusion, we achieved the evidence of correlation between the excitonic emissions and the excess of oxygen in our NPs. This unprecedented ability of PMCS of fine-tuning the optical properties of oxide nanostructures pave the way to very interesting studies and applications, like sensing and energy [117] [25], as they are well known to play a critical role in the device efficiency. For instance, recent studies demonstrate the influence of the optical properties on the photocatalytic activity of nanoparticulates for chemical waste [137] as well as on the response efficiency of gas-sensor devices [138].

Chapter 3

Phthalocyanines films by supersonic beams

Upon introducing the properties of our TiO_2, we can focus our attention on the organic counterpart of the hybrid interface (described in the next chapter). Here, we present a detailed study of the electronic properties of both copper and free-base phthalocyanine, grown by means of supersonic beams seeded by organic precursors. The study has been achieved by comparing core levels and valence bands (VB) of both molecules, obtained by high resolution photoelectron emission experiments performed at synchrotron ELETTRA. The aim of this work is to help the interpretation of the chemical/physical processes involving these molecules in UHV hybrid systems synthesis and to better understand the real influence of the metal core (if any) during the sensitization processes.

3.1 Experimentals

The experiments have been performed at the BEAR beamline (BL8.1L), installed at the left exit of the 8.1 bending magnet of the ELETTRA synchrotron facility in Trieste (Italy). All the depositions have been achieved and characterized in situ (i.e. in UHV environment without exposure to atmosphere), in order to prevent and minimize the samples contamination. The depositions of phthalocyanines thin films have been achieved by using a supersonic molecular beam apparatus, directly connected to the beamline preparation chamber. The apparatus geometry has been carried out in order

to get the molecular beam impinging orthogonally to the substrate surface. The employed substrates are amorphous gold films, about 500 nm-thick, deposited ex situ by a traditional Knudsen cell on silicon native oxide supports. The latter have been previously cleaned by chemical treatment in an ultrasonic bath, in order to remove impurities and pollutants. The absence of contaminants at the gold surface have been checked before the deposition of organic films by core levels photoemission spectroscopies. CuPc and H_2Pc powders with a certified purity of 99.99 % have been acquired from Sigma Aldrich. A specific degassing procedure has been performed before each deposition session in order to purify both the powders, by removing the possible traces of the solvents used during the powder synthesis, and to obtain contaminants-free supersonic beams. All the examined samples have been grown with a deposition rate of 1 Å/min, estimated by means of a quartz-crystal microbalance. The pressure of the preparation chamber was $4 \cdot 10^{-7}$ mbar during the organic film deposition, while the base pressure was $4 \cdot 10^{-10}$ mbar. The difference of three order of magnitude for the chamber pressure is due to the presence of the carrier gas, helium in this case, in the supersonic molecular beam. More details about the growth apparatus are reported in the section 1.1.3. The final thickness of CuPc and H_2Pc film is 25 nm, that is large enough to exclude any contribution from the gold substrate in the photoelectron spectra, and small enough to prevent charging effects in our films. Clean gold substrates and all the organic films have been thoroughly characterized by X-ray photoelectron spectroscopy and ultraviolet photoelectron spectroscopy; the organic samples have been carefully checked for radiation damage during beam exposure. XPS and UPS measurements were performed by using a hemispherical electron energy analyzer, with an energy resolution of 10 meV. The photoelectron spectroscopy measurements have been collected in normal emission geometry. The Valence band analysis was performed using photons at 90 eV, characterized by a bandwidth of about 30 meV. The photons energies used for the C_{1s}, N_{1s} and Cu_{2p} core levels were 400, 513 and 1068 eV, respectively, in order to keep constant the photoelectron energy at 110 eV and, consequently, the sampling depth and surface sensitivity for all elements. The aforementioned photons were characterized by a bandwidth of 0.5, 0.7 and 2 eV, respectively. The spectra intensity have been normalized to the incident photon flux, monitored

by a gold grid. In all the PES experiments the photon incidence angle was 80° refereed to the normal of substrate and the photon beam was linearly polarized. The core level analysis was performed by Voigt line-shape deconvolution after background subtraction by a Shirley function. The typical precision for each component energy position is ± 0.05 eV. The uncertainty for FWHM (full width at half maximum) is less than ± 5%, while for the area evaluation is about ± 2.5%. The reader is referred to section 1.4.4 for more details about the diagnostic technique and the experimental apparatus.

3.2 XPS core levels

The atomic models of the studied molecules are represented in Figure 3.1. Despite the bond delocalization of these macrocycles, different chemical species can be identified. As shown in the left picture of Figure 3.1, the

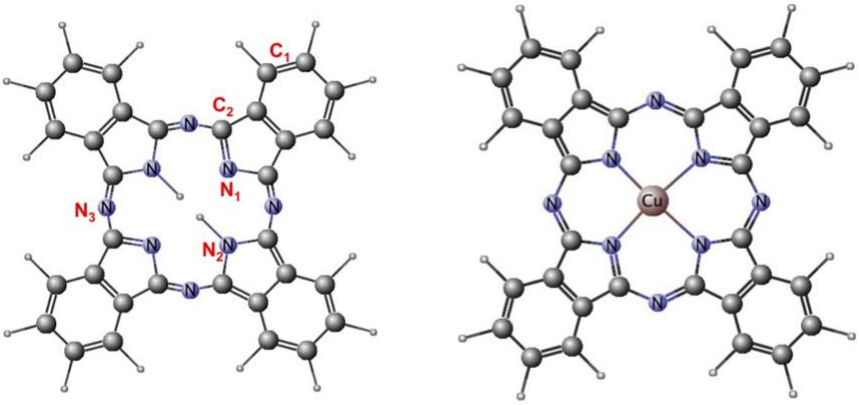

Figure 3.1: Model of free base H_2Pc (left) and metal phthalocyanine CuPc (right)

carbon atoms of free-base phthalocyanine ($C_{32}H_{18}N_8$) can be divided into twenty-four aromatic carbons (C_1) of the phenyl rings, and eight pyrrolic carbon atoms (C_2). The nitrogens can be distinguished into four pyrrolic nitrogens, divided in turn into two N_1 atoms (with a lone pair in the molecular plane) and two N_2 atoms (bonded to the two central H atoms), and four meso-bridge aza-nitrogens (N_3). The copper phthalocyanine ($C_{32}H_{16}CuN_8$) is represented in the right picture of Figure 3.1. Here, the 4-fold coordinated core, generated by the removal of the internal hydrogens, is occupied by a

copper atom. For the sake of simplicity, we will use for both molecules the same atoms labeling, just introduced; however, it should be noticed that the pyrrolic nitrogens are chemically equivalent in CuPc, so in the last case the contributions of N_1 and N_2 atoms will be discussed simultaneously.
The atomic percentages have been evaluated from the core levels analysis, by using the sensitivity factors method [126] with the Yeh and Lindau photoionization cross sections [127]. Disregarding the hydrogen contributions, the calculated stoichiometry of our molecules are found to be in good agreement with the theoretical values. For H_2Pc, the atomic percentages are estimated to be 78.8% and 21.2% for C and N respectively, very similar to the expected 80.0% and 20.0%. On the other hand, the estimated content of

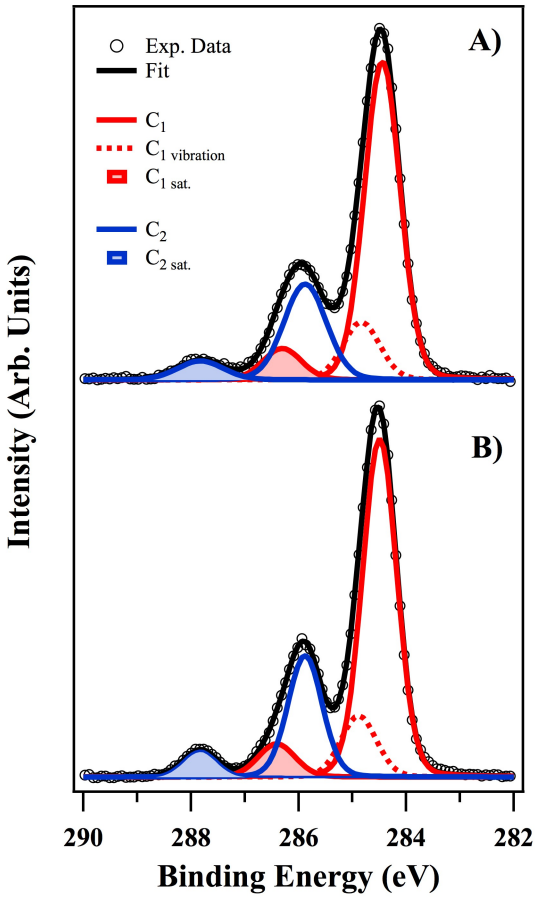

Figure 3.2: C1s Core Level spectra from thick films of H_2Pc (A) and CuPc (B)

carbon, nitrogen and copper atoms in our CuPc films were 78.2 %, 19.7% and 2.1% respectively, nearly coinciding with the theoretical percentages (78.0%, 19.5% and 2.4%).

Figure 3.2 represents the experimental spectra of C 1s core level collected from H_2Pc (A) and CuPc (B) thick films. Both molecules show the same lineshape, as expected due to the similar chemical environment of the carbon atoms in copper and free base phthalocyanines: both spectra are dominated by three pronounced structures with a very slight asymmetric broadening on the high binding energy side, suggesting the presence of more components. Taking advantages of this similarity, the interpretation of the the C_{1s} core levels deconvolution will be presented just for H_2Pc. The case of CuPc will be introduced soon after, by pointing out all the remarkable differences between the two molecules. From the Voigt analysis of C_{1s} core levels five different peaks arise: in H_2Pc, the main contribution is centered at 284.36 eV (red continuous line), while the second most intense feature is located at 285.79 eV (blue continuous line). Further peaks can be found at 284.75 eV (red dashed line), 286.22 eV (red-filled area) and 287.73 eV (blue filled area), respectively. The percentages of the aforementioned peaks on the total C_{1s} area are (in the order they have been presented) 57.8%, 20.7%, 10.9%, 6.1% and 4.4%. All fit parameters are reported in Table 3.1. The most intense contribution is attributed to the electrons photoemission from the 24 aromatic carbon atoms of the phenyl rings and it is then labeled as C_1 (Figure 3.2). The second most intense peak is ascribable to the 8 pyrrole carbons (C_2 in Figure 3.2). According to the number of the atoms involved, the ratio between C_1 and C_2 areas should be 3.0. This is not the case, as also the other contributions have to be taken into account. In particular, the filled-area peaks at 286.22 and 287.73 eV have been previously attributed to shake-up processes from C_1 and C_2 respectively and are then indicated as C_{1sat} and C_{2sat} [139]. The energy gap between the main ionization peak and its shake-up feature is 1.86 eV for benzene carbon atoms and 1.94 eV for pyrrole carbons, similar to the energy of the Frenkel molecular exciton of Pcs, estimated to be 1.85 eV by Papageorgiou et al. [139]. It has to be noticed that the ratio between the benzene shake-up and its main peak is definitely lower than C_{2sat}/C_2, as shown by the theoretical work of Brena et al. [140]. The peak reported as C_{1vib} is assigned to vibrational coupling

between the initial and the final state during the photoemission from C_1 atoms. It is located at 0.39 eV from the main feature, in perfect agreement with values reported in [141] and [139]. By taking into account all these contributions, the stoichiometry ratio of the aromatic, i.e C_1, C_{1vib} and C_{1sat} (red components), and pyrrolic carbons, i.e. C_2 and C_{2sat} (blue peaks), is 3.0 as expected.

The deconvolution of CuPc C_{1s} core level shows the same features, whose fit parameters are reported in Table 1. In particular, the main contribution C_1 is located at 284.49 eV; C_{1vib} and C_{1sat} are centered at 284.88 and 286.39, respectively. Concerning the contributions from pyrrole carbons, the C_2 is centered at 285.87 and it shape-up peak C_{2sat} at 287.83. The percentages of C_1, C_{1vib}, C_{1sat}, C_2 and C_{2sat} peaks on the total C_{1s} area are 57.8%, 10.9%, 6.1%, 20.8% and 4.5%, respectively. Also in this case, the ratio between the aromatic and pyrrolic carbons is 3.0, as expected. The comparison of the fit parameters of both H_2Pc and CuPc (see Table 3.1) highlights the great similarity of their carbon structure: in particular, the relative intensities and energy differences of all contributions are found to be almost the same in both molecules (considering the experimental uncertainty). However, some differences can be observed in the FWHM values: in fact, the C_2 and C_{2sat} contributions in H_2Pc have a broader character with respect to those of CuPc, with a FWHM increasing by 20%. This phenomenon can be ascribed to the slight difference in the chemical environment of the pyrrole carbons of the two molecules: in CuPc, the pyrrole nitrogens, N_1 and N_2, are chemically equivalent, so C_2 and C_{2sat} show the same sharp character of the benzene carbons contributions. On the contrary, in H_2Pc the C_2 carbon atoms are bonded with two different type of nitrogens, N_1 and N_2, causing a broadening of their related components in C_{1s} core levels.

Figure 3.3 presents the experimental spectra of N 1s core level acquired from H_2Pc (A) and CuPc (B) thick films. Differently from the previous case, the N_{1s} line shapes of the the two molecules are rather different, therefore their deconvolutions will be discussed separately.

The H_2Pc N_{1s} core levels spectrum consists of two intense features at about 398.9 and 400.4 eV, and further weaker structures at higher BE. The main feature at 398.9 eV is related to the two pyrrole nitrogens N_1 with a lone pair in the molecular plane (red continuous line) and to the four meso-bridging

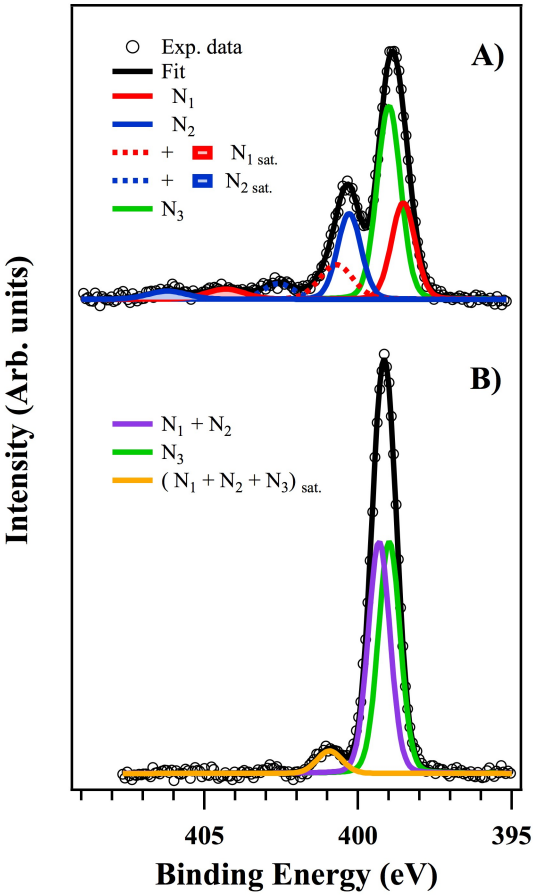

Figure 3.3: N_{1s} Core Level spectra from thick films of H_2Pc (A) and CuPc (B)

aza-nitrogens N_3 (green line). They are located at 398.53 eV and 399.00 eV, respectively. Their energy difference of 0.47 eV is in agreement with the theoretical values reported in [142] and [143]. The second structure at 400.4 eV is associated with the two pyrrole nitrogens bonded to the central hydrogens (i.e the blue continuous line, indicated as N_2) and a first shake-up satellite (red dashed line), probably related to both N_1 and N_3 contributions. The N_2 peak is centered at 400.29, while the $(N_1 + N_3)_{sat}$ has a BE of 400.71 eV. The shake-up satellite of N_2 is located at 402.59 eV and is indicated as N_{2sat} in Figure 3.3 (blue dashed line). Two further components are visible at high BE region (red and blue solid areas): both of them are located at an energy difference of 3.61 eV from both the aforementioned satellite contributions,

therefore they can be considered as further satellite peaks and labelled as $(N_1 + N_3)_{sat2}$ and N_{2sat2}. The percentages of the aforementioned peaks on the total N_{1s} area are all reported in Table 3.1. Here, the evaluation of the nitrogens stoichiometry is more difficult, as the shake-up contributions of the N_1 and N_3 atoms are too close in energy to be distinguished, resulting in a single broad peak. However it has to be noticed that, as expected, all the contribution related to pyrrolic aza-nitrogens bonded with hydrogen atoms, i.e. N_2, N_{2sat} and N_{2sat2}, constitute the 25% of the whole N_{1s} area, and that the N_3 peak area is almost doubled respect to N_1 and N_2 area.

The CuPc N_{1s} deconvolution (Figure 3.3.B) shows the presence of three

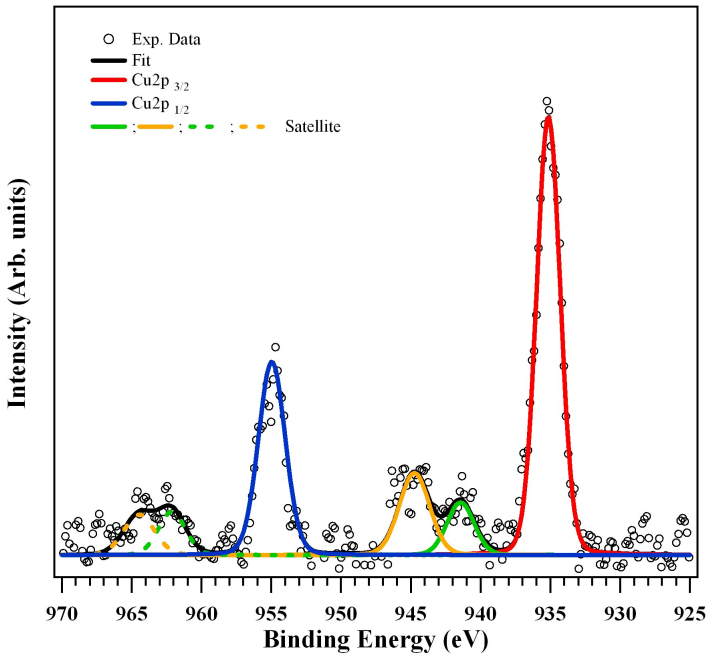

Figure 3.4: Cu_{2p} Core Level spectrum from thick films of CuPc

peaks: the green line at 399.00 eV is referred to the four meso-bridging aza-nitrogens, while the peak at 399.30 eV, showing same sharpness and area of the previous one, is related to the four pyrrole nitrogen atoms N_1 and N_2 (here, chemically equivalent). The energy difference of 0.33 eV is in agreement with the values reported by Ottaviano et al. for CuFPc [144]. The third peak can be attributed to shake-up transitions, probably involving all kind of nitrogens. By comparing the N_{1s} fit parameters of both molecules

(Table 3.1), it is possible to observe that the presence of a copper atoms in the molecular core implies some changes on the relative energies and on the FWHM of the different components. In particular the several components of CuPc N_{1s} core levels show lower FWHM than those of H_2Pc.
The Cu_{2p} core levels spectrum of CuPc is displayed in Figure 3.4. It shows a spin-orbit doublet of 20 eV, each component being composed by a main peak and a multiple satellite structure. The $2p_{3/2}$ component is located at 935.00 eV, while the $2p_{1/2}$ component is found at 955.00 eV. The area of the latter is half of the $2p_{3/2}$ peak, as expected (see Table 3.1). Several shake-up satellites can be found at 941.30, 944.60 eV, 962.12 and 964.46 eV and are ascribable to the hole formation in the Cu 2p orbital and to the different degeneracy of the final state.

		H_2Pc				CuPc			
Core Level	Component	BE (eV)	△E (eV)	FWHM	%	BE (eV)	△E (eV)	FWHM	%
C_{1s}	C_1	284.36	-	0.78	57.8	284.49	-	0.75	57.8
	C_{1vib}	284.75	+0.39	0.81	10.9	284.88	+0.39	0.78	10.9
	C_{1sat}	286.22	+1.86	0.84	6.1	286.39	+1.90	0.80	6.1
	C_2	285.79	+1.43	0.93	20.7	285.87	+1.38	0.75	20.8
	C_{2sat}	287.73	+3.37	1.00	4.4	287.83	+3.34	0.75	4.5
N_{1s}	N_1	398.53	-0.47	0.91	20.4	399.3*	+0.33	0.83	47.3
	N_2	400.29	+1.29	0.91	18.1				
	N_3	399.00	-	0.91	40.7	399.00	-	0.83	47.3
	$(N_1+N_3)_{sat}$	400.71	+1.71	1.26	10.2	400.93*	+1.93	0.96	5.4
	N_{2sat}	402.59	+3.59	1.16	4.2				
	$(N_1+N_3)_{sat2}$	404.32	+5.32	1.50	3.5				
	N_{2sat2}	406.20	+7.20	1.50	2.9				
Cu_{2p}	3/2					935.00	-	2.00	47.3
	1/2					955.00	+20	2.27	23.7

Table 3.1: Experimental C_{1s} and N_{1s} Core Levels Components of both H_2Pc and CuPc, shown in Figures 3.2, 3.3 and 3.4. For each component we report name, energy position, energy difference with the main peak, FWHM, and percentages on the total core levels area. *Due to the chemical equivalence of the CuPc pyrrolic nitrogens, the N_1 and N_2 components are overlapped, as well their shake-up satellites.

3.2.1 UPS valence band

The valence band photoelectron spectra collected from H_2Pc and CuPc thick films are represented in Figure 3.5. The binding axes origin is referred to the Fermi level E_F. The main peaks, common to both molecules, have been labeled with letters from A to G.

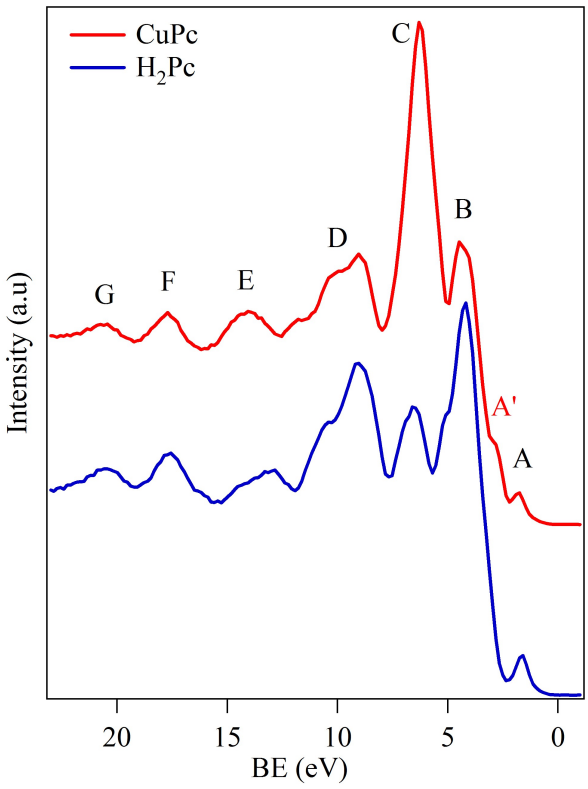

Figure 3.5: UPS valence band spectra from H_2Pc and CuPc thick films (photon energy = 90 eV).

Considering the H_2Pc spectrum, the highest occupied states (HOMO) can be found at around 1 eV (peak A); this feature is known to be a π orbital mainly composed by carbon 2p orbitals [142]. All the other features originate from a mixture of carbon and nitrogen orbitals, whose specific contribution can be only determined by theoretical calculations. In particular, the Density of states (DOS) simulations by Alfreddson et al. [142] suggest that the structures from B to D have mostly carbon and nitrogen 2p origin, while E arises from C_{2s} components. On the contrary, features F and G are mainly attributed to carbon and nitrogen 2s orbitals.
The CuPc valence band spectrum shows almost the same structures of H_2Pc (from A to G), but some differences can be observed in their shapes and reciprocal weights rising from the contribution of copper orbitals to the occupied states. In particular, peak C shows a strong intensity increase, that is as-

cribed by Evangelista et al. to the contribution of Cu-derived orbitals [141]. Moreover, the formation of a new feature, labeled *A'*, is observed at 2.8 eV and it is related to a contribution from copper 3d state [145], The presence of the core-metal atom does not contribute to the HOMO level, as demonstrated by the theoretical work of Marom et al. [146]
A more detailed description of the atomic contributions to the highest occupied orbitals can be only achieved by specific computational data. In this respect, we are performing theoretical analysis on the electronic structure of both CuPc and H_2Pc by Density-functional theory (DFT) calculations, in collaboration with a research group from the Berlin University.

3.3 Conclusions

The electronic structures of both copper and free-base phthalocyanine have been determined by core levels and valence band investigations. The high resolution of the XPS measurements, performed by synchrotron radiation, allows the determination of well suitable fit models for all core levels. In particular, the deconvolution model related to the CuPc molecule will be the needed basis for the study of sensitization processes at the inorganic/organic interface, discussed in the next chapter. The comparative study of the UPS spectra gives the role played by the metal core in the molecule valence band.

Chapter 4

Sensitizing by supersonic beams

The peculiar features of both TiO_2 and CuPc, rising from the supersonic beams approaches, have been investigated and discussed in the last two chapters. Following the achievement of a comprehensive knowledge of the electronic properties of both the organic and the inorganic counterparts, we focus our attention to the chemical reactivity phenomena occurring at their interface, induced by the same deposition method. In the next section, we will introduce a first sensitization experiment (referred as A), where a functional hybrid material has been obtained by depositing copper phthalocyanine on TiO_2, by means of SuMBD and PMCS supersonic beam methods, respectively. In order to understand the role of kinetic energy during the sensitization process, a further hybrid material, with the same configuration, has been achieved by using an organic seeded beam working in the effusive regime (experiment B). Both hybrid systems have been investigated by comparing their *in-situ* photoelectron spectroscopy spectra, acquired at different coverages of the organic film. These experiments have been performed at the IMEM-CNR laboratories in Trento. A Detailed description of the experimental apparatus and can be found in section 1.4.4.

4.1 Experiment A: CuPc/TiO_2 at high molecular kinetic energy

In the first part of the experiment, a layer of titanium dioxide, about 60 nm-thick, has been synthesized at room temperature by PMCS, directly in the analysis chamber. The deposition parameters are the same reported in Table 2.1. The substrate consisted in an amorphous gold film, about 500 nm-thick, deposited ex situ by a traditional Knudsen cell on silicon native oxide support. In order to remove impurities and pollutants, the substrate has been previously cleaned by traditional chemical treatment in an ultrasonic bath and, once placed in the analysis chamber, sputtered by Argon beam.
In the second part of the experiment, the PMCS apparatus has been replaced by a SuMBD source: this solution allows the deposition of the CuPc molecule directly on the TiO_2 film, reaching a complete overlap of their spots and then improving the reliability of the data interpretation. The carrier gas used in this experiment was helium. It is initially injected in the source at 900 mbar, but it reaches about 1200 mbar when the source is working at full capability. With these parameters a supersonic beam is produced, the seeded molecules of which show very high kinetic energy (more then 20 eV). The temperatures of the beam source have been modulated in order to keep the deposition rate at about 1 Å/min during all the experiment stages.
The molecule deposition has been performed in several steps, at 5 increasing coverage (<=1ML, 2ML..) up to the achievement of a thick bulk organic film. Core levels and UPS spectra have been acquired at each coverage step, from the clean TiO_2 to the bulk CuPc, in order to evaluate the electronic properties and the chemical/physical processes during the formation of the hybrid interface.
Figure 4.1 shows the XPS wide energy range spectra (called survey) collected at each step of the experiment. The bottom spectrum is related to the clean TiO_2 surface, while the top one has been acquired on the bulk CuPc film. All the other spectra are related to the 5 intermediate organic coverages. Hereafter, each deposition has been indicated with the label $CuPc^x_A$, where "A" stands for the experiment name and the number "x" suggests the % of CuPc amount extracted from the C_{1s} quantitative spectra (see next section).

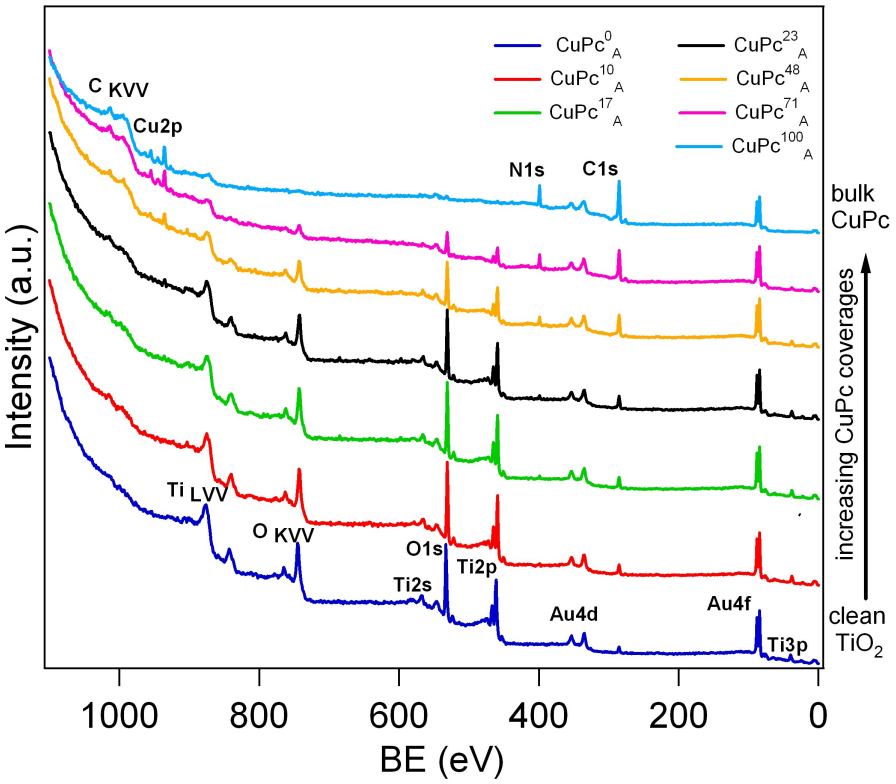

Figure 4.1: Survey spectra acquired at each deposition stage of experiment A, from the clean TiO_2 to the bulk CuPc.

The surveys have been acquired by keeping the electron analyzer pass energy at 50 eV: the high signal intensity granted by this experimental condition allows a fast data acquisition over the whole BEs range (to the detriment of resolution). This is particularly helpful to get an immediate overview about the chemical elements present in the analyzed surface.

The blue line spectrum shows the typical features of titanium dioxide: the principal core levels of titanium, i.e Ti_{2s}, Ti_{2p} and Ti_{3p}, can be clearly identified at about 560, 460 and 30 eV, respectively, while the electron photoemission from the 1s orbital of oxygen is located at about 530 eV. As the analyzed area is wider than the spot of the deposited material (about 1 cm^2 versus 0.5 cm^2) the survey shows also a strong contribution of the 4d and 4f orbitals related to the gold substrate (at about 340 and 80 eV, respectively). At higher binding energies, some Auger structures are observed: the lines in

the region between 800 and 900 eV are LVV auger transitions occurring at titanium atoms. Further Auger lines are located in the region ranging from 750 to 800 eV and are KVV transitions related to oxygen atoms.
By observing the intensity of all the afore-mentioned structures in the other spectra, it can be noticed that the features related to TiO_2 gradually reduce their intensity, up to reach a complete quenching in the top spectrum (sky-blue line). This is obviously a consequence of the gradual coverage of the titanium dioxide film due to CuPc deposition. At the same time, the gradual rising of the organic molecule structures is observed, up to the achievement of their maximum intensity at the top spectrum: the photoemission from 1s orbitals of nitrogen and carbon can be identified at about 400 and 290 eV, respectively, while the multi-peaked structure at about 950-930 eV is related to the 2p orbitals of copper. Finally, the features at 990 eV are ascribed to KVV Auger transition occurring in carbon atoms. It has to be mentioned that a small contribution of C_{1s} orbitals is distinguishable even in the clean TiO_2 film (blue line). This is a consequence of the presence of some adventitious carbon atoms lying on the gold substrate and not on the TiO_2 clean substrate, evaluated to be carbon free by Auger analysis. This contribution has been evaluated and subtracted from all the C_{1s} spectra collected at the different coverages and here presented. In the following sections we will examine the reference core level of each element of interests (i.e. Ti_{2p}, O_{1s}, C_{1s}, N_{1s}, Cu_{2p}), by analyzing both quantitative and high resolution spectra.

4.1.1 Quantitative XPS

As the survey gives only preliminary information about the presence/absence of the different chemical elements, further XPS measurements have been collected for each CuPC coverage, in order to extract quantitative information. The employed pass energy for this kind of analysis is 20 eV, as it grants a good compromise between resolution and signal intensity, as well an higher reliability over the whole BEs range of the electron analyzer transmission.
The core levels spectra collected at the different CuPc coverages are all displayed in Figure 4.2: pictures (a) and (b) show the gradual quenching of the Ti_{2p} and O_{1s} signals; while the increasing of the C_{1s}, N_{1s} and Cu_{2p} intensities are represented in pictures (c), (d) and (e), respectively.
For each core level, we have extracted the spectra areas and we have nor-

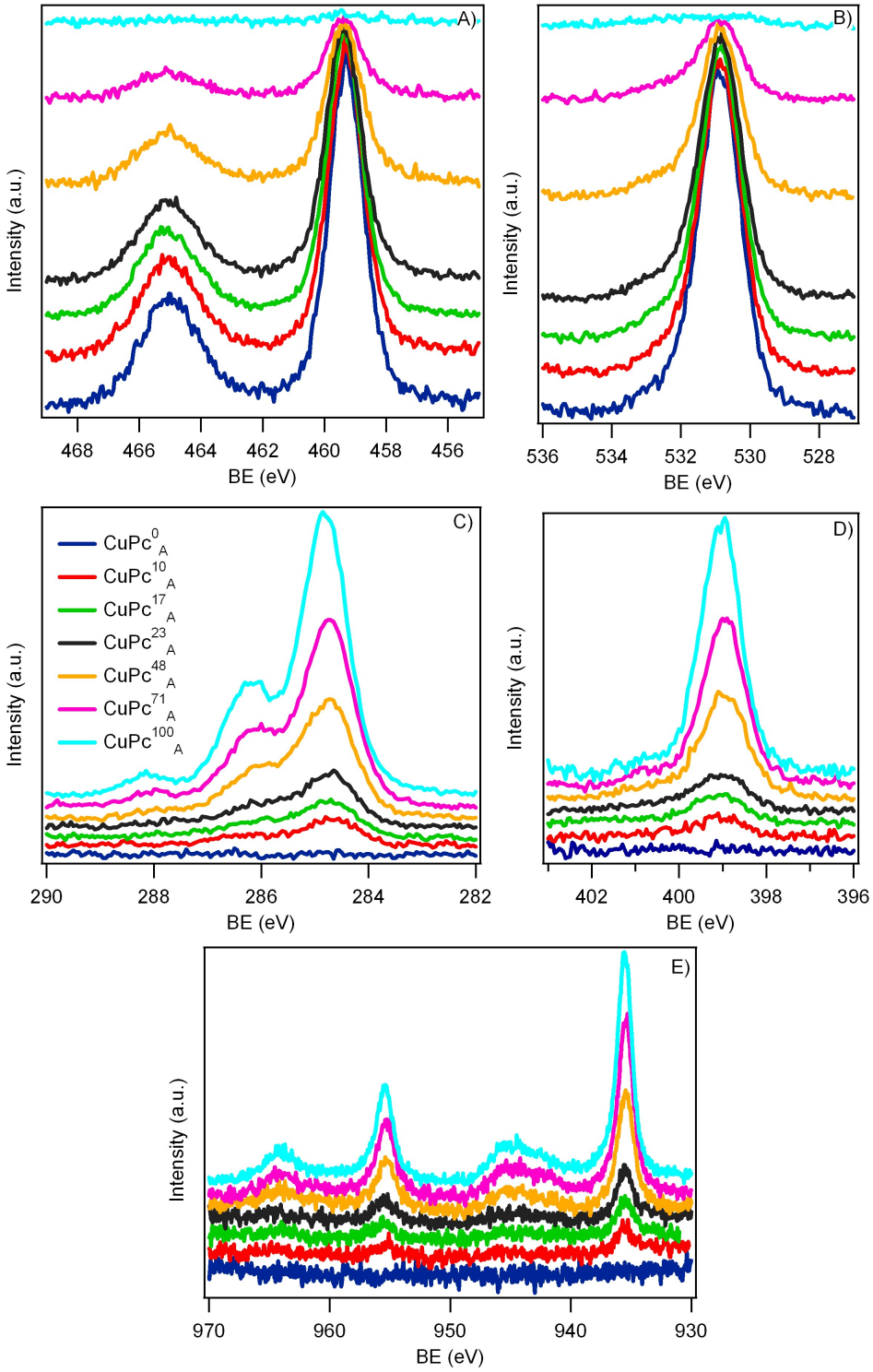

Figure 4.2: Quantitative core levels spectra, collected at different CuPc coverages (exp. A): (a) Ti_{2p}; (b) O_{1s}; (c) C_{1s}; (d) N_{1s}; (e) Cu_{2p}.

malized them to the maximum area. In figure 4.3 these normalized areas are plotted versus the deposition time t of the CuPc molecule (bottom x scale), in order to display the reciprocal trend of the different signals during the several steps of the experiment. The top x-scale represents the estimated

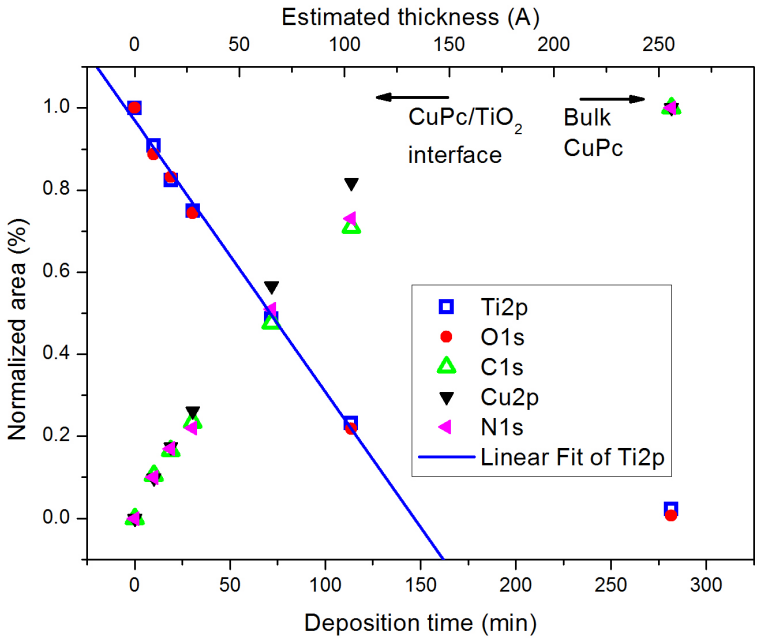

Figure 4.3: Normalized areas of the quantitative XPS data (exp. A) plotted versus the deposition time (bottom x-scale) and the estimated CuPc thickness (top x-scale)

thickness of the CuPc film, calculated as the deposition time multiplied by the measured deposition rate. At t=0 min (i.e. before the start of CuPc deposition), the Ti_{2p} e O_{1s} core levels show their maximum intensities. As the time goes by, their percentages assume lower and lower values, with a reciprocal agreement of the 1%.

By first approximation, the complete coverage of the titanium dioxide film can be extracted by a linear fit of the first 6 points of the Ti_{2p} areas (or O_{1s} as well): according to this extrapolation, the possible effects occurring at the CuPc/TiO_2 interface could be observed up to a deposition time of about 160 min (i.e. about 145 A-thick CuPc layer). As shown in Figure 4.3, the last coverage step has been achieved far beyond this threshold, later on 120

minutes. Therefore, the data collected in the last deposition are not affected by any interface effects and can be considered as reference data for CuPc bulk molecule.

In Figure 4.4, the trends of Ti_{2p} (a) and C_{1s} (b) signals have been reported and analyzed, in order to understand which kind of deposition model explains better our data behavior (see paragraph 1.3.2). It is known that an electron signal crossing a material with thickness d, is attenuated by inelastic scattering of a factor $e^{-\frac{x}{\lambda}}$ being λ the inelastic mean free path. The Ti_{2p} signal attenuation can be tentatively fitted by the equation:

$$\frac{I}{I_0} = 1 - \theta + \theta \cdot e^{-d/\lambda} \begin{cases} \theta = 1 & \longrightarrow \text{ layer by layer growth} \\ 0 < \theta < 1 & \longrightarrow \text{ island growth} \end{cases} \tag{4.1}$$

where the θ parameter stands for the area percentage occupied by islands. From the same considerations, the C_{1s} signal should be described by the relation:

$$\frac{I}{I_0} = \theta(1 - \cdot e^{-d/\lambda}) \begin{cases} \theta = 1 & \longrightarrow \text{ layer by layer growth} \\ 0 < \theta < 1 & \longrightarrow \text{ island growth} \end{cases} \tag{4.2}$$

The inelastic mean free path values employed for the fit analysis of Ti_{2p} and C_{1s} signals are 1.9 and 2.1 nm, respectively. They have been calculated from the inelastic mean free path relation for inorganic compound [147]:

$$\lambda = \frac{49/E^2 + 0.11 \cdot \sqrt{E}}{\rho} \tag{4.3}$$

where E is the kinetic energy of the escaping electrons (789.8 eV for electrons originated from the Ti2 orbital and 963.7 eV for the C_{1s} orbital) and ρ is the CuPc density (1.65 g/cm^3 as reported by [148]).

These graphs highlight that the organic deposition on our TiO_2 surface is not suitably depicted by any of the typical growth models. This phenomenon can be explained by the peculiar morphology of our TiO_2, here acting as a substrate of the organic deposition: the surface area of porous and nanostructured materials is really wide and rough, therefore their organic decoration probably occurs in a more complex and disordered way. This implies that the upper x-scale of Figure 4.3 and the x-scale of Figure 4.4 suggest merely the average thickness of the deposited CuPc film as if we were dealing with a flat surface, but the organic material can not be considered arranged on the TiO_2 surface in homogenous and ordered way. However, this parameters

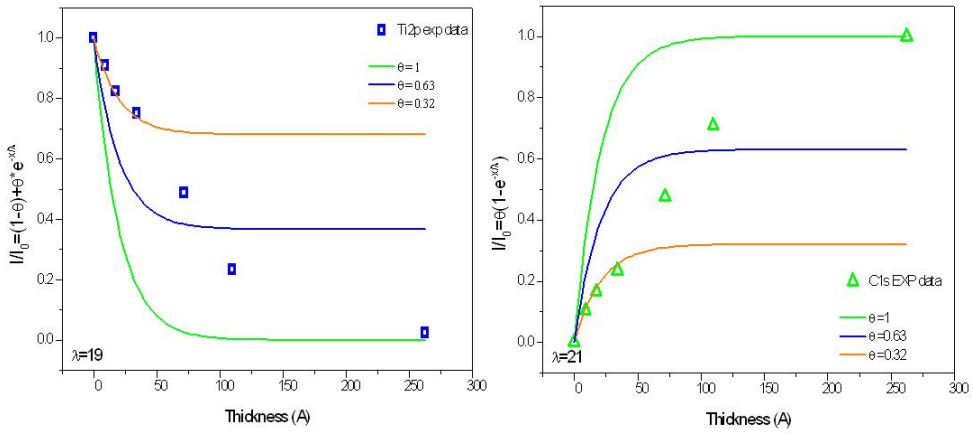

Figure 4.4: Trend of the Ti_{2p} (a) and C_{1s} (b) signals plotted versus the average thickness of the CuPc film (exp. A). The mismatch between the experimental data and the theoretic lines shows that the organic decoration of our TiO_2 surface cannot be suitably described by any of the typical growth models.

is quite helpful to get the picture of the deposited molecules amount.
The same XPS spectra have been used also to extract quantitative information about the stoichiometry of both the organic and inorganic counterparts. In order to get comparable quantities, the areas of the different core levels have been corrected by different Sensitivity Factors, as explained in section 1.4.4. The O/Ti ratios calculated for each coverage are reported in Table 4.1. As already demonstrated, the employed PMCS deposition parameters induce a superstoichiometry in oxygen in our clean TiO_2 surface. The O/Ti ratio calculated at the several CuPc coverages are consistent (considering the error of $\pm$ 0.04) with the value obtained for the clean surface. Only the $CuPc_A^{71}$ layer shows a quite different stoichiometry, but the low intensity of its O_{1s} and Ti_{2p} signals probably makes the calculation at this coverage less reliable. With regard to the molecule stoichiometry, Table 4.2 reports the atoms number estimated for each element. It can be noticed that they are in perfect agreement with the theoretical atoms number, for all coverage steps. This is a very important result as it gives evidence that our deposition method does not induce any degradation in the chemical structure of the original molecule. Therefore we can be confident that the peculiar prop-

erties of CuPc molecules have been preserved during the deposition, even after having experienced thermal sublimation and kinetic processes with the substrate.

	$CuPc_A^0$	$CuPc_A^{10}$	$CuPc_A^{17}$	$CuPc_A^{23}$	$CuPc_A^{48}$	$CuPc_A^{71}$	$CuPc_A^{100}$
O/Ti	2.20	2.16	2.22	2.18	2.16	2.06	-

Table 4.1: Calculated stoichiometry of TiO_2 for all the CuPc coverages of experiment A, expressed as O/Ti ratio.

	$CuPc_A^{10}$	$CuPc_A^{17}$	$CuPc_A^{23}$	$CuPc_A^{48}$	$CuPc_A^{71}$	$CuPc_A^{100}$	Theory
C	32.3	31.6	32.1	31.6	32.1	32.3	32
N	7.8	8.4	7.8	8.4	8.1	7.8	8
Cu	0.9	1.1	1.1	1.1	1.1	0.9	1

Table 4.2: Calculated stoichiometry of CuPc molecule, for all coverage steps of experiment A, expressed as atoms number per each element.

4.1.2 High resolution XPS

All the binding energy regions analyzed in this last section have been investigated by XPS measurements at PE=10 eV as well. This particular analysis condition allows a better resolution of the observed features and an improved reliability of their binding energy values, both needed to perform a correct analysis about the involved chemical species. Obviously, these advantages are to detriment of intensity, therefore the core level signals acquired at PE=10 eV are expected to be less intense then those discussed in the last section.

Figure 4.5 (a) displays the normalized high resolution spectra of C_{1s} core level at all CuPc coverages. The contribution of the adventitious carbons lying on the gold substrate has been already removed. As a first step, we have fitted the C_{1s} spectrum of the last deposition ($CuPc_A^{100}$), by adopting the model obtained from the XPS measurements on bulk CuPc, performed at the ELETTRA synchrotron (section 3). However, it has to be noticed that the spectrum under consideration shows more broadened features with

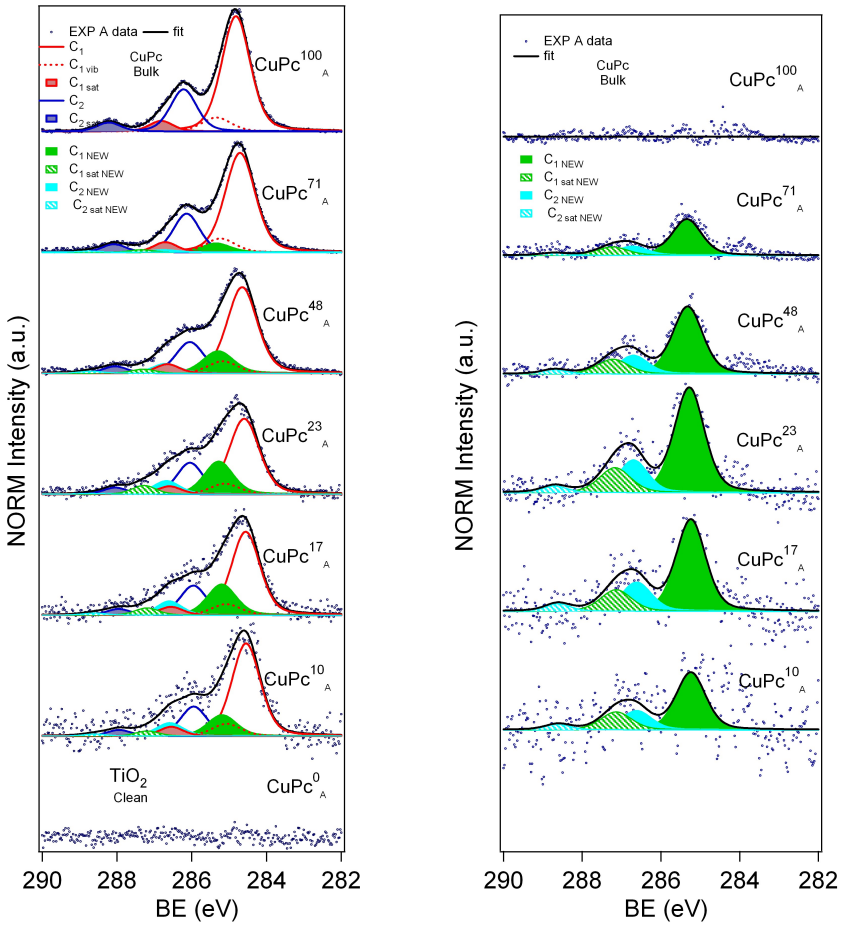

Figure 4.5: (a) High resolution C_{1s} spectra acquired at the different coverages of experiment A, showing the typical fitting components of the bulk molecule and other new components. All spectra areas have been normalized in order to allow a better comparison among the different CuPc coverages. Picture (b) represents the same spectra, at whom the typical molecule components have been subtracted.

respect to the CuPc C_{1s} core level reported in Figure 3.2.B. This is a consequence of the different resolution of the analysis apparata, therefore in the present case a FWHM correction of about + 20% has to be considered. In this way, the $CuPc_A^{100}$ spectrum of Figure 4.5.a. can be perfectly deconvolved by C_1, C_{1vib}, C_{1sat}, C_2 and C_{2sat} contributions of Table 3.1, keeping the same reciprocal energy gaps and area ratios.

By simply observing the shapes of all the other spectra, it is clear that this

bulk fit model is not suitable for the deconvolution of the intermediate coverages. In fact, the step-by-step deposition of the organic thin film onto the inorganic material leads to a continuous change of the C_{1s} line shape, from the titanium dioxide substrate up to the formation of the complete molecular film. In particular, the regions 285-286 eV and 287-288 eV can not fitted at all, unless considering the introduction of new components. The need of additional features gives evidence that the chemical environment of the investigated carbon atoms (or at least a part of them) is not the typical one of CuPc. This phenomenon can be ascribed to the formation of chemical bonds of the carbon atoms with the TiO_2 surface. As in the last section we have assumed a complex organic decoration of the TiO_2 surface, our hypothesis is that only a fraction of the deposited molecules have reacted with the surface, while the other part of molecules will experience weak interactions with organics rather strong chemical interactions with the inorganic surface. Therefore, we can suppose that our core-level spectra result from the contributions of two kind of CuPc molecules, reacted and unreacted. While the unreacted molecules should be perfectly described by the fit model related to the bulk CuPc, the deconvolution of reacted molecules is more complex. The latters probably don't form covalent bonds as whole molecules, but they interact with surface with only a fraction of their atoms. Moreover, we cannot exclude that the different kind of atoms show different reaction efficiency. The complex behavior of these molecules implies that they should be represented by both old components (located at the same BE of those related to unreacted molecules) and new components rising from the formation of new covalent bonds with surface. We have tentatively deconvolved our spectra by using this new fit model, having 9 contributions: the first five peaks represents the contributions of all the atoms coming from the unreacted molecules , so having the same energy distance and FWHM used for the $CuPc_A^{100}$ fit. The further new 4 peaks represent the C_1, C_{1sat}, C_2 and C_{2sat} of the reacted components. The latters, indicated with the label "NEW", are found to be shifted by $d = +\ 0.66$ eV from their corresponding peaks. All parameters of this fit model have been reported in Table 4.3. It can be noted that all the reciprocal energy distances of NEW components are the same of the unreacted molecules peaks, as well as their FWHM. The only exception is the C_{1NEW} peak, that has been defined with a wider FWHM in order to include

also the $C_{1vibNEW}$ contribution. The absolute energies reported in Table 4.3 are then referred to the $CuPc_A^{23}$ spectrum. Considering the complexity of the fit-model, the carbon stoichiometry has to be calculated by considering both reacted and unreacted components. The relation to be satisfied by our fit model is:

$$\frac{C_1 + C_{1vib} + C_{1sat} + C_{1NEW} + C_{1satNEW}}{C_2 + C_{2sat} + C_{2NEW} + C_{2satNEW}} = 3 \tag{4.4}$$

i.e. the contribution of benzene carbons (at which partecipate both old and new components) is three time higher than the contribution of both reacted and unreacted pyrrole carbons. This is related to the absence of any change in the whole molecular electronic properties, i.e. the molecule does not break or loose groups due to chemical reactivity, as put in evidence by the organic stoichiometries at the several coverages, almost coincident with that of the non interacting phthalocyanine Figure 4.5.a shows that the aforementioned fit model is in good agreement with the experimental data for all CuPc coverages. In order to give more evidence to the new components, the same spectra have been subtracted by the unreacted peaks and then reported in Figure 4.5.b. By increasing the CuPc film thickness, a small rigid shift towards higher energies can been found in both pictures of Figure 4.5: the calculated energy difference between the $CuPC_A^{100}$ and $CuPC_A^{10}$ is 0.22 eV. This energy shift, as well the trend of the new components over all the deposition steps will be discussed later.

Now we want focus our attention on the reactivity evaluation of the other elements present in the CuPc molecule, whose core levels have been reported in Figure 4.6.

The left picture shows the normalized HR N_{1s} spectra, collected at all CuPc coverages. Even in this case, the experimental fit model presented in the last chapter is well suitable for the deconvolution of $CuPc_A^{100}$ spectrum, taking into account a FWHM correction of about +20% due to the experimental resolution. The introduction of a NEW component at +2.19 eV from the N_3 peak is needed in order to improve the fit agreement with the experimental data, suggesting a small but defined reactivity also in nitrogen atoms. As in the case of C1s core level, a small rigid shift towards higher energies can been found with the CuPc film thickness: here, the observed energy difference between the $CuPC_A^{100}$ and $CuPC_A^{10}$ is about 0.2 eV, in good agreement with what observed for C1s analysis.

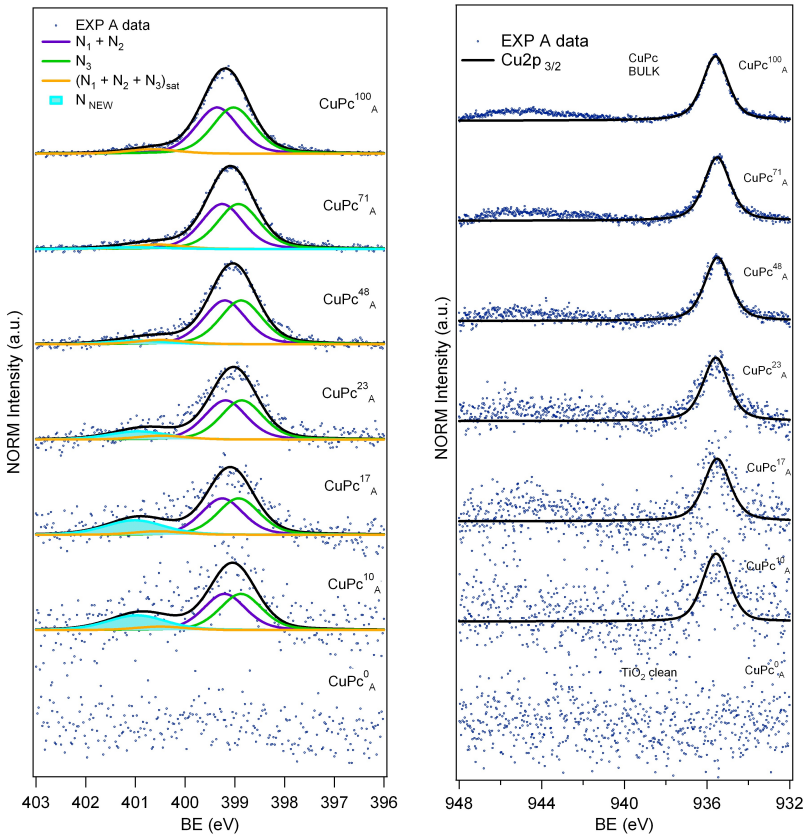

Figure 4.6: Normalized High resolution spectra acquired at the different coverages of experiment A. (a) the fitting of N_{1s} highlights the presence of new peaks respect to the typical one related to the bulk molecule, while no NEW contributions have been detected in Cu_{2p}(b)

Figure 4.6.b shows the normalized HR spectra of the $Cu_{2p^{3/2}}$ peak. No shape variation has been identified during the several deposition steps, suggesting that the copper atoms does not play a prominent role in the sensitization processes or, at least these change are below the detection limit of our experimental set up. In fact, the broader character of the Cu2p peak, as well the weaker nature of its signal, does not allow the determination of an energy shift with the CuPc coverage.

Considering the presence of new components in C_{1s} and N_{1s} spectra of the organic/inorganic interface, some interaction effects would be expected also in the TiO_2 core levels. Nevertheless, the CuPc/TiO_2 interface effects cannot be evaluated from the analysis of the Ti_{2p} and O_{1s} HR core levels, as the

main contributions to these spectra originate from the bulk material, where bulk means from the last surface layers in a 1-4 nm depth, while interface relates only to the last 0.5 nm. For this reason, the O_{1s} and Ti_{2p} collected at PE=10 eV do not lead to any reliable data interpretation and, hence, they have not been shown here. The fit models employed for all the HR core level have been summarized in Table 4.3.

Core level	Component	BE (eV)	△E (eV)	FWHM
C_{1s}	C_1	284.66	-	0.89
	C_{1vib}	285.05	+0.39	0.94
	C_{1sat}	286.56	+1.90	0.96
	C_2	286.09	+1.43	0.89
	C_{2sat}	288.02	+3.36	0.89
	C_{1NEW}	285.32	+0.66	0.92
	$C_{1satNEW}$	287.22	+2.56	0.96
	C_{2NEW}	286.70	+2.04	0.89
	$C_{2satNEW}$	288.70	+4.04	0.89
N_{1s}	$N_1 + N_2$	399.20	+0.33	1.00
	N_3	398.87	-	1.00
	$(N_1 + N_2 + N_3)_{sat}$	400.69	+1.82	1.20
	N_{NEW}	401.06	+2.19	1.40
Cu_{2p}	3/2	935.58	-	1.50

Table 4.3: Fit model for the core levels deconvolution at the CuPc/TiO_2 interface. As a rigid shift towards higher energies has been found for all core levels with the CuPc film thickness, the reported absolute energy are referred to the $CuPc_A^{23}$ spectrum.

After the identification of a good fit model for each core level, we can evaluate the trend of the interface effects during the several deposition steps. In figure 4.7.a, the percentages of the new components over the reference core level have been plotted versus the CuPc coverage. At the beginning of the CuPc deposition, the carbon atoms (black data) show very weak reactivity; then the percentage of NEW components increases up to the $CuPc_A^{23}$ cover-

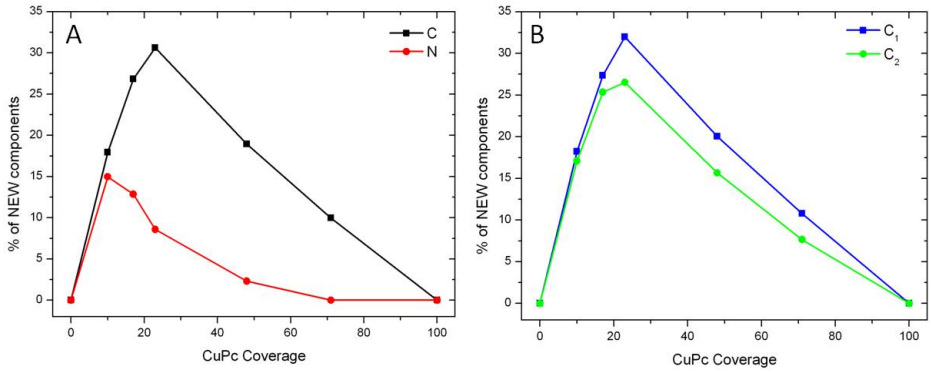

Figure 4.7: (A) Percentage of NEW components in the C1s (black line) and N1s (red line) core levels versus the CuPc coverage (experiment A); (B) Percentage of NEW components in the benzene (blue line) and pyrrole (green line) carbon atoms.

age, where it reaches the maximum values of 32%. By crossing this point the NEW components become weaker and weaker, completely disappearing at $CuPc_A^{100}$. This behavior gives further information about the deposition process: in particular, this implies that the impinging molecules can find some clear TiO_2 surface up to the $CuPc_A^{23}$ coverage, then they grow only on the organic layer. On the other hand, the N_{1s} NEW component shows its maximum intensity at the first deposition step, then it gradually disappears. The different behavior of the NEW components in C_{1s} and N_{1s} core levels may be tentatively explained with the presence of different kinds of processes that originate their chemical bonds: for example, the nitrogens reactivity may result just by the first interaction molecule/TiO_2, explaining its maximum effect just at the beginning of the deposition and also the poor efficiency of the process at higher coverages. On the contrary the carbons reactivity may be activated also by diffusion processes on the TiO_2 surface, that would explain a more efficient reactivity at increasing deposition time, up to the complete coverage of the TiO_2 surface. However, it has to be considered that the fit model and therefore the reactivity behavior are probably more reliable in C_{1s} than in N_{1s} spectra, due to the poorer signal of the latter. As the high intensity of C_{1s} data allows also the identification of the different chemical species of carbons, we have compared the reactivity of benzene and pyrrole carbon atoms during the sensitization process. The blue (green)

	$C_1 + C_{1vib} + C_{1sat}$	$C_{1NEW} + C_{1satNEW}$	$C_2 + C_{2sat}$	$C_{2NEW} + C_{2satNEW}$
$CuPc_A^{10}$	20	4	7	1
$CuPc_A^{17}$	17	7	6	2
$CuPc_A^{23}$	16	8	6	1
$CuPc_A^{48}$	19	5	7	1
$CuPc_A^{71}$	21	3	7	1
$CuPc_A^{100}$	24	0	8	0

Table 4.4: Number of the reacted/unreacted carbons per molecule, calculated for each CuPc coverage of experiment A

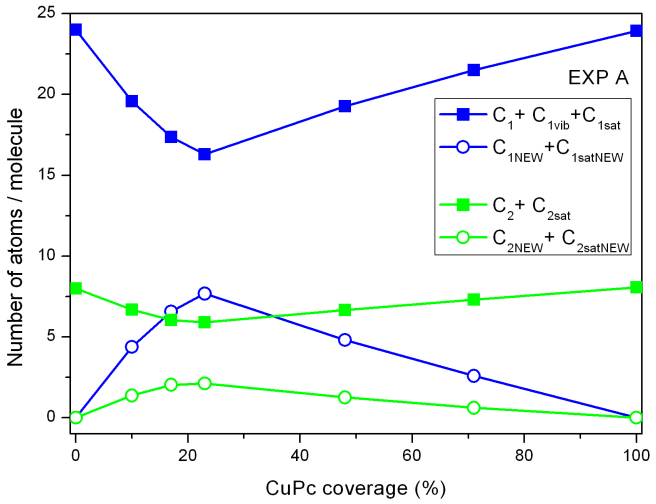

Figure 4.8: Trend of the reacted/unreacted carbons per molecule, for each CuPc coverage of experiment A (see Table 4.4)

scatter of Figure 4.7.b represents the percentage of the new benzene (pyrrole) carbon contributions over all the benzene (pyrrole) peaks. The trend of both chemical species is quite similar, even if a more efficient reactivity with surface may be attribute to benzene carbons. Finally, the number of the reacted/unreacted carbons per molecule have been calculated for each CuPc coverage. These values are reported in Table 4.4 and represented in Figure 4.8.

4.1.3 UPS

Figure 4.9 represents the He I (a) and He II (b) UPS spectra of the CuPc/TiO_2 interface for increasing thickness of the organic film, deposited by high kinetic energy. A progressive change in the line shape of the acquired spectra

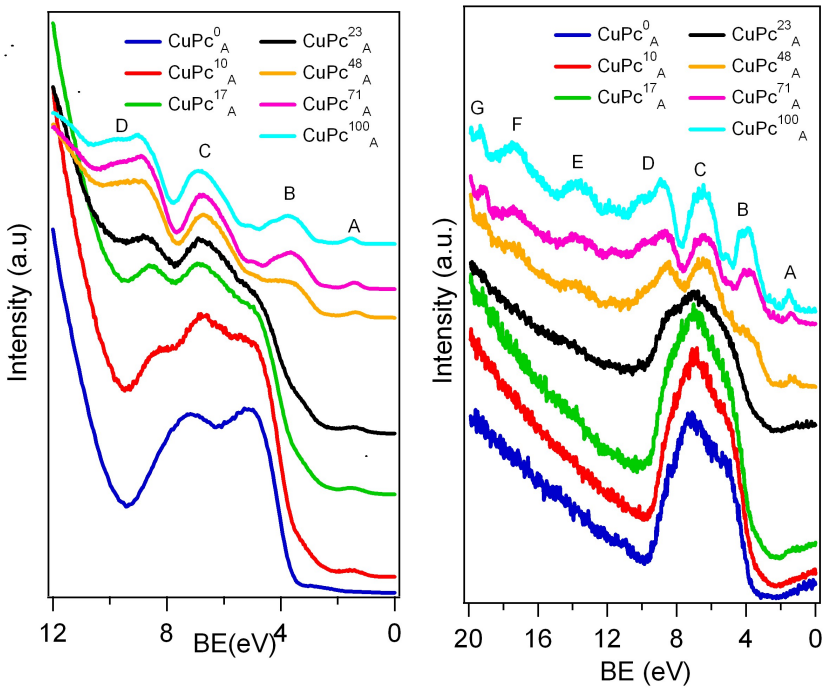

Figure 4.9: He I (a) and He II (b) UPS spectra of the CuPc/TiO_2 interface for increasing thickness of the organic film (deposited by high kinetic energy)

can be observed in both pictures, giving evidence of the increasing CuPc coverage of the TiO_2 surface. The valence band of each CuPc coverage shows the same features in both pictures, except to some intensity difference ascribable to cross-section effects. In fact, the probability of the photoemission by a specific orbital is strongly affected by the impinging photon energy. For the same motivation, the $CuPc_A^{100}$ spectra of both pictures (representing to the bulk molecule) show very different line shapes with respect to the CuPc UPS spectrum collected by a photon energy of 90 eV in Figure 3.5. However, a careful comparison of the He I and He II UPS spectra with that reported in Figure 3.5 allows the identification and the labeling of all the observed CuPc features, whose assignment has been described in the previ-

ous chapter. These cross-section effects make the photon energy of the He I line (21.2 eV) particularly suitable for the detection of the typical features of titanium dioxide, so the $CuPc_A^0$ spectrum shows higher resolution in the left picture than in the right one. Moreover, the slow rising of the CuPc features of $CuPc_A^{10}$-$CuPc_A^{23}$ coverages can be well-observed in the He I spectra, while contemporary He II investigations show just almost featureless valence bands. This is probably a consequence of the poor CuPc amount of the first deposition steps, that can be hardly detected by the weak intensity of the He II radiation. On the other hand, the nitrogen and carbon 2s orbital are found to be more sensitive to the excitation from the He II photon energy (40.8 eV), so the features from E to G are well marked only in the right picture. By observing the line shapes evolution of Figures 4.9 (a) and (b), we can observe that the complete disappearing of the typical features of titanium dioxide corresponds to the $CuPc_A^{48}$ coverage. As the depth investigated by UPS (1 nm) is definitively thinner than XPS (10 nm), this observation suggests that a complete layer of CuPc is formed only between the $CuPc_A^{23}$ and $CuPc_A^{48}$ coverage. Therefore, we have the confirmation that the CuPc decoration of the TiO_2 surface occurs by island formation. Unfortunately, no clear evidence of a reactivity phenomenon at the hybrid interface can be extracted from a direct comparison of the UPS spectra: in fact the intermediate coverages do not show any new feature, attributable to some chemical reaction at the interface. This does not exclude the presence of some hybridization effects of the topmost occupied states, because they could be revealed by an accurate fitting of all spectra. However, the background variation due to secondary electrons contribution would not grant a good reliability of this method.

Further quantitative information on the electronic structure can be obtained from the UPS analysis. In Figure 4.10 the secondary onset (a) and the HOMO (b) regions of the He I UPS spectra are reported. As already discussed in chapter 2, the bottom spectrum (blue line) of Figure 4.10.b shows the presence of contributions near the valence band edge, ascribable to surface defects states probably related to the material morphology, such as grain boundaries and clusters aggregation. The work function (Φ) of the titanium dioxide is obtained by subtracting the secondary onset cutoff from the excitation energy. The ionization energy (IE) of the molecule is calculated by

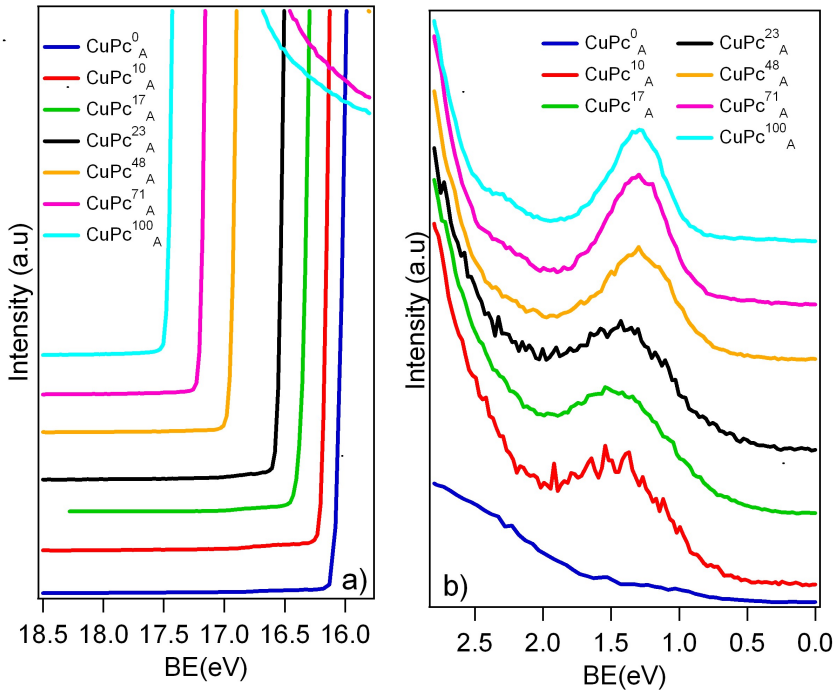

Figure 4.10: Secondary onset (a) and HOMO (b) regions of the He I UPS spectra.

the subtracting the energy gap existing between the SO and the HOMO cut-offs (i.e., the spectrum length) from the photon energy. Moreover, the VB (HOMO) cutoff identifies the energy distance between the top of the highest occupied orbital and the Fermi level. Figure 4.11 (a) and (b) show the trends of all these values with the CuPc film thickness. The work function and the valence band-E_F distance of the clean TiO_2 have been evaluated to be 5.27 and 3.59 eV, respectively, in agreement with values reported in chapter 2. We observe that the CuPc ionization energy and HOMO-E_F distance strongly depend on the several experiment stages. In particular, the *IE* is found to be 4.93 eV for the bulk molecule, but it increases up to 5.83 eV in the $CuPC^{10}_A$ layer. Moreover in the $CuPC^{100}_A$ coverage, the HOMO is located at 1.13 eV below the Fermi level, whereas at the beginning of the hybrid interface it is found to be at 0.75 eV below E_F.

This phenomenon can be explained by an energy alignment phenomenon at the interface. Greiner et al. have recently elaborated an "Universal energy-level alignment of molecules on metal oxides" model [149]. They have per-

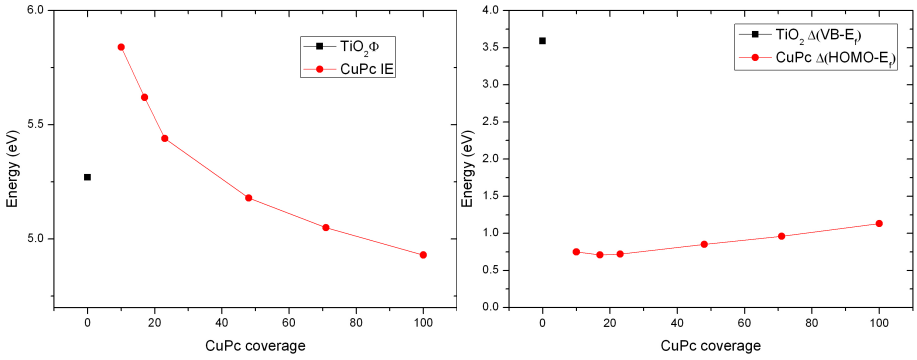

Figure 4.11: Experimenta A: (a) Work function of the clean TiO_2 and CuPc ionization energies values as a function of the CuPc coverage. (b) Energy distance of the TiO_2 valence band and of the CuPc HOMO from the Fermi level.

formed layer-by layer UPS measurements on a large set of metal oxides and molecules, giving a mathematical formalism (based on fundamental thermodynamic and electrostatic principles) to predict energy alignment in the case of merely weak and physisorptive organic/inorganic interactions. Their studies show that the energy alignment can be established regardless the substrate electronic structure, such as the oxide conduction/valence-band positions. The only relationship that was found to affect energy alignment was the energy difference between the substrate's work function and the organic's ionization energy. In particular they have found that for $\Phi < IE$ the HOMO-E_F offset depends on the difference between the oxide work function and the molecular ionization energy. Moreover, once the substrate's Φ has exceeded the molecule's IE, the HOMO offset establishes a minimum value, of about 0.3 eV and remains constant. Even if we should be in this last case (TiO_2 Φ > CuPc IE), the HOMO orbitals found at our interface is located at 0.75 eV below the E_F. The disagreement with the universal model of Greiner is a further confirmation that the interactions occurring at our organic/inorganic interface cannot be described by merely Wan der Walls or physisorptive forces, but they are also related to covalent bonds (as suggested by the presence of new chemical state in the core level spectra). In Figure 4.12 a schematic energy level diagram of our CuPc/TiO_2 system is represented: the values reported for the clean TiO_2 surface and the bulk

CuPc have been extracted by $CuPc_A^0$ and $CuPc_A^{100}$ spectra, respectively, while those referred to the hybrid interface have been estimated from the $CuPc_A^{23}$ intermediate coverage.

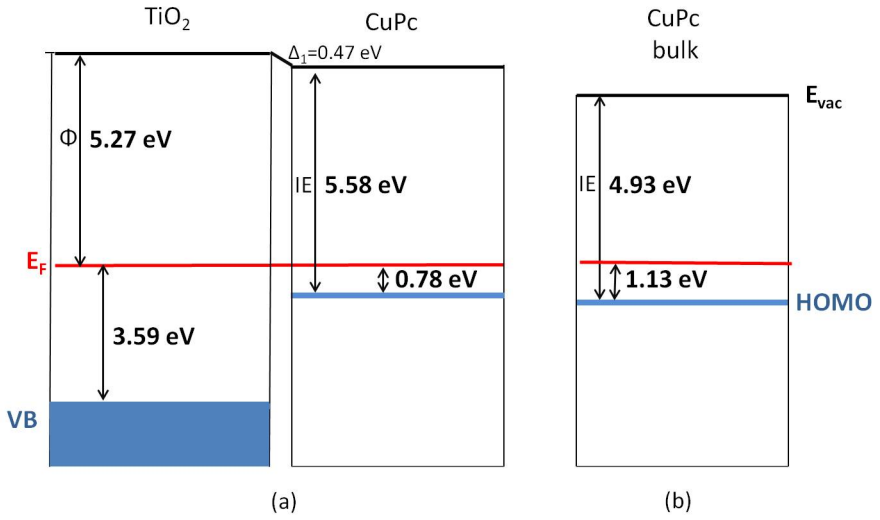

Figure 4.12: Schematic energy-level diagram of the CuPc/TiO_2 system (a) and of the bulk CuPc film (b). These band diagrams have been obtained from UPS measurements of experiment A.

4.2 Experiment B:CuPc/TiO_2 at low molecular kinetic energy

As in the previous case, the first part of this experiment consists in the growth of a 60-thick titanium dioxide film by PMCS, directly in the analysis chamber. The deposition parameters and the substrate are the same of experiment A.

Then the PMCS apparatus has been replaced by a SUMBD source, in order to deposit the CuPc molecule directly on the TiO_2 film, with a complete overlapping. In this experiment, the SUMBD source has been operated in a quasi-effusive regime: by using kripton as a carrier gas at low pressure (about 120 mbar), the kinetic energy of seeded molecules in the beam reach the much lower value of 0.5 eV. The temperatures of the beam source have been calibrated in order to keep the deposition rate at about 1 Å/min, as in

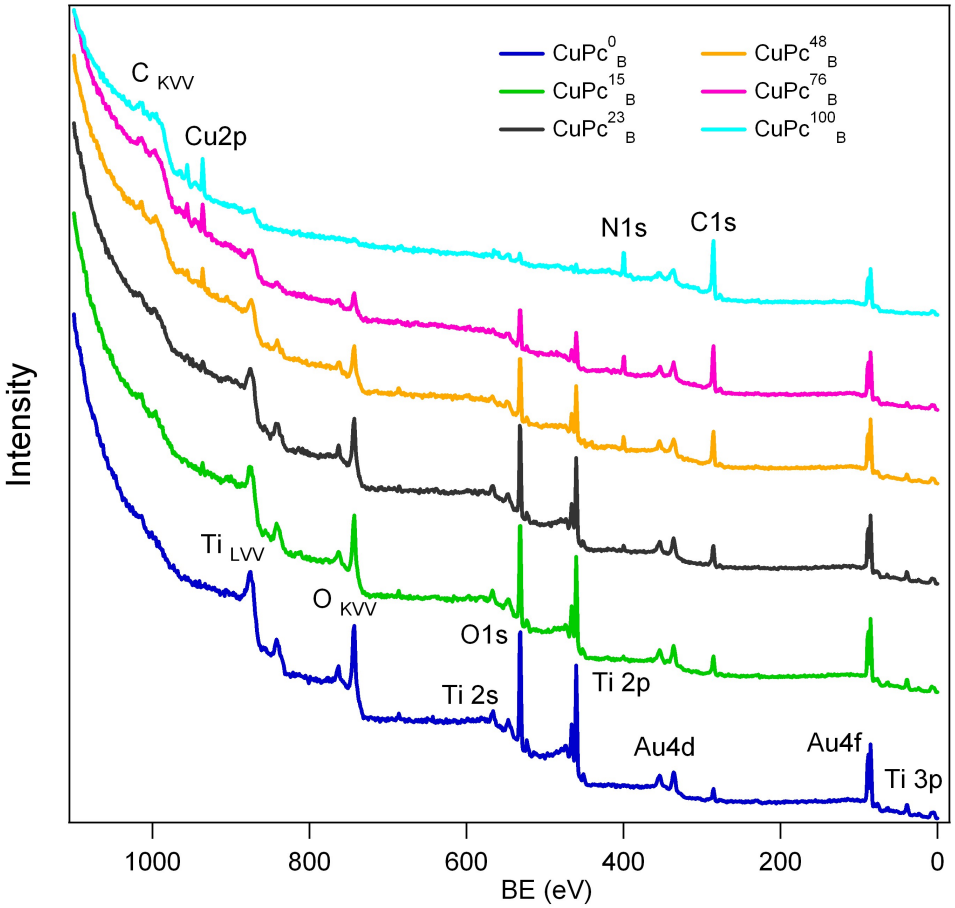

Figure 4.13: Survey spectra acquired at each deposition step of experiment B, from the clean TiO_2 to the bulk CuPc.

the previous experiment.

The molecule deposition has been performed at 4 increasing coverages up to the achievement of a thick bulk organic film. Core levels and UPS spectra have been acquired at each coverage step, from the clean TiO_2 to the bulk CuPc.

Figure 4.13 shows the XPS surveys collected at each step of the experiment: the bottom spectrum is related to the clean TiO_2 surface, the top one to the bulk CuPc film and all the other spectra are related to the 4 intermediate organic coverages. Each deposition has been labeled by using the same notation of experiment A: for example, $CuPc^{48}_{B}$ stands for the coverage of experiment B in which the CuPc amount is the 48% of the bulk CuPc film

(value extracted from the quantitative C_{1s} spectrum).
The blue line spectrum shows the typical features of titanium dioxide: the photoemissions from the Ti_{2s}, O_{1s}, Ti_{2p} and Ti_{3p} core levels are found at about 560, 530, 460 and 30 eV, respectively, while the presence of Ti_{LVV} O_{KVV} Auger lines can be observed in the regions 800-900 eV and 750-800 eV. The contributions of the 4d and 4f orbitals related to the gold substrate can be noticed at about 340 and 80 eV, respectively.
All TiO_2 features gradually reduce their intensity by increasing the CuPc coverage, up to reach a complete quenching in the top spectrum (sky-blue line). At the same time, the organic molecule structures gradually increase, up to the achievement of their maximum intensity at the $CuPc_B^{100}$ coverage: the photoemission from N_{1s}, C_{1s} and Cu_{2p} can be identified at about 400, 290 eV and 950-930 eV, respectively, while the C_{KVV} Auger transitions can be found at around 990 eV. Even in this case, there is a small contribution of C_{1s} orbitals due to the presence of adventitious carbon atoms lying on the gold substrate. This contribution is distinguishable in the clean TiO_2 film (blue line) and has been carefully evaluated and subtracted from all the C_{1s} spectra here presented. In the following sections we will examine the reference core level of each element of interests (i.e. Ti_{2p}, O_{1s}, C_{1s}, N_{1s}, Cu_{2p}), by analyzing both quantitative and high resolution spectra.

4.2.1 Quantitative XPS

XPS measurements at PE=20 eV have been collected and carefully examined, in order to extract further information about the sensitization process and the materials stoichiometry.
The trends of the core levels intensity with the increasing of the CuPc coverage are very similar to that reported in Figure 4.2 for the previous experiment, so they are not shown here. On the other hand, the behavior of their normalized areas with the deposition time t are of great interest and are represented in Figure 4.14. As expected, the Ti_{2p} e O_{1s} core levels show their maximum intensities at t=0 and as the time goes by, their percentages contemporary assume lower and lower values (within an agreement of the 1%). The linear fit of the first 5 points of the Ti_{2p} areas highlights that the CuPc/TiO_2 interface should be observable up to a deposition time of about 110 min (i.e. about 100 A-thick CuPc layer). Again, the reference data for

the bulk molecule has been achieved beyond this threshold, later on 50 minutes. The comparison of Figures 4.3 and 4.14 highlights that the formation of a complete molecular film is more rapidly achieved by a quasi-effusive source than a supersonic one.

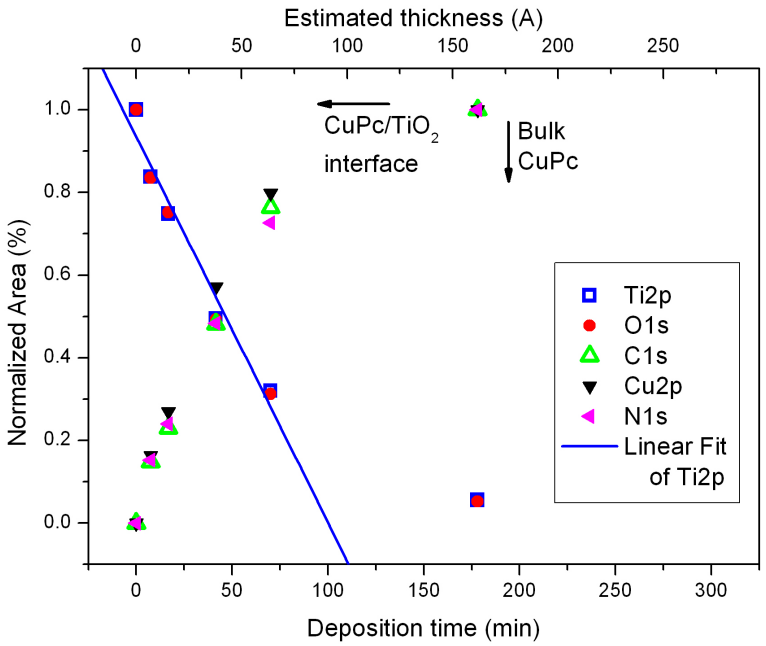

Figure 4.14: Normalized areas of the quantitative XPS data of experiment B plotted versus the deposition time (bottom x-scale) and the estimated CuPc thickness (top x-scale), grown by low energy.

This phenomenon has been thoroughly examined by comparing the Ti_{2p} (a) and C_{1s} (b) signals of both experiments with the deposition models presented in section 4.1.1 (Figure 4.15).
These graphs highlight that neither the organic deposition at low energy on our TiO_2 surface can be fully described by the conventional growth models. However, we observe that the experimental data acquired in the last experiment is closer to a layer-by-layer model than the data acquired in the previous experiment. This phenomenon could be explained by an higher mobility, possibly by diffusion, of the molecules on the TiO_2 surface, that allows a more efficient molecular coverage. On the other hand, one could expect a more "ballistic" kind of behavior in the molecular collisions at higher kinetic energies of experiment A. A similar result has been obtained in a

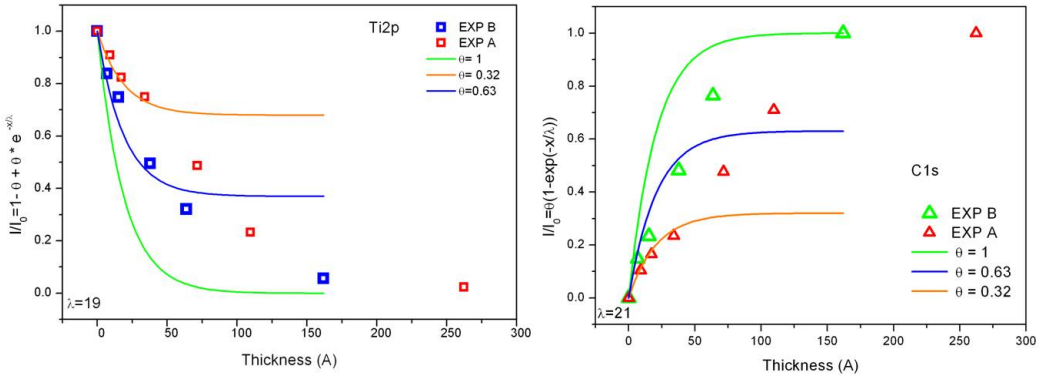

Figure 4.15: Trend of the Ti_{2p} (a) and C_{1s} (b) signals of both experiments plotted versus the average thickness of the CuPc film.

previous study performed in our laboratories and reported in [150]. Here, the deposition behaviors of the H2TPP(F) molecule grown by 0,5 eV and 25 eV kinetic energy beams have been examined and compared. In the quasi-effusive regime, dominated by weak Van der Waals forces, a layer-by-layer growth is observed. On the contrary a more complex behavior has been observed for H2TPP(F) at 25eV KE, where strong chemical interaction between the molecules and the substrate have been found [150].

	$CuPc_B^0$	$CuPc_B^{15}$	$CuPc_B^{23}$	$CuPc_B^{48}$	$CuPc_B^{76}$	$CuPc_B^{100}$
O/Ti	2.20	2.19	2.21	2.19	2.17	-

Table 4.5: Calculated stoichiometry of TiO_2 for all the CuPc coverages of experiment B, expressed as O/Ti ratio.

	$CuPc_B^{15}$	$CuPc_B^{23}$	$CuPc_B^{48}$	$CuPc_B^{76}$	$CuPc_B^{100}$	Theory
C	31.5	31.6	31.6	32.1	31.8	32
N	8.3	8.2	8.1	7.8	8.2	8
Cu	1.1	1.2	1.2	1.1	1.0	1

Table 4.6: Calculated stoichiometry of CuPc molecule deposited at low energy, expressed as atoms number per each element.

Quantitative information about the stoichiometry of our materials has been

extracted by comparing the core levels areas, corrected by specific sensitivity factors. Table 4.5 summarizes the TiO_2 stoichiometry calculated at each CuPc coverage. The O/Ti ratio of the clean surface is 2.20 (the same of the previous experiment). This value is in agreement with the O/Ti ratio calculated at each deposition stage. With regard to the molecule stoichiometry, Table 4.6 reports the atoms number estimated for each element, that are found to be in agreement to the theoretical values. This is a further evidence that the supersonic beam methods are suitable for organic thin film deposition as they don't induce any degradation in the chemical structure of the molecules.

4.2.2 High resolution XPS

In this section, the fitting analysis performed on the high resolution XPS measurements will be presented and discussed.
Figure 4.16 (a) displays the normalized C_{1s} core level at all CuPc coverages, where the contribution of the adventitious carbons lying on the gold substrate has been already removed. As demonstrated for the previous experiment, the $CuPc_B^{100}$ spectrum can be perfectly deconvolved by the fit model found by HR synchrotron measurements (see Table 3.1), keeping the same reciprocal energy gaps and area ratios, but introducing a FWHM correction of about + 20%.
Even in this case, the intermediate coverages show a broader character than the top $CuPc_B^{100}$ spectrum, requiring the introduction of new components. However, the comparison of depositions of both experiments, having similar CuPc content (i.e. $CuPc_A^{17}$ with $CuPc_B^{15}$, $CuPc_A^{23}$ with $CuPc_B^{23}$ and so on), highlights some significant differences. In fact, the spectra of experiment B show significantly lower FWHM with respect to their respective spectra of experiment A, suggesting a poorer reactivity of the molecules deposited at low energy. In order to asses this hypothesis, the same fit model presented in Table 4.3 and satisfying the relation 4.4 has been applied to all the intermediate coverages of experiment B. The results of this deconvolution has been displayed in Figure 4.16.a , showing a good agreement with the experimental data. The same spectra, at which the unreacted molecule peaks have been subtracted, are represented in Figure 4.16.b. By comparing the latter with Figure 4.5.b, we gain a clear further evidence that the contribution of NEW

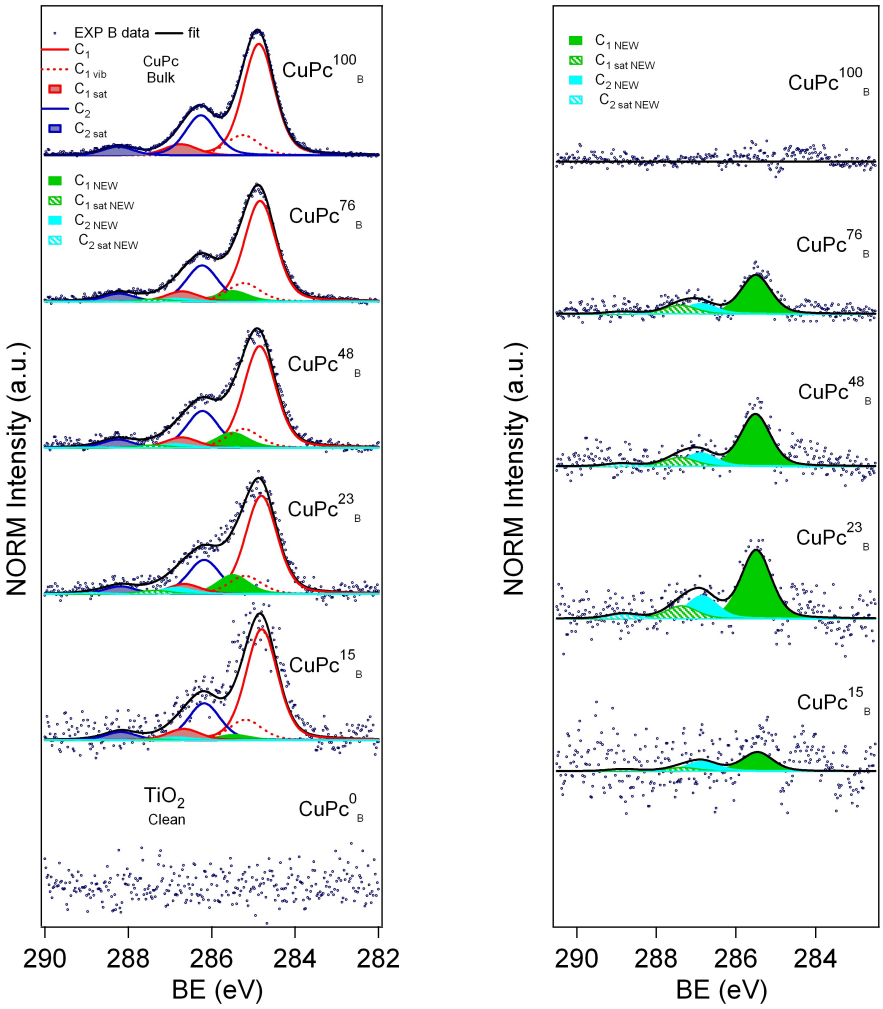

Figure 4.16: (a) High resolution C_{1s} spectra acquired at the different coverages of experiment B, showing the typical fitting components of the bulk molecule and other new components. All spectra areas have been normalized in order to allow a better comparison among the different CuPc coverages. Picture (b) represents the same spectra, at whom the typical molecule components have been subtracted.

components is definitely higher at high molecular kinetic energy deposition.

Figure 4.17 shows the normalized HR N_{1s} (a) and $Cu_{2p^{3/2}}$ (b) spectra collected at all CuPc coverages of experiment B. As already observed in Figure 4.6, the fit model of the bulk molecule is well suitable for the deconvolu-

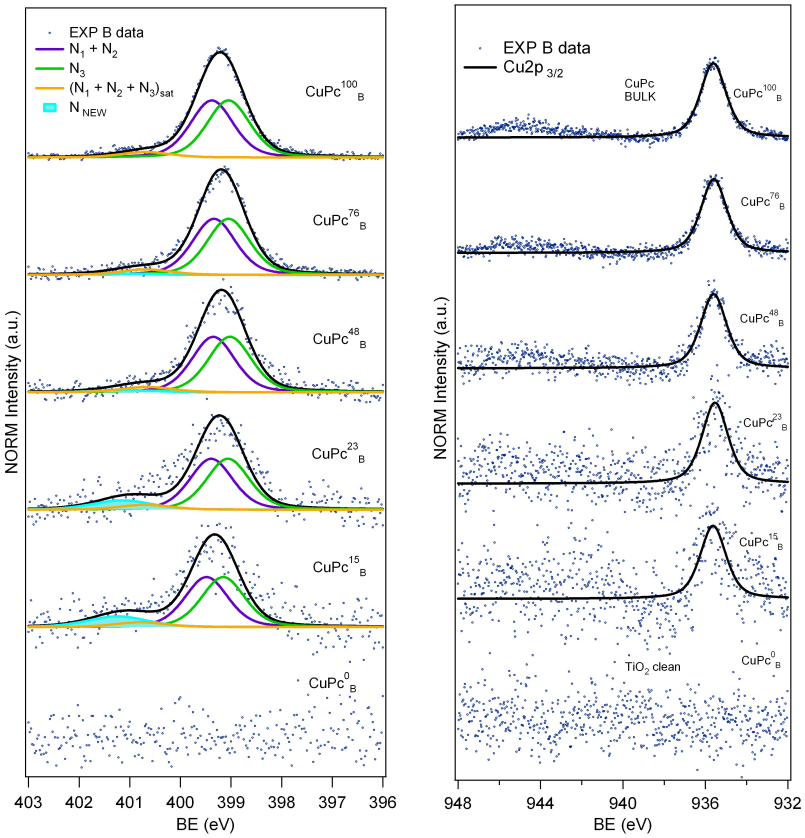

Figure 4.17: Normalized High resolution spectra acquired at the different coverages of experiment B. (a) the fitting of N_{1s} highlights the presence of new peaks respect to the typical one related to the bulk molecule, while no NEW contributions have been detected in Cu_{2p}(b)

tion of all $Cu_{2p}^{3/2}$ spectra, but not for all the N_{1s} data. Except the $CuPc_B^{100}$ spectrum, all intermediate coverages needs the introduction of a new peak in the fit model. We remind that all the fit models employed in this section are the same discussed in the previous experiment, so the reader can referred to Table 4.3 to get a summary of all fit parameters. In Figure 4.18.a, the percentage of the new components of experiment B have been plotted versus the percentage of CuPc coverage. The same graph displays also the results of the previous experiment (dotted lines), in order to facilitate the comparison. Carbons (black data) and nitrogens (red data) show a similar dependence on the molecular coverage in both experiments: in particular, the NEW components related to C1s core level reach their maximum percentage

at the $CuPc_A^{23}$ coverage, while the N_{1s} NEW component shows its highest intensity at the first deposition step, then it gradually vanishes. The same graph highlights also an important difference between the two experiments: the carbons reactivity has more than doubled when the molecule deposition have been achieved at high kinetic energy. On the contrary, any variation in the nitrogens sensitization efficiency can be observed by changing the deposition conditions. Figure 4.18.b shows the specific reactivity of benzene and

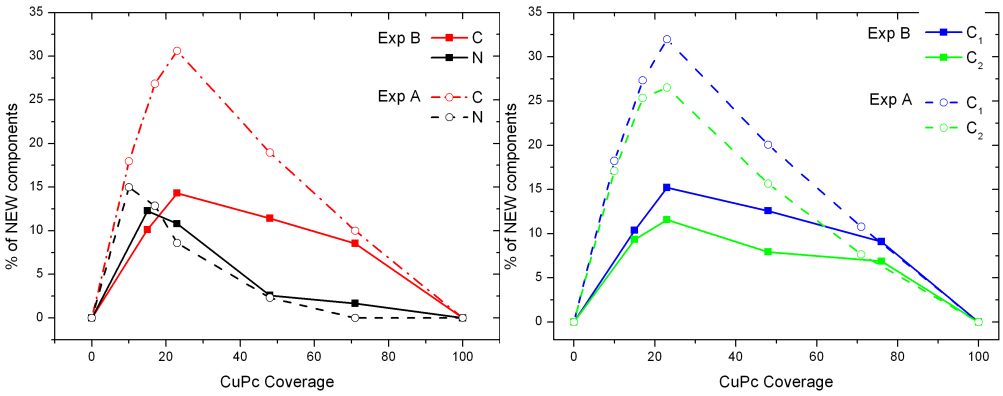

Figure 4.18: (A) Percentage of NEW components in the C1s (black line) and N1s (red line) core levels versus the CuPc coverage of experiment B; (B) Percentage of NEW components in the benzene (blue line) and pyrrole (green line) carbon atoms.

	$C_1 + C_{1vib} + C_{1sat}$	$C_{1NEW} + C_{1satNEW}$	$C_2 + C_{2sat}$	$C_{2NEW} + C_{2satNEW}$
$CuPc_B^{15}$	22	2	7	1
$CuPc_B^{23}$	20	4	7	1
$CuPc_B^{48}$	21	3	7	1
$CuPc_B^{76}$	22	2	7	1
$CuPc_B^{100}$	24	0	8	0

Table 4.7: Number of the reacted/unreacted carbons per molecule have been calculated for each CuPc coverage (low energy)

pyrrole carbon atoms during the sensitization process of both experiments: here, the slightly higher efficiency of benzene carbons than pyrrole carbons can be observed in both cases. The number of the reacted/unreacted carbons per molecule have been calculated for each CuPc coverage. These values are

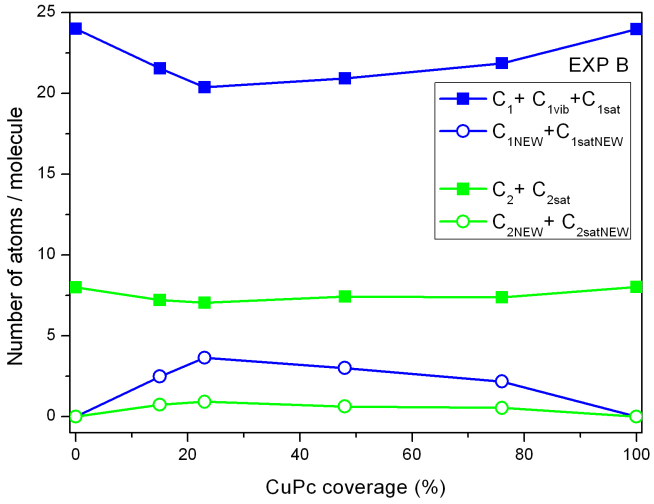

Figure 4.19: Trend of the reacted/unreacted carbons per molecule, for each CuPc coverage of experiment B (see Table 4.7)

reported in Table 4.7 and represented in Figure 4.19. These results are the evidence that the kinetic energy of the molecular beam is a critical parameter during the sensitization precesses: in particular high kinetic depositions are found to induce a more complex organic decoration of the TiO_2, as it probably inhibits surface diffusion processes or it causes backscattering phenomena. Despite this disordered type of growth, the carbons reactivity is improved of more than 100% in high energy deposition

4.2.3 UPS

The He I (a) and He II (b) UPS spectra of the CuPc/TiO_2 interface, deposited by low kinetic energy, are represented in Figure 4.20 Both pictures show the progressive spectral evolution of the CuPc features, rising from the organic coverage increasing. The valence band of each CuPc coverage shows mostly the same features in both Figures 4.20 (a) and (b), except to the intensity differences related to cross-section effects. Even in this case, the disappearing of the typical shape of titanium dioxide valence band is found at the $CuPc_B^{48}$ coverage, suggesting that 1 nm-thick CuPc layer is achieved between the $CuPc_B^{23}$ and $CuPc_B^{48}$ coverage. We remind that the $CuPc_B^{48}$ coverage has been achieved with half the deposition time respect to $CuPc_A^{48}$ of the previous experiment, confirming that the low energy deposition allows

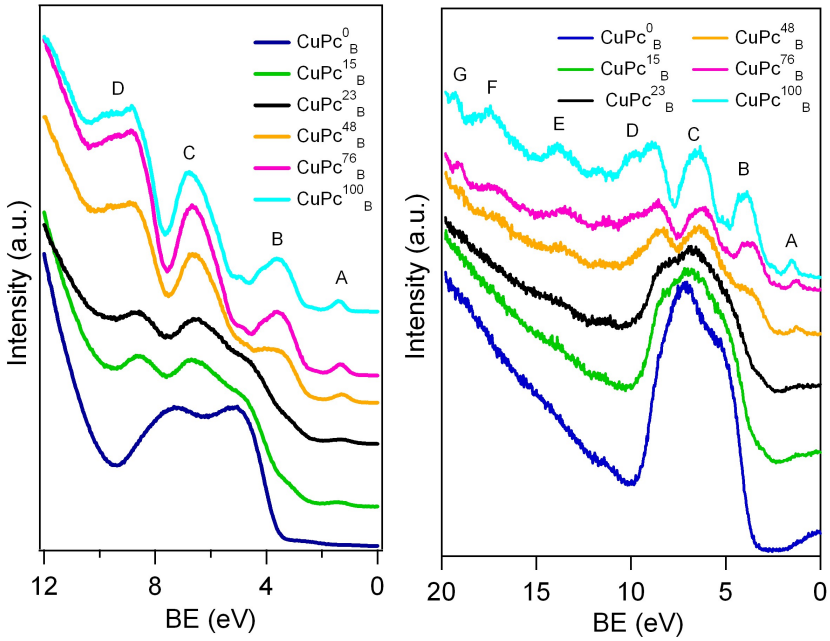

Figure 4.20: He I (a) and He II (b) UPS spectra of the CuPc/TiO_2 interface for increasing thickness of the organic film (deposited by low kinetic energy)

a more efficient and quicker substrate coverage. As in the previous experiment, no clear evidence of reactivity phenomena at the hybrid interface can be observed from the UPS spectra.

Figure 4.21 shows the secondary onset (a) and the HOMO (b) regions of the He I UPS spectra.

Figure 4.22 (a) and (b) show the trends of all these values with the CuPc film thickness. Even in this case, the bottom spectrum (blue line) of Figure 4.21.b shows the presence of contributions near the valence band edge, ascribable to surface defects states probably related to the material morphology, such as grain boundaries and clusters aggregation. The quantitative values extracted by the UPS analysis are comparable to those of the previous experiment. The work function and the valence band-E_F distance of the clean TiO_2 have been evaluated to be 5.28 and 3.58 eV, respectively. The bulk CuPc ionization energy and HOMO-E_F are 4.98 and 1.08 eV, respectively. By approaching to the hybrid interface, the latters are found to be shifted, due to the energy alignment phenomenon occurring at the interface. In par-

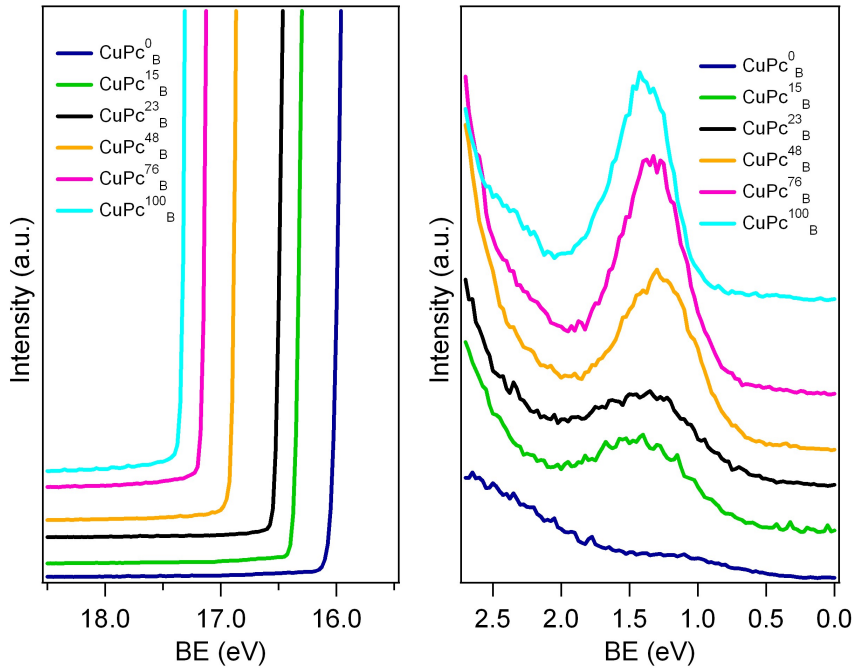

Figure 4.21: Secondary onset (a) and HOMO (b) regions of the He I UPS spectra (experiment B).

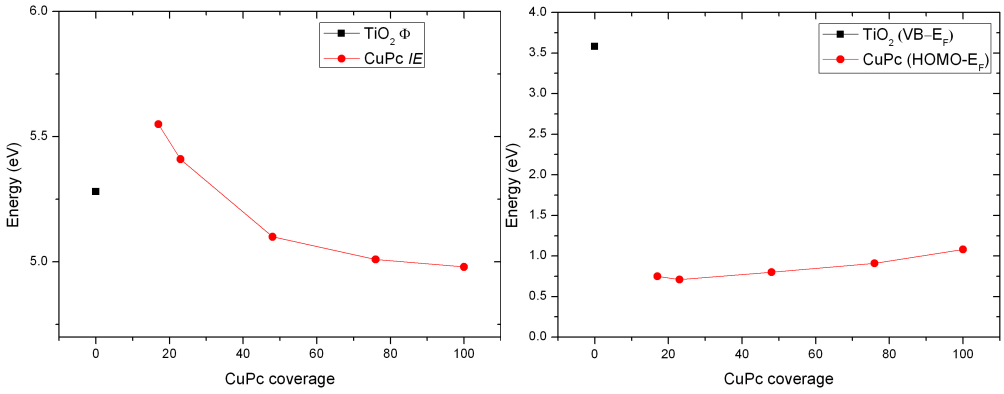

Figure 4.22: (a) Work function of the clean TiO_2 and CuPc ionization energies values with the CuPc coverage. (b) Energy distance of the TiO_2 valence band and of the CuPc HOMO from the Fermi level.

ticular the $CuPc_B^{15}$ coverage show a molecular ionization energy of 5.55 eV and an HOMO offset of 0.75 eV, in agreement with values reported for the $CuPc_A^{17}$ of the previous experiment. Differently from the XPS core levels

analysis, the UPS studies on CuPc/TiO_2 at low molecular kinetic energy have not revealed any differences from the case of CuPc/TiO_2 grown at high molecular kinetic energy.

4.3 Conclusions

Two hybrid systems showing the same organic/inorganic configuration have been investigated by surface photoelectron spectroscopies. In both cases the inorganic material consists in superstoichiometric titanium dioxide (O/Ti $\approx$ 2.20), grown by PMCS technique. The organic film has been deposited onto the TiO_2 layer by molecular seeded beam, working in both supersonic (experiment A) and quasi-effusive (experiment B) regime. The photoelectron spectroscopy measurements have been performed at increasing CuPc coverages, in order to test the role of kinetic energy at each stage of the sensitization process. The core levels intensities behavior with the deposition time indicates that in both experiments the organic deposition on our TiO_2 surface is not suitably depicted by any of the simple growth models. This phenomenon can be explained by the peculiar morphology of our porous and nanostructured TiO_2, whose surface area is too wide and rough for the achievement of an ordered organic decoration. Actually the lower energy deposition would lead to a more efficient and quicker molecular coverage of the TiO_2 substrate, probably due to a higher surface diffusion of the impinging molecules, to be compared to the "ballistic-like" behavior that is reasonably expected for molecular beams at higher kinetic energies . However, high resolution XPS measurements show that this higher coverage does not induce a surface reactivity increase. Considering that the amount of CuPc is the same, the hybrid system achieved by supersonic beam at high kinetic energy shows an improvement of the chemical reactivity of more than 100%, with respect to the quasi-effusive case. This suggests that supersonic beams methods are ideally suitable for the deposition of organic and inorganic materials, up to the activation of sensitization processes at the interface. Finally, UPS spectra at different photon energies have been analyzed and compared. Both hybrid systems show almost the same electronic structure and a strong energy-band alignment at the interface.

Chapter 5

Outlook

One of the major goals of this work is to demonstrate that chemical bonds at hybrid interfaces can be activated by high kinetic energy processes. This result has been achieved by comparing two systems with the same configuration (TiO_2/CuPc), where the molecule deposition has been carried out by molecular seeded beams at both high and low kinetic energies. These sensitization experiments have performed at the Trento IMEM-CNR laboratories, where all the supersonic apparata have been conceived and developed. The capacity to couple deposition sources to surface spectroscopies is an important opportunity, as it enables the analysis of the hybrid interface at each stage of its formation, avoiding environmental contaminations. The reactivity of different molecular elements has been evaluated by the presence of new components in their related core-level spectrum. These new features suggest the effective formation of new chemical species induced by chemical bonds with the metal oxide surface. The evolution of these new components has been monitored over all the deposition steps, in order to evaluate the reactivity dependence of the atomic elements on the different interface stages and on the initial kinetic energy of the molecule. In particular, an enhanced carbons reactivity efficiency has been observed in the hybrid system obtained by supersonic seeded beams. This suggests that supersonic beams methods, already employed in the deposition of organic and inorganic materials, are suitable as well for the achievement of sensitization processes at their interface. This achievement pave the way to a novel class of hybrid systems overcoming the limitations inherent in conventional equilibrium processes and possibly to hew generation of devices. The evaluation of the molecu-

lar reactivity by photoelectron spectroscopies has been made possible by the propaedeutical analyses performed at the synchrotron ELETTRA in Trieste. Taking advantages of the high resolution of this facility, a well suitable fit model has been found for the bulk CuPc molecule. We also determined the influence of the metal core in the molecular electronic properties, by further comparative investigations on the free-base phthalocyanine. Moreover, this thesis work gives a comprehensive knowledge on the as-grown TiO_2, deposited by PMCS, by means of diagnostic techniques at the nanoscale. The experimental evidence of non conventional room temperature excitonic emissions from the as-grown TiO_2 NPs have been obtained by cathodoluminescence investigations, while HRTEM studies reveal the crystalline and mixed-phase character of the NPs. XPS measurements show also that our NPs are superstoichiometric in composition, a quite difficult task to achieve and a very interesting type of material to further investigated All the results presented highlight the suitability of Supersonic Beam approaches in the achievement of nanostructured metal oxides, organic thin films and molecular sensitization processes. Therefore, the natural development of the present work would be the study of the structural and luminescence properties of the hybrid CuPc/TiO_2 as well as the extension of the entire work schedule to other interesting molecules, such as porphyrins. We envisage very interesting perspectives, where the combination of such properties in novel nanosystems could be fully exploited in new classes of devices including sensing and energy.

List of Figures

List of Tables

Bibliography

[1] G. Scoles, D. Bassi, U. Buck, and D. Laine. *Oxford University Press, New York*, 1:721, 1988.

[2] P.Milani and S.Iannotta. *Cluster Beam Synthesis of Nano-structured Materials*. Springer-Verlag, Berlin, 1999.

[3] Dunoyer. *Compt. rend.*, 2(3):153, 1911.

[4] W. Gerlach and O. Stern. *Z. Physik*, 8:110, 1921.

[5] W. Gerlach and O. Stern. *Z. Physik*, 9:349, 1921.

[6] A. Kantrowitz and J. Grey. *Rev. Sci. Instr.*, 22:328, 1951.

[7] E.W. Becker and K. Bier. *Zeitschrift Fuer Naturforschung A*, 9:975, 1956.

[8] O. Hagena and W. Henkes. *Zeitschrift Fuer Naturforschung A*, 15:851, 1960.

[9] J.B. Anderson. *Molecular Beams and Low Density Gasdynamics*. P.P. Wegener, New York, Dekker, 1974.

[10] H.C. Beijerinck, R.J.Van Gerwen, E.R. Kerstel, J.F. Martens, E.J. Van Vliembergen, M.R. Smits, and G.H. Kaashhoek. *Chemical Physics*, 96:153, 1985.

[11] M. Zucrow and J. Hoffman. *Gas Dynamics*, volume I, II. Wiley, New York, 1976.

[12] S.Iannotta, T.Toccoli, A. Boschetti, and M.Ferrari. *Applied Physics Letters*, 76:1845, 2000.

[13] S.Iannotta and T.Toccoli. *Journal of polymer science: Polymers physics*, 41:2501, 2003.

[14] T.Toccoli, S.Capone, L.Guerini, M.Anderle, A.Boschetti, E.Jacob, V.Micheli, P.Siciliano, and S.Iannotta. *IEEE Sensors Journal*, 3:199, 2003.

[15] O. Hagena and Obert. *J. Chem. Phys.*, 56:1793, 1972.

[16] H. W. Kroto, J. R. Heath, S. C. O'Brien, R. F. Curl, and R. E. Smalley. *Nature*, 318:162, 1985.

[17] S. Iannotta (G.Scoles). *Experiments with spin polarized beams in Atomic and Beam methods*, volume 1. Oxford university press (New York-Oxford), 1988.

[18] D. Bassi, A. Boschetti, S.Iannotta, M. Scotoni, and M.Zen. *Laser. Chem.*, 5:143, 1984.

[19] A. Boschetti, F. Biasioli, P. Miseri, P. Milani, and S. Iannotta. *Chemical Physics Letters*, 301:109, 1999.

[20] F. Biasioli, A. Boschetti, E. Barborini, P.Piseri, P.Milani, and S.Iannotta. *Chem. Phys. Lett.*, 270:115, 1997.

[21] D. Bassi, S. Iannotta, P. Tosi, H. Villinge, W. Dobler, and W. Lindiner. *J. Chem. Phys*, 80:1905, 1984.

[22] F. De Angeli, T.Toccoli, A.Pallaoro, N.Coppedè, L.Mariucci, G.Fortunato, and S.Iannotta. *Synthetic Metals*, 146:291, 2004.

[23] M. Taurino, S.Capone, A.Boschetti, T.Toccoli, R.Verucchi, A.Pallaoro, P.Siciliano, and S.Iannotta. *Sensor and antuactors B: Chemical*, 100:177, 2004.

[24] M. Taurino, S.Capone, P.Siciliano, T.Toccoli, A.Boschetti, L. Guerini, and S.Iannotta. *Sensor and Actuators B: Chemical*, 92:292, 2003.

[25] N. Coppedè, M. Nardi, T. Toccoli, M. Tonezzer, F. Siviero, V. Micheli, A. C. Mayer, and S. Iannotta. *Journal of Renewable and Sustainable Energy*, 2(5):053106, 2010.

[26] L.Aversa, R.Verucchi, G.Ciullo, P.Moras, M.Pedio, L.Ferrari, A.Pesci, and S.Iannotta. *Appl. Surf. Sci.*, 184:350, 2001.

[27] F. Rosei and R. Rosei. *Surf. Sci.*, 500:395, 2002.

[28] G. Pfaff and P. Reynders. *Chemical Reviews*, 99(7):1963, 1999.

[29] J. H. Braun, A. Baidins, and R. E. Marganski. *Progress in Organic Coatings*, 20(2):105, 1992.

[30] R. Zallen and M. P. Moret. *Solid State Commun.*, 137:154, 2006.

[31] L. Frazer. *Environ. Health Perspect.*, 109:174, 2001.

[32] K. Lubkowski, B. Grzmil, A. Markowska-Szczupak, and A. Tymejczuk. *Pol. J. Commun. Sci.*, 1:82, 2009.

[33] O. Carp, C.L. Huisman, and A. Reller. *Prog. Solid State Chem.*, 32:33, 2004.

[34] J.M. Herrmann. *Catal. Today*, 53:115, 1999.

[35] A. Fujishima and K. Honda. *Nature*, 37:238, 1972.

[36] D. A. Tryk, A. Fujishima, and K. Honda. *Electrochim. Acta*, 45:2363, 2000.

[37] A. Lu, Y. Guo, J. Liu, F. Liu, C. Wang, N. Li, and Q. Li. *Chinese Science Bulletin*, 49(21):2284, 2004.

[38] S. Malato, P. Fernandez-Ibanez, M.I. Maldonado, J. Blanco, and W. Gernjak. *Catalysis Today*, 147(1):1, 2009.

[39] A. Mills and S. Le Hunte. *Journal of Photochemistry and Photobiology A: Chemistry*, 108(1):1, 1997.

[40] M.R. Hoffmann, S.T. Martin, W. Choi, and D.W. Bahnemann. *Chemical Reviews*, 95(1):69, 1995.

[41] T.-H. Bui, M. Karkmaz, E. Puzenat, C. Guillard, and J.-M. Herrmann. *Research on Chemical Intermediates*, 33(3-5):421, 2007.

[42] J.F. Montoya, J.A. Velasquez, and P. Salvador. *Applied Catalysis B: Environmental*, 88(1-2):50, 2009.

[43] A. Mills, G. Hill, S. Bhopal, I. P. Parkin, and S. A. O'Neill. *Journal of Photochemistry and Photobiology A: Chemistry*, 160(3):185, 2003.

[44] H. Zhang and J.F. Banfield. *J. Mater. Chem.*, 8:2073, 1998.

[45] C.J. Howard, T.M. Sabine, and F. Dickson. *Acta Cryst.*, 47:462, 1992.

[46] B. O'Regan and M. Grätzel. A low-cost, high-efficiency solar cell based on dye-sensitized colloidal tio$_2$ films. *Nature*, 353:737, 1991.

[47] A. Hagfeldt and M. Grätzel. *Chem. ReV.*, 95:49, 1995.

[48] A. L. Linsebigler, G. Lu, and J. T. Yates. *Jr. Chem. ReV.*, 95:735, 1995.

[49] A. P. Alivisatos. *Science*, 271:933, 1996.

[50] C. Burda, X. Chen, R. Narayanan, and M. A. El-Sayed. *Chem. ReV.*, 105:, 1025, 2005.

[51] Y. Yin and A.P. Alivisatos. *Nature*, 437:664, 2005.

[52] U. Diebold. *Surface Science Rep.*, 48:53, 2003.

[53] X. Chen and S. S. Mao. *Chem. Rev.*, 107:2891, 2007.

[54] V. Swamy, A. Kuznetsov, L.S. Dubrovinsky, R.A. Caruso, D.G Shchukin, and B.C. Muddle. *Phys. ReV. B*, 71:184302/1., 2005.

[55] A.S. Barnard and P. Zapol. *Phys. ReV. B*, 70:235403/1, 2004.

[56] A.S. Barnard and P. Zapol. *J. Phys. Chem. B*, 108:18435, 2004.

[57] A.S. Barnard, P. Zapol, and L.A. Curtiss. *Surf. Sci.*, 582:173, 2005.

[58] A.S. Barnard and L.A. Curtiss. *Nano Lett.*, 5:1261, 2005.

[59] L. X. Chen, T. Rajh, W. Jager, J. Nedeljkovic, and M. C. Thurnauer. *J. Synchrotron Radiat.*, 6:445, 1999.

[60] X. Qian, D. Qin, Q. Song, Y. Bai, T. Li, X. Tang, E. Wang, and S. Dong. *Thin Solid Films*, 385:152, 2001.

[61] T. Ohsaka, F. Izumi, and Y. Fujiki. *Journal of Raman Spectroscopy*, 7(6):321, 1978.

[62] S. P. S. Porto, P. A. Fleury, and T. C. Damen. *Phys. Rev.*, 154:522, 1967.

[63] P. Limsuwan K. Thamaphat and B. Ngotaworncha. *Kasetsart J. (Nat. Sci.)*, 42:357, 2008.

[64] L. Chiodo, J.M Garcia-Lastra, A. Iacomino, S. Ossicini, J. Zhao, H. Petek, and A. Rubio. *Phys. Rev. B*, 82:045207, 2010.

[65] Y. Tezuka, S. Shin, T. Ishii, T. Ejima, S. Suzuki, and S. Sato. *Journal of the Physical Society of Japan*, 63:347, 1994.

[66] S. Rangan, S. Katalinic, R. Thorpe, R.A. Bartynski, J. Rochford, and E. Galoppini. *The Journal of Physical Chemistry C*, 114(2):1139, 2010.

[67] M van Schilfgaarde, T. Kotani, and S. Faleev. *Phys. Rev. Lett.*, 96:226402, 2006.

[68] T. Kotani and H. Kino. *Journal of Physics: Condensed Matter*, 21:266002, 2009.

[69] J. Muscat, A. Wander, and N.M. Harrison. *Chemical Physics Letters*, 342:397, 2001.

[70] A. Janotti, J.B. Varley, P. Rinke, N. Umezawa, G. Kresse, and C.G. Van de Walle. *Phys. Rev. B*, 81:085212, 2010.

[71] R. O. Jones and O. Gunnarsson. *Rev. Mod. Phys.*, 61:689, 1989.

[72] A. Amtout and R. Leonelli. *Phys. Rev. B*, 51:6842, 1995.

[73] H. Tang, H. Berger, P. Schmid, and F. Levy. *Solid State Communications*, 92(3):267, 1994.

[74] W. Mannstadt R. Asahi, Y. Taga and A. Freeman. *J. Phys. ReV. B*, 61:7459, 2000.

[75] S. Krischok, J. Ganster, D.W. Goodman, O. Hafft, and V. Kempter. *Surface and Interface Analysis*, 37(1):77, 2005.

[76] R. Sanjinés, H. Tang, H. Berger, F. Gozzo, G. Margaritondo, and F. Lévy. *Journal of Applied Physics*, 75(6):2945, 1994.

[77] N. Kruse and S. Chenakin. *Applied Catalysis A: General*, 391:367, 2011.

[78] S. Munnix and M. Schmeits. *Phys. Rev. B*, 31:3369, 1985.

[79] M. Ramamoorthy, R.D. King-Smith, and D. Vanderbilt. *Phys. Rev. B*, 49:7709, 1994.

[80] E. Cho, S. Han, H. Ahn, K. Lee, S.K. Kim, and C.S. Hwang. *Phys. Rev. B*, 73:193202, 2006.

[81] A. Cremades R. Plugaru and J. Piqueras. *J. Phys.: Condens. Matter*, 16:S261, 2004.

[82] J. Pascual, J. Camassel, and H. Mathieu. *Phys. Rev. B*, 18:5606, 1978.

[83] R. Saidur M. M. Hasan, A. S. M. A. Haseeb and H. H. Masjuki. *International Journal of Chemical and Biomolecular Engineering*, 1:93, 2008.

[84] Z. Wang, U. Helmersson, and P. Käll. *Thin Solid Films*, 405:50, 2002.

[85] H. Tang, F. Lévy, H. Berger, and P. E. Schmid. *Phys. Rev. B*, 52:7771, 1995.

[86] C. Kormann, D.W. Bahnemann, and M.R. Hoffmann. *J. Phys. Chem.*, 92:5196, 1988.

[87] L. Kavan, T. Stoto, M. Grätzel, D. Fitzmaurice, and V. Shklover. *J.Phys. Chem.*, 97:9493, 1993.

[88] A. Henglein. *Chem. Rev.*, 89:1861, 1989.

[89] N. Serpone, D. Lawless, and R. Khairutdinov. *J. Phys. Chem.*, 99:16646, 1995.

[90] S. Monticone, R. Tufeu, A.V. Kanaev, E. Scolan, and C. Sanchez. *Appl. Surf. Sci.*, 162:565, 2000.

[91] I. Fernandez, A. Cremades, and J. Piqueras. *Semiconductor Science and Technology*, 20(2):239, 2005.

[92] W.F. Zhang, M.S. Zhang, and Z.Yin. *Phys. Stat. Sol. a*, 179:319, 2000.

[93] R. Plugaru. *J. Thin Solid Films*, 516:8179, 2008.

[94] J. Xu, L. Li, Y. Yan, H. Wang, X. Wang, X. Fu, and G. Li. *Journal of Colloid and Interface Science*, 318:29, 2008.

[95] L. G. J. DE Haart and G. Blasse. *J. Solid State Chem.*, 61:135, 1986.

[96] J.M Wu, H.C. Shih, and W.T. Wu. *Nanotechnology*, 17:105, 2006.

[97] H. Najafov, S. Tokita, S. Ohshio, A. Kato, and H. Saitoh. *Japanese Journal of Applied Physics*, 44:245, 2005.

[98] A. Suisalu, J. Aarik, H. Maèndar, and I. Sildos. *Thin Solid Films*, 336:295, 1998.

[99] Y. zhu and c. ding and g. ma and z. du. *Journal of Solid State Chemistry*, 139:124, 1998.

[100] Y. Zhao, C. Li, X. Liu, F. Gu, H. Jiang, W. Shao, L. Zhang, and Y. He. *Materials Letters*, 61:79, 2007.

[101] G. Witte and Ch. Wöll. *J. Mater. Res.*, 19:1889, 2004.

[102] C.D. Dimitrakopoulos and P.R.L. Malenfant. *Adv. Mater.*, 14:99, 2002.

[103] W.R. Salaneck, K. Seki, and A. Kahn. *Conjugated Polymer and Molecular Interfaces.* J.-J. Pireaux (Eds.), Marcel Dekker, New York, 2001.

[104] S.R. Forrest. *J. Phys.: Condens. Matter*, 15:S2599, 2003.

[105] R. Ruiz, B. Nickel, N. Koch, L.C. Feldman, R.F. Haglund Jr., A.Kahn, F. Family, and G. Scoles. *Phys. Rev. Lett.*, 91:136102, 2003.

[106] L.S. Hung and C.H. Chen. *Mater. Sci. Eng. R*, 39:143, 2002.

[107] M. D. Angione, R. Pilolli, S. Cotrone, M. Magliulo, A. Mallardi, G. Palazzo, L. Sabbatini, D. Fine, A. Dodabalapur, N. Cioffi, and L. Torsi. *Materials Today*, 14(9):424, 2011.

[108] S.-H. Jang and A.K.-Y. Jen. *1.06 - Structured Organic Non-Linear Optics.* Academic Press, Amsterdam, 2011.

[109] Thien-Phap and Nguyen. *Surface and Coatings Technology*, (0):in press, 2011.

[110] N. Papageorgiou, E. Salomon, T. Angot, J.-M. Layet, L. Giovanelli, and G. Le Lay. *Progress in Surface Science*, 77(5-8):139, 2004.

[111] M. Della Pirriera, J. Puigdollers, C. Voz, M. Stella, J. Bertomeu, and R. Alcubilla. *Journal of Physics D: Applied Physics*, 42(14):145102, 2009.

[112] A. Ritz and H Lüth. *Applied Physics A: Materials Science and Processing*, 31:75, 1983.

[113] B.H. Schechtman and W.E. Spicer. *Journal of Molecular Spectroscopy*, 33(1):28, 1970.

[114] P. Mineo, F. Lupo, I. Fragala and E. Scamporrino, and A. Gulino. *Journal of Luminescence*, (0):–, 2011.

[115] C. Litwinski, I. Corral, E. A. Ermilov, S. Tannert, D. Fix, S. Makarov, O. Suvorova, L. Gonzalez, D. Wöhrle, and B Röder. *J. Phys. Chem. B*, 112:8466, 2008.

[116] F. Siviero, N. Coppedé, A. Pallaoro, A.M. Taurino, T. Toccoli, P. Siciliano, and S. Iannotta. *Sensors and Actuators B: Chemical*, 126(1):214, 2007.

[117] F. Siviero, N. Coppedé, A.M. Taurino, T. Toccoli, P. Siciliano, and S. Iannotta. *Sensors and Actuators B: Chemical*, 130(1):405, 2008.

[118] M. Grätzel. Review: Dye-sensitized solar cells. *Journal of Photochemistry and Photobiology C: Photochemistry Reviews*, 4:145, 2003.

[119] M. Wang, C. Huang, Y. Cao, Q. Yu, Z. Deng, Y. Liu, Z. Huang, J. Huang, Q. Huang, W. Guo, and J. Liang. *J. Phys. D: Appl. Phys.*, 42:155104, 2009.

[120] G. C. Vougioukalakis, A. I. Philippopoulos, T. Stergiopoulos, and P. Falaras. *Coordination Chemistry Reviews*, 255(21-22):2602, 2011.

[121] B. Li, L. Wang, B. Kang, P. Wang, and Y. Qiu. *Solar Energy Materials and Solar Cells*, 90(5):549, 2006.

[122] D. B. Williams and C.B. Carter. *Transmission Electorn Microscopy*. Springer Science, 1996 and further editions.

[123] S.Hüfner. *Photoelectron Spectroscopy.* Springer-Verlag, Berlin, 1995.

[124] J.F.Moulder, W.F.Stickle, P.E.Sobol, and K.D.Bomben. *Handbook of X-ray Photoelectron Spectroscopy.* Perkin-Elmer Corp., Eden Prairie, MN, USA, 1992.

[125] A. Nakaruk, D. Ragazzon, and C.C. Sorrell. *Thin Solid Films*, 518(14):3735, 2010.

[126] D. Briggs and M-P.Seah. *Practical Surface Analysis.* Wiley, Frankfurt, 1990.

[127] J.-J. Yeh and I.Lindau. *At. Data Nucl Data Tables*, 32:1, 1985.

[128] Z. Zhang, S.-P. Jeng, and V. E. Henrich. *Phys. Rev. B*, 43:12004, 1991.

[129] Y. P. Varshni. Temperature dependence of the energy gap in semiconductors. *Physica*, 34(1):149, 1967.

[130] B. Liu, L. Wen, and X. Zhao. *Mat. Chem. Phys.*, 106:350, 2007.

[131] M. Luo, K. Cheng, W. Weng, C. Song, P. Du, G. Shen, G. Xu, and G. Hang. *J. Phys. D: Appl. Phys.*, 42:105414, 2009.

[132] K. Madhusudan Reddy, C.V. Gopal Reddy, and S.V. Manorama. *Journal of Solid State Chemistry*, 158:180, 2001.

[133] V. Grillo, N. Armani, F. Rossi, G. Salviati, and N. Yamamoto. *Inst. Phys. Conf. Ser.*, 180:565, 2003.

[134] I. M. Tiginyanu, O. Lupan, V.V. Ursaki, L. Chow, and M. Enachi. *M. Comprehensive Semic. Science and Technology*, 3:369, 2011.

[135] M. Zhu, H. Huang, J. Gong, C. Sun, and X. Jianga. *J. of App. Phys.*, 102:043106, 2007.

[136] Y. Kakehi, K. Satoh, T. Yotsuya, A. Ashida, T. Yoshimura, and N. Fujimura. *Thin Solid Films*, 516:5785, 2008.

[137] A. Dodd, A. McKinley, T. Tsuzuki, and M. Saunders. *Journal of Physics and Chemistry of Solids*, 68:2341, 2007.

[138] M. G. Manera, J. Spadavecchia, D. Buso, C. de Julián Fernández, G. Mattei, A. Martucci, P. Mulvaney, J. Pérez-Juste, R. Rella, L. Vasanelli, and P. Mazzoldi. *Sensors and Actuators B*, 132:107, 2008.

[139] N. Papageorgiou, Y. Ferro, E. Salomon, A. Allouche, J.M. Layet, L. Giovannelli, and G. Le Lay. *Phys. Rev. B*, 68:235105, 2003.

[140] B. Brena and Y. Luo. *Radiation Physics and Chemistry*, 75:1578, 2006.

[141] F.Evangelista, V. Carravetta, G. Stefani, B. Jansik, M. Alagia, S. Stranges, and A. Ruocco. *J. of Chem. Phys*, 126:124709, 2007.

[142] Y. Alfreddson, B. Brena, K. Nilson, J. Ahlund, L.Kjeldgaard, M. Nyberg, Y. Luo, N. Martensson, A.Sandell, C.Puglia, and H.Siegbahn. *J. of Chem. Phys*, 122:214723, 2005.

[143] A. Ghosh, P.G. Gassman, and J. Almlöf. *J. A. Chem. Soc*, 116:1932, 1994.

[144] L.Ottaviano, L.Lozzi, F. Ramondo, P. Picozzi, and S. Santucci. *J. of Electr. Spectr. and Rel. Phenom.*, 105:145, 1999.

[145] M Grobosch, C.Schmidt, R.Kraus, and M.Knupfer. *Organic Electronics*, 11:1483, 2010.

[146] N. Marom, X. Ren, J. E. Moussa, J. R. Chelikowsky, and L. Kronik. *Phys. Rev. B*, 84:195143, 2011.

[147] M. P. Seah and W. A. Dench. *Surface and Interface Analysis*, 1(1):2, 1979.

[148] I. Thurzo, G. Pham, and D. R. T. Zahn. *Semiconductor Science and Technology*, 19(9):1075, 2004.

[149] M.T. Greiner, M.G. Helander, W.-M. Tang, Z.-B. Wang, J. Qiu, and Z.-H. Lu. *Nature Materials*, 11:76, 2012.

[150] M.V. Nardi. *PhD thesis: Organic and organolanthanide films syntesized by SuMBE as candidates for photonic materials.* 2007.